Department of Physics and Astronomy

University of Heidelberg

Master thesis

in Physics

submitted by

Joschka Hannes Schöner

born in Rothenberg

2022

Magnetic-Field Setup for Magneto-Optical-Trapping and Interaction-Tuning in Novel Dysprosium Quantum Gas Experiment

This Master thesis has been carried out by Joschka Schöner

at the

Ruprecht Karl University of Heidelberg

under the supervision of

Prof. Dr. Lauriane Chomaz

&

Prof. Dr. Selim Jochim

Abstract

This thesis describes the development of two magnetic coil pairs, one to produce highly homogenous and one for quadrupolar magnetic fields, both having a fast response time. One of the main challenges was to achieve the desired field quality and strength values and at the same time adapting the coils to a highly constrained space inside a reentrant viewport. A detailed description of the physics-based experimental requirements, and of the individual aspects of the design process is provided. In particular, we discuss how the design of the outer geometry of the coils and the choice of the wire play the main decisive roles in the design process. Important aspects of the manufacturing processes, like the implementation of an orthocyclic winding scheme, are highlighted. We then present different tests and characterisations performed on the coils in their final geometrical configuration. We find that with water cooling maximum fields of 57 G and gradients of 20 G cm^{-1} are achieved under continuous operation.
Furthermore, the optical design and first implementation of our 3D-magneto-optical trap are described.

Kurzfassung

In dieser Arbeit wird die Entwicklung von zwei Magnetspulenpaaren beschrieben, von denen eines zur Erzeugung hoch homogener und eines zur Erzeugung quadrupolarer Magnetfelder dient und beide eine schnelle Reaktionszeit haben. Eine der größten Herausforderungen bestand darin, die gewünschte Feldqualität und -stärke zu erreichen und gleichzeitig die Spulen an einen stark eingeschränkten Raum innerhalb eines reentrant Viewports anzupassen. Es wird eine detaillierte Beschreibung der physikalisch basierten experimentellen Anforderungen und der einzelnen Aspekte des Entwicklungsprozesses gegeben. Insbesondere wird erörtert, wie die Gestaltung der äußeren Geometrie der Spulen und die Wahl des Drahtes entscheidende Rollen in diesem Prozess spielen. Wichtige Aspekte des Herstellungsprozesses, wie die Implementierung eines orthozyklischen Wickelschemas, werden hervorgehoben. Anschließend stellen wir verschiedene Tests und Charakterisierungen vor, die an den Spulen in ihrer endgültigen geometrischen Konfiguration durchgeführt wurden. Wir stellen fest, dass mit Wasserkühlung maximale Felder von 57 G und Gradienten von 20 G cm^{-1} im Dauerbetrieb erreicht werden.
Weiterhin werden das optische Design und die erste Implementierung unserer 3D-magneto-optischen Falle beschrieben.

Acknowledgement

First and foremost, I would like to thank Prof. Dr Lauriane Chomaz very much for the extraordinary supervision of this thesis, including very enjoyable, extensive discussions about even the tiniest aspects of this work and furthermore for all the other funny moments.

Special thanks also go to Prof. Dr Selim Jochim for kindly being my second examiner and supporting my thesis with comprehensive and very creative discussions.

Furthermore, I would like to express my gratitude towards our mechanical workshop and especially to Jessica Riedinger and Simon Rabenecker, for all their time and expertise flowing into the manufacturing process.

For the great support with my measurements, another thank you goes to Lennart Hoenen and also to Jianshun Gao for all the boundless and very funny discussions. Furthermore, I would like to acknowledge Shuwei Jin and Karthik Chandrashekara for doing the major work of the MOT implementation.
Since enumerating them all would, unfortunately, go beyond the scope of this acknowledgement: Thank you very much to all members of the group for supporting me in various ways and most importantly making my time here very enjoyable!

Contents

List of Figures

List of Tables

Acronyms

2D two-dimensional.

3D three-dimensional.

AHH anti-Helmholtz.

BEC Bose-Einstein condensate.

CNC computerized numerical control.

Dy Dysprosium.

FR Feshbach resonance.

HH Helmholtz.

IR infrared.

MOT magneto-optical trap.

op amp operational amplifier.

PBS polarizing beamsplitter.

PEEK polyether ether ketone.

RF radio frequency.

RMS root mean square.

SF small field.

1 Introduction

Understanding the deep nature of quantum mechanics is still one of the frontier aims of modern physics. Decades of extensive research in the techniques of laser cooling and trapping at the end of the last century, finally brought up ultracold quantum gases as a prime experimental platform to study quantum mechanics due to their outstanding level of controllability. The first realization of a Bose-Einstein condensate (BEC) of rubidium [1] and sodium [2] in 1995 was the first step of an immense development in this field that is still ongoing. Since quantum degeneracy of the highly magnetic chromium atom species was achieved in 2004 [3], studying dipolar quantum gases has become an emerging research topic. On the one hand, they show the standard contact interaction in ultracold gases, tunable in strength via Feshbach resonance (FR)s and on the other hand, they offer the competing long-range anisotropic dipole-dipole interactions, tunable via the orientation of the magnetic field. These two competing interaction with a high tunability is enabling us to study a whole new field in physics [4]. As one of the most magnetic atom species, which furthermore offers a very suitable electronic structure for laser cooling [5], as well as a wide spectrum of FRs [6], Dysprosium (Dy) has become a candidate of great interest for studying these systems. Some breakthroughs are the realization of stable quantum macro-droplet states [7, 8, 9] or evidence of supersolidity [10, 11, 12, 13].

Our goal is to study exotic physical phenomena like supersolidity, topological ordering and some out-of-equilibrium physics which emerge when the system is restricted to two dimensions. At our new Quantum Fluids group supervised by Lauriane Chomaz at Heidelberg University, we are currently building a new cold atom experiment in which we transfer Dy from a two-dimensional (2D)-magneto-optical trap (MOT) to a three-dimensional (3D)-MOT before loading them into a crossed dipole trap and later into a tailorable in-plane trap to achieve 2D-confinement.

A fully 3D-tunable magnetic field setup is one of the main prerequisites for such an experiment. We need to be able to tune the contact-contact interaction by addressing FRs [14] and also modulate the dipole-dipole interaction by having full control over the orientation of the magnetic-dipole moment of the atoms [4]. Furthermore, a quadrupole magnetic field is needed for trapping the atoms in the 3D-MOT [15] and separate the pseudo-spin-composition of an atomic cloud [16].

In the scope of this thesis, a high-performance, low-space consuming coil setup, consisting of two pairs of coils, one producing a highly homogeneous and one a gradient magnetic field, was developed. Both are low-noise and offer a fast fast response time thanks to our home-built power supply developed by Lennart Hoenen [17]. Furthermore, the optical setup of our 3D-MOT was designed and implemented leading to the achievement of the first 3D-MOT of Dy^{164} atoms in our setup in May 2022. This is the first-ever 3D-MOT of Dy loaded from a 2D-MOT atomic jet.

In chapter 2 I will present some important properties of Dy and describe which are the needed magnetic fields in our experiment and their requirements. Chapter 3 provides a detailed description of the design process of the magnetic coils. The previously defined requirements were adapted to our specific experimental setup, a thermal simulation was done and the final coil configuration, including calculated characteristics, are provided. The rather involved manufacturing process of the water-cooled coil holder and the winding process is presented in chapter 4. The final coil setup is then experimentally characterized in chapter 5, by measuring the heating characteristics, time and frequency response, as well as some magnetic field measurements. The design process and realization of the optical setup of our 3D-MOT is described in chapter 6. The optical setup has been characterized and a brief overview of our first realization of the MOT is provided.

2 | Magnetic Fields in Dysprosium Quantum Gas Experiments

In this chapter, we describe why magnetic field management is important in cold atom experiments in general and in the case of dysprosium atoms in particular. This holds both for homogeneous and gradient fields. We discuss the different applications of such fields and deduce requirements for our Dy setup.

2.1 Properties of Dy

2.1.1 Magnetic properties of the ground state

As mentioned before, Dysprosium is of particular interest due to its very high magnetic momentum. The magnetic moment is determined by the electron dynamics. The electron configuration for Dy is given by [18]

$$[\mathrm{Xe}]\ 4\mathrm{f}^{10}\ 6\mathrm{s}^{2}, \tag{2.1}$$

with twelve valence electrons occupying the 6s-shell and partially the 4f-shell, leaving 4 unpaired electrons. Russel-Sanders (LS)-coupling provides a good description of the Dy ground-state (as justified below), which can therefore be described by the quantum number triplet (L, S, J). All individual electron orbital angular momenta $\boldsymbol{\ell}_i$ and spins $\boldsymbol{s}_i$ couple individually to a total orbital angular momentum $\boldsymbol{L}$ and spin $\boldsymbol{S}$, which then couple to the total angular momentum $\boldsymbol{J} = \boldsymbol{L} + \boldsymbol{S}$ [19].

The bosonic isotopes ^{162}Dy and ^{164}Dy, in which we are primarily interested in our experiment, exhibit a ground state configuration of [20]

$$^{5}\mathrm{I}_{8}, \tag{2.2}$$

with no nuclear spin $\boldsymbol{I}$, in the notation $^{2S+1}L_J$.

Following the derivation of [19], the magnetic moment $\boldsymbol{\mu}$ has contributions of $\boldsymbol{L}$ and $\boldsymbol{S}$:

$$\boldsymbol{\mu} = -\mu_{\mathrm{B}}\boldsymbol{L} - g_s\mu_{\mathrm{B}}\boldsymbol{S}, \tag{2.3}$$

with the Bohr magneton μ_B and Landé factor g_S. The interaction with an external magnetic field $\boldsymbol{B}$, known as the Zeeman effect, is given by $H_{\mathrm{ZE}} = -\boldsymbol{\mu} \cdot \boldsymbol{B}$. If the strength of the interaction is much smaller than the LS-coupling and thus H_{ZE} can be treated as perturbation to the fine structure, the expectation value can be calculated in the basis $|LSJm_J\rangle$ as

$$E_{\mathrm{ZE}}(m_J) = m_J g_J \mu_{\mathrm{B}} B \tag{2.4}$$

with $\boldsymbol{B} = B\boldsymbol{e}_z$ and m_J the projection of $\boldsymbol{J}$ onto the quantization axis $\boldsymbol{e}_z$. For g_J follows

$$g_J = \frac{3}{2} + \frac{S(S+1) - L(L+1)}{2J(J+1)}. \tag{2.5}$$

The magnitude of the magnetic moment follows from equation 2.4 to be

$$\mu = -m_J g_J \mu_B. \tag{2.6}$$

Inserting the ground state configuration (2.2) into (2.5) yields $g_{J,\mathrm{D}y} = 1.25$. In fact, the experimentally measured value is $g_{J,\mathrm{Dy}} = 1.241\,586\,9(10)$ [20], showing that the rather simple assumption of LS-coupling does not perfectly describe the complex situation, but still to a good approximation. The absolute magnetic moment for Dy in its ground state, having $m_J = -8$, follows via (2.6) as $|\mu_{\mathrm{Dy}}| = 9.93\,\mu_B$, making Dy to one of the most magnetic atomic species. The consequently very strong dipole-dipole interaction makes Dy a very interesting candidate to study dipolar quantum gases.

2.1.2 Energy levels and laser cooling transitions

Additional to its very promising magnetic properties Dy offers an optical spectrum perfectly suited for laser cooling. Of particular interest for us are the two transitions depicted in figure 2.1 where one of the 6s electrons is excited to the 6p orbital. The two excited states can no longer be described by the simple LS-coupling scheme. A better description is offered by the J_1J_2-coupling scheme, in which the inner 4f electrons couple to ${}^5I_8$ ($J_1 = 8$), whereas the outer 6s and 6p electrons individually couple to the singlet- and triplet-states ${}^1P_1$ and ${}^3P_1$ ($J_2 = 1$), respectively (see figure 2.1). The two angular momenta $\boldsymbol{J}_1$ and $\boldsymbol{J}_2$ subsequently couple to the total angular momentum $\boldsymbol{J}$, expressed via the notation $(J_1, J_2)_J$. [20]

	Unit	421 nm	626 nm
Wavelength λ	nm	421.291	626.082
Natural Linewidth Γ	$2\pi \times$ MHz	32.2	0.135
Saturation Intensity I_{sat}	mW/cm^2	56.4	72×10^{-3}
g-factor of excited state $g_{J,e}$		1.22	1.29
Doppler cooling temperature limit T_{D}	µK	774	3.2

Table 2.1: Properties of the blue 421 nm and red 626 nm transitions we use to cool, trap and image Dy [5]

The two important transitions we use in the experiment are shown in figure 2.1 (with $J = 9$) and their properties are listed in table 2.1. On the one hand, we have the broad

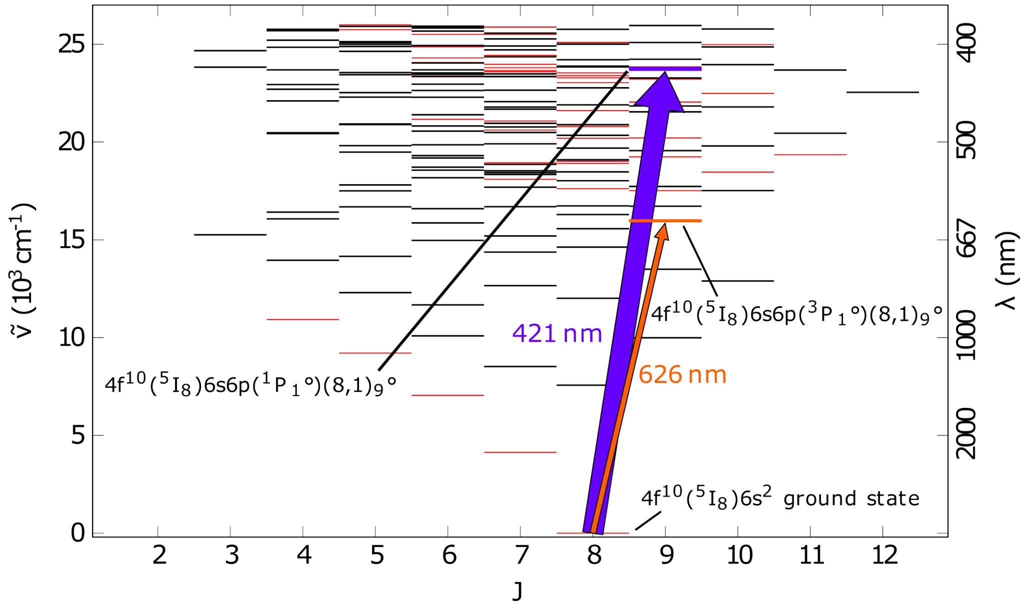

Fig. 2.1. Energy level diagram of Dy in wavenumber $\tilde{\nu}$ or corresponding wavelengths λ: The blue arrow represents the broad 421 nm transition from the ground state to the 6s6p(^{1}P$_1$)(8, 1)$_9$ excited state and the orange one the narrow transition to the 6s6p(^{3}P$_1$)(8, 1)$_9$ state (figure adapted from [21, p. 22]) [1]

blue transition, perfectly suited to precool the atoms, as well as for imaging. On the other hand the narrow red transition, with its corresponding low Doppler temperature (see (2.12)), enables a rather cold MOT, making the loading into the dipole trap easier (see sec. 2.4.1).

2.2 Homogeneous Magnetic Fields

In this section, we discuss how a homogeneous magnetic field enables to control both the contact interaction strength [14] and the anisotropy of dipole-dipole interaction. As introduced, this tuning is crucial to explore novel many-body phenomena in Dy quantum gases, as they arise from the competition of these two interactions.

2.2.1 Dipolar interactions

The dipole-dipole interaction between two atoms having atomic mass M and relative position $\boldsymbol{r}$, with their dipole moments oriented along the unit vectors $\boldsymbol{e}_1$ and $\boldsymbol{e}_2$ (see fig. 2.2 (a)) is given by [22]

$$V_{\mathrm{dd}}\left(\boldsymbol{r}\right) = \frac{3\hbar}{M} a_{\mathrm{dd}} \frac{\left(\boldsymbol{e}_1 \cdot \boldsymbol{e}_2\right) r^2 - 3\left(\boldsymbol{e}_1 \cdot \boldsymbol{r}\right)\left(\boldsymbol{e}_2 \cdot \boldsymbol{r}\right)}{\boldsymbol{r}^5}, \tag{2.7}$$

with the dipolar length

$$a_{\mathrm{dd}} = \frac{M \mu_0 \mu^2}{12\pi\hbar}. \tag{2.8}$$

---

[1] The °-symbol in the electron configuration denotes odd parity

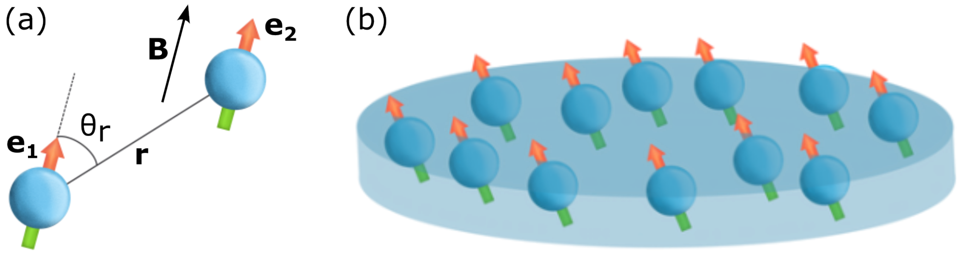

Fig. 2.2. (a) Schematic of two atoms with their magnetic moment aligned along the unit vectors $\boldsymbol{e}_1$ and $\boldsymbol{e}_2$, with an external magnetic field $\boldsymbol{B}$, (b) Schematic representation of several magnetically polarized atoms

Here $\hbar$ is the reduced Planck constant and μ_0 the vacuum permeability.
In a magnetically polarized sample all atoms magnetic moments point in the same direction (see fig. 2.2 (b)). In this case (2.7) simplifies to

$$V_{\text{dd}}\left(\boldsymbol{r}\right)=\frac{3\hbar}{M}a_{\text{dd}}\frac{1-3\cos^2\theta_{\text{r}}}{|\boldsymbol{r}|^3}. \tag{2.9}$$

The angle θ_{r} between the magnetic moment and the connection axis (cf. fig. 2.2 (a)) determines if the interaction is repulsive or attractive and is therefore responsible for the anisotropic character of the interaction. The $\propto 1/r^3$ slope describes its long-range behaviour. Due to equ. (2.3), in presence of any finite magnetic field (setting the polarisation axis), magnetic polarization implies that only one magnetic level m_J is populated. In this case, the magnetic dipoles are aligned along the magnetic field axis. Magnetic polarisation of magnetic atoms naturally occurs in ultracold gases in presence of a homogeneous magnetic field of even a fraction of mG magnitude. The underlying reason is actually found in formula (2.7) combined to (2.3)-(2.4). The bare dipole-dipole interaction may induce a modification of magnetic levels of the two colliding partners. In presence of a magnetic field, the energy degeneracy of the magnetic levels is lifted and collisions involving a change of m_J to lower values are energetically favoured. Therefore, if k_BT is small enough compared to $E_{\text{ZE}}(m_J)-E_{\text{ZE}}(m_J-1)$, the gas gets spontaneously polarised to $m_J=-J$ by dipolar relaxation.
As seen in (2.8) the strength of the interaction depends on the square of the value of the magnetic moment, showing why Dy is such an interesting candidate for studying dipolar systems.

Due to the anisotropy of the interaction, it is of great interest to investigate scenarios in which the atoms are oriented in an arbitrary direction with respect to the trap geometry (cf. fig 2.2 (b)), as this greatly influences the mean atom interaction. Therefore we need a magnetic field system with full 3-axis field control.

2.2.2 Feshbach resonances

For two atoms of the same species with relative position $\boldsymbol{r}$ the contact interaction potential is given by [23]

(2.10)

with the s- wave scattering length a_S. The character of the contact-like interaction can be approximated via the Dirac delta distribution $\delta\left(\boldsymbol{r}\right)$.
The basic idea and properties of FRs can be derived from a rather simple picture. Considering two molecular curves (see fig. 2.3 (a)), representing the potential of two atoms in the ultracold gas approaching each other by a distance R. The background potential $V_\mathrm{bg}(R)$, being the open channel, asymptotically approaches the limit of two free atoms in the gas.

The closed channel with potential V_c, corresponds to the dissociation limit ($R \to \infty$) to two free atoms in different internal states with higher total energy $E_{\mathrm{c},\infty} > 0$. For energies $E < E_{\mathrm{c},\infty}$, bound molecular states with an energy E_c can occur in the closed channel. The value of E_c can be magnetically tuned relatively to the open channel, which leads to resonant coupling for $E_\mathrm{c} \to 0$. This has a direct impact on a_S of the atoms, which for $R \to \infty$ collide in the open channel. For a magnetically tuned FR the scattering length is given by [14]

$$a_\mathrm{S}(B) = a_\mathrm{bg}\left(1 - \frac{\Delta_\mathrm{FR}}{B - B_0}\right). \tag{2.11}$$

Here a_bg refers to the background scattering length associated with the background channel, representing the off-resonant value. Tuning the value of the magnetic field B around the position B_0 (corresponding to $E_c = 0$) of the FR, with width Δ_FR, enables the opportunity to get direct access to the scattering properties (cf. fig. 2.3 (b)) and therefore the strength of the contact interaction of the atoms, being the dominant interaction in non-dipolar ultracold gases. Note that the strength of the coupling of the two channels is determined by the difference in the magnetic moment of the closed and open channel.

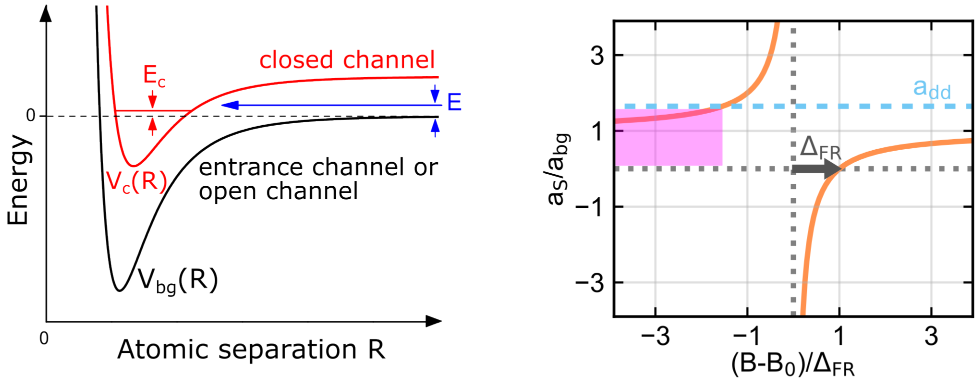

Fig. 2.3. (a) Two-channel model of FR: Two atoms with an energy E collide in the open channel and couple to a bound molecular state with energy E_c of the closed channel potential (figure taken from [14, p. 3]), (b) s-wave scattering length a_S around a FR at position B_0 with width Δ_FR: In the in-pink marked region where a_S is smaller than the dipolar length a_dd, new orders in quantum gases can be realized (see text)

In figure 2.3 (b) also the dipolar length of the dipole-dipole interaction a_dd is noted (see sec. 2.2.1). Of particular interest is the in-pink marked region, where a_S is tuned below a_dd. In standard non-dipolar BECs typically the mean interaction becomes attractive in this regime (now corresponding to $a_\mathrm{S} < a_\mathrm{dd} = 0$) and a so-called Bosenova, a super-nova-like explosion of the system, is observed [24]. In dipolar gases, on the other hand, it is possible to realize stable states due to beyond mean-field effects of the interactions via quantum fluctuations, first described by Lee, Huang and Yang in 1957 [25], e.g. in the form of a self-stable dense macrodroplet state realized in [8, 7, 9, 4].

2.3 Gradient Magnetic Fields

2.3.1 Magneto-optical trap

Trapping and cooling atoms in vacuum is always a precondition to do a cold atoms experiment. A 3D-MOT is usually the first step, after pre-cooling the atoms either with a Zeeman-Slower or a 2D-MOT, to achieve trapping in three dimensions, as well as cooling to a certain limit. The detailed working principle can be read for example in [19]. In the following, a brief overview is provided.

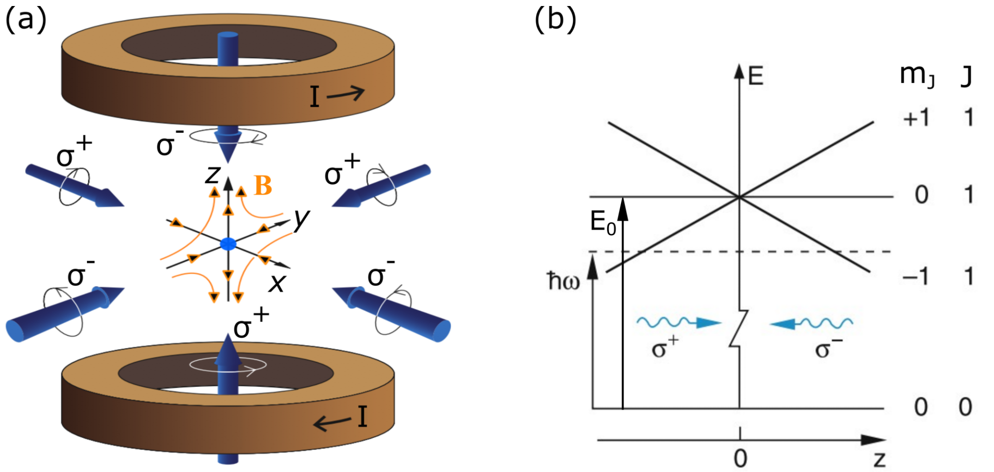

Fig. 2.4. MOT working principle: (a) Schematic representation of circularly polarized beams (blue arrows) crossing in the centre of a quadrupole field, generated by a pair of magnetic coils (in brown), with circulating current I in opposite direction (fig. adapted from [26, p. 24]), (b) Explanation of MOT working principle in one dimension: The solid lines are the energies of the different Zeeman levels with respect to the position of the atoms in presence of a magnetic gradient along the $z-$axis. The dashed line denotes the energy of the red-detuned laser beam. (figure adapted from [27, p. 458])

The most common configuration of a 3D-MOT consists of six counter-propagating circularly polarized laser beams crossing in the centre and a quadrupole magnetic field being zero in the centre and increasing magnitude in all directions (cf. fig. 2.4 (a)). The laser beams have a frequency ω, red-detuned with respect to an electronic atomic transition ω_0: $\delta \equiv \omega - \omega_0 < 0$. Due to the Doppler effect, the probability of absorbing a photon from a beam in which direction the atom is currently moving is increased and it therefore on average gets a momentum kick against its moving direction. The subsequent spontaneously emitted photon has no preferred direction, leading to a momentum kick in a random direction. Consequently, the atom experiences a net force against its moving direction, slowing it down. This cooling setup is called an optical molasses. Due to the subsequent absorption and emission processes the atom performs a random walk, leading to a non-zero mean square velocity, determining the minimum Doppler temperature T_D, which can be reached via this technique:

$$k_\mathrm{B}T_\mathrm{D} = \frac{\hbar\Gamma}{2}, \tag{2.12}$$

with k_B being the Boltzmann constant. This temperature is reached for the case of $\delta = -\Gamma/2$, with Γ the linewidth of the respective transition.

The trapping principle is depicted in figure 2.4 (b) for one dimension and relies on the presence of the magnetic gradient together with selection rules for the electronic transition and photon polarization. For simplicity a two-level system with an angular momentum of $J = 0$ for the ground state $|g\rangle$ and $J = 1$ for the excited state $|e, m'\rangle$ is chosen. The energy difference ΔE between these two states can be derived via (2.4) and is with respect to the transition energy in the centre of the trap E_0 (cf. fig. 2.4) given by:

$$\Delta E = E_0 + m' g'_J \mu_B \frac{\mathrm{d}B}{\mathrm{d}z} z, \tag{2.13}$$

with g'_J the Landé-factor of the exited state.
If the atom now moves into positive z-direction out of the trap centre, the transition $|g, 0\rangle \rightarrow |e, -1\rangle$ becomes resonant (or the less detuned) (cf. 2.13) and begin to cycle. As this transition can, due to selection rules, only be excited by σ^- polarized light, which is counter-propagating to the z-axis, the atom is pushed back to the centre of the trap. A similar process with the $|g, 0\rangle \rightarrow |e, +1\rangle$ transition absorbing the along the z-axis propagating σ^+-polarized light, happens for a displacement in the other direction. Note that the quantization axis of this system is the spatially fixed z-axis.
To conclude, the strength of the magnetic field gradient is crucial for the trapping effect of the MOT.

2.3.2 Stern-Gerlach separation

In cold atom experiments, the pseudo-spin-composition of an atomic cloud can be of great interest. Due to the Zeeman effect (cf. 2.4) each atom with a different spin projection m_J of an atomic sample experiences a different force in a spatially varying magnetic field:

$$F = -m_J g_J \mu_\mathrm{B} \frac{\mathrm{d}B}{\mathrm{d}z}. \tag{2.14}$$

We can make use of that by applying a gradient magnetic field and spatially separating the individual spin components of an atomic cloud along the z-axis, known as Stern-Gerlach separation. In this process, the atom cloud will also fall, but as we are only interested in the separation of the cloud, it is sufficient to calculate the difference in acceleration Δa for two neighbouring spin components, which follows from (2.14) as

$$\Delta a = \frac{1}{M} g_J \mu_\mathrm{B} \frac{\mathrm{d}B}{\mathrm{d}z}. \tag{2.15}$$

To clearly distinguish the several spin components of an atom cloud, they need to be separated by twice the root mean square (RMS) cloud size along the z-axis σ_z. The gradient along the z-axis, needed to perform this separation, applied during a time Δt, directly follows from Newton's mechanics:

$$\frac{\mathrm{d}B}{\mathrm{d}z} = \frac{4\, M\, \sigma_\mathrm{rms}}{g_J\, \mu_\mathrm{B}\, \Delta t^2} \tag{2.16}$$

is needed.

The RMS size of interest is given by the size of an atom cloud with temperature T, after a free expansion, which writes:

$$\sigma_z^2(\Delta t) = \sigma_z^2(0) + \frac{k_B T}{M}\Delta t^2. \tag{2.17}$$

2.4 Field Requirements for Our Experiments

2.4.1 Experimental overview

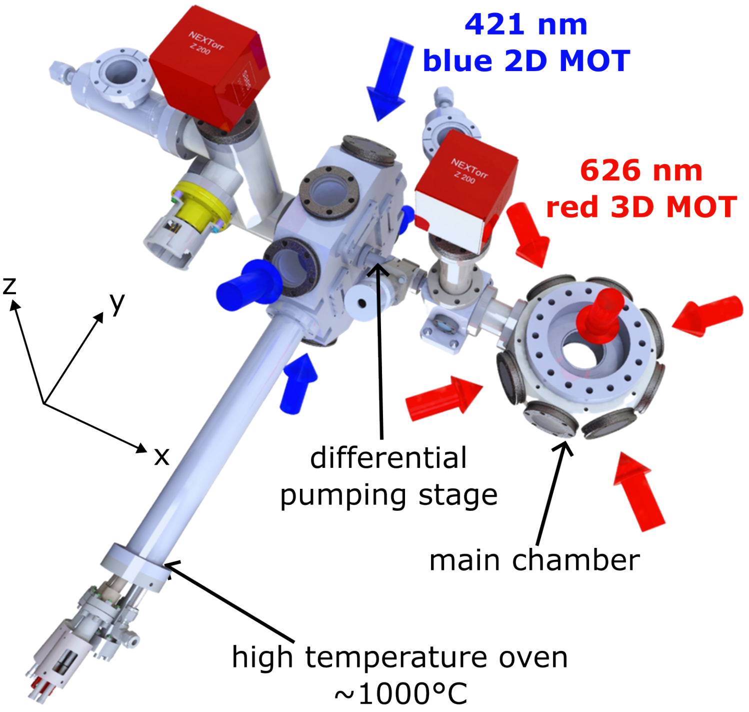

Fig. 2.5. Experimental overview: Atoms are evaporated in the high-temperature oven and go from there through the blue 2D-MOT and the differential pumping stage into the main chamber where they are captured via a red 3D-MOT and further processed (see text)

As pictured in figure 2.5 the experiment consists of one big vacuum apparatus. The Dy atoms are vaporized in a high temperature oven at about 1000 °C and get from there as a hot atomic vapour jet to the 2D-MOT, where the atoms are decelerated to almost zero velocity and trapped in 2 dimensions (in the x-z plane, cf. fig. 2.5) on the blue 421 nm transition of Dy. From there a blue push beam transports the atoms through a differential pumping stage into the main science chamber, containing an ultra-high vacuum with a pressure below 1×10^{-11} mbar. Here they are captured in a 3D-MOT on the 626 nm transition and reach a temperature close to the Doppler limit $T_D = 3.2\,\mu K$ (see tab. 2.1 after a compression of the MOT. In the next step, the atoms will be loaded into a dipole trap, where quantum degeneracy is reached via evaporative cooling and afterwards into a tailorable in-plane trap (accordion lattice), which makes it possible to create an effective

2D system. At this final stage, the atoms' dipolar and contact interactions can be tuned via the homogeneous magnetic fields (cf. sec. 2.2).

2.4.2 Homogeneous fields

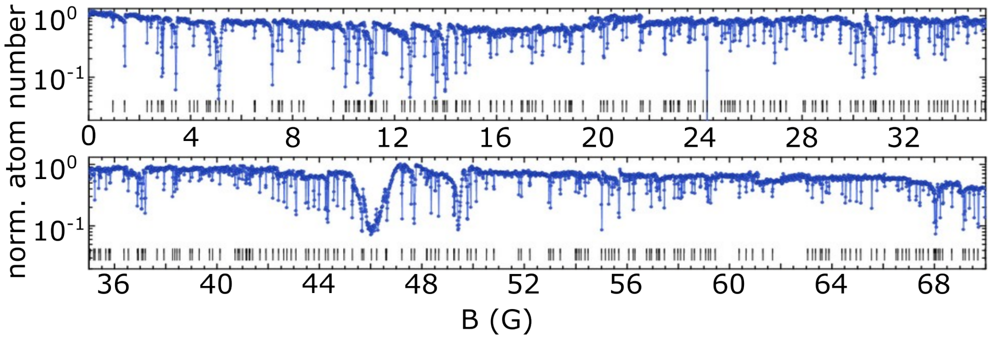

Fig. 2.6. Spectrum of Feshbach resonances of ^{164}Dy below 75 G obtained via trap-loss spectroscopy (figure taken from [6])

As discussed in section 2.2.2 we want to be able to address FRs of Dy to tune the contact interaction strength. Dy offers a wide spectrum of FRs even at low field strengths (cf. 2.6) [6, 28], which is a great technical benefit, as it is not needed to use very high magnetic fields, common for other atom species classically used for BECs. For example, in ^{6}Li the FRs are at several hundreds of Gauss [29].

Even below 10 G there are several interesting FRs for Dy. We plan to work primarily with them, which sets the minimum magnetic field strength requirement for our magnetic coil setup:

$$B_{\text{min}} = 10\,\text{G}. \tag{2.18}$$

We want to be able to achieve this field in an arbitrary direction to control the orientation of the atoms' magnetic moments (cf. sec. 2.2.1). Therefore we need a setup of three pairs of magnetic coils around our chamber. This thesis describes the development of one of pair around the symmetry (z)-axis of our chamber (cf. fig 2.5), we will call them Helmholtz (HH)-coils. The other two in form of two rectangular coils were developed in the scope of Lennart Hoenens Bachelor's thesis [17].

Of course, it would be beneficial to be able to achieve higher magnetic fields, at least in one direction to account for future plans, where we might also want to address higher lying FRs. Therefore in the whole design process of the HH-coils, B_{min} was used as an absolute minimum requirement.

The next important requirement is the field stability, both spatially and temporarily, we want to achieve. The width of the FRs was used as a decision criterion here, as we want to be able to tune the magnetic field value precisely in this region. In figure 2.7 a measurement of one exemplary FR of ^{164}Dy is shown. This specific resonance is actually one, we plan to work with. The widths of the FRs are on the order of 100 mG. We would like to tune the magnetic field value with a precision two orders of magnitudes smaller than this, resulting in an absolute precision of 1 mG. As this is the minimum requirement,

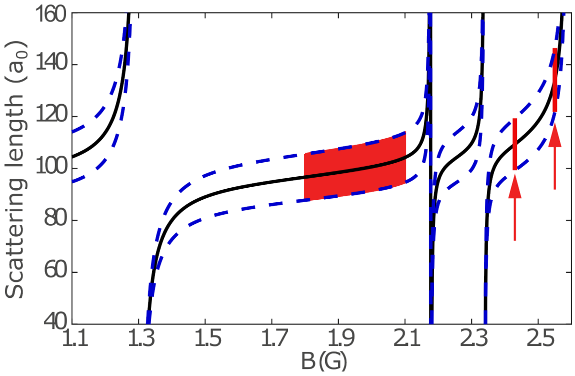

Fig. 2.7. Estimated scattering length dependence a_S from the magnetic field B, extracted from trap-loss spectroscopy (fig. taken from [12])

we formulated the requirement in terms of relative field stability δB to reach this absolute precision at 10 G:

$$\delta B < 1 \times 10^{-4}. \tag{2.19}$$

Spatially we want to achieve this field stability in a region of ±1 mm in all directions around the centre, as this is roughly the size of a thermal cloud in the 3D-MOT [30]. Furthermore, this directly implies the current stability and maximum noise level of our power supply.

The last requirement is the time response of our coil setup. At the final stage of the experiment the atoms will be captured in a 2D dynamical optical trap (in the $x - y$-plane), an accordion lattice which provides strong confinement along the z-diretion and a tunable in-plane trap based on Digital micromirror device (DMD) and a microscope. The dynamics of the atoms in the plane are determined by frequency associated with the ground state of the trap in these directions, which are below 100 Hz [31]. We want to be able to switch our magnetic fields much faster than this, resulting in the desired time-scale for full switch on/off of the field of:

$$\Delta t_{\text{on/off}} < 1\,\text{ms}. \tag{2.20}$$

Furthermore, we want to have the possibility to drive the system, introducing non-equilibrium dynamics. Therefore we want to be able to vary the field with an amplitude in the order of 50 mG at several kHz. These requirements apply to both, the power supply and the magnetic coil characteristics.

2.4.3 Gradient fields

According to Monte-Carlo simulations of the MOT-loading carried out by Jianshun Gao [32], the optimum gradient to achieve a 3D-MOT on the 626 nm-transition of Dy is $1\,\text{G}\,\text{cm}^{-1}$, along the strong gradient (z-) axis of the field. This order of magnitude matches what was used before, as e.g. $1.7\,\text{G}\,\text{cm}^{-1}$ in [30]. To have some margin for optimizing the MOT, we agreed on a gradient of $5\,\text{G}\,\text{cm}^{-1}$, which we should be able to achieve.

The more challenging constraints were dictated by the gradient values needed for Stern-Gerlach separation. As a minimum requirement we wanted to be able to do a Stern-Gerlach separation of a degenerate cold atoms cloud, having a temperature of $T = 3.2\,\mu\mathrm{K}$, which should be a save upper limit for a thermal gas loaded in a dipole trap (see low-temperature limit valid for our MOT in table 2.1, in a time interval of $\Delta t = 20\,\mathrm{ms}$. The initial size of such a cloud is neglected and after Δt the size follows from (2.17) as $\sigma_z = 0.26\,\mathrm{mm}$, according to (2.16) resulting in a gradient of

$$\frac{\mathrm{d}B}{\mathrm{d}z} = 6\,\mathrm{G/cm}, \tag{2.21}$$

fixing the minimum requirement for our gradient-coil pair, called anti-Helmholtz (AHH)-coils from now on.
If possible, it would be favourable to have the possibility to do a Stern-Gerlach separation also of a thermal cloud in the MOT. In [30] a gradient of about $30\,\mathrm{G\,cm^{-1}}$ was applied for $4\,\mathrm{ms}$, followed by a subsequent $20\,\mathrm{ms}$ free expansion for this task. Similar to the HH-coil, also for the AHH-coil 2.21 was kept as absolute minimum requirement during the design process, such that it is highly likely to achieve significantly larger gradients.

The uniformity of the gradient is of less importance than the field quality of the HH-coils, as for both the MOT as well as Stern-Gerlach separation we will not perform quantitative measurements relying on the exact value of the magnetic gradient.

3 | Magnetic Coil Design

In this chapter, the design process of the magnetic coils inside the reentrant viewport of our main science chamber (see fig. 3.1) is described. A detailed description of, how and why the outer geometry of the coils as well as the wire geometry were determined, is provided and the resulting coils are characterized based on calculations.

The stainless steel chamber has an octagon shape with CF40 flanges on the site and two CF100 flanges on the top and bottom, where we plan for reentrant viewports (cf. fig. 3.1) for optimized optical access and magnetic coils close to the atoms. As described in section 2.4 the experiment needs four sets of individually controllable coils. The two pairs of (rectangular) coils around the main chamber, producing a homogeneous field in x- and y- direction (cf. fig. 2.5) [17] and the two pairs symmetrically around the symmetry (z-) axis of the main chamber, described in this thesis. One pair produces a homogeneous field along the z-axis, and one pair generates a gradient magnetic field. These coils are placed inside the inverted viewport to be as close as possible to the atoms. This has two benefits, first one needs a lower current to produce the same field magnitude in the centre. Second, there is less conducting material (metal chamber) in between the coils and the atom cloud, minimizing eddy currents and therefore decreasing the switching time of the magnetic field.

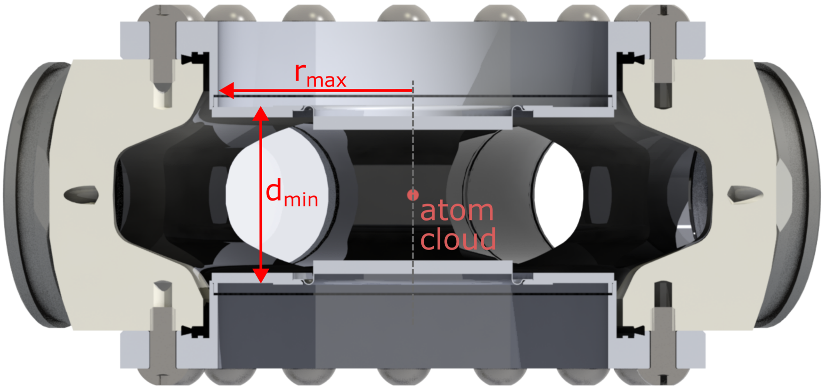

Fig. 3.1. Sectional view of the main chamber with reentrant viewports, the maximum radius $r_{\max}$ and minimal distance $d_{\min}$ the magnetic coils can have due to geometric constraints dictated by the viewport are indicated

3.1 Magnetic Field Configuration and Calculation

Given the geometrical constraints inside the inverted viewport, it is a natural choice to use a pair of round coils, with the same radius r and number of windings N, which share the same symmetry ($z-$) axis (cf. fig. 3.2. These two coils in a pair are driven either by the same or opposite current I. The magnetic field produced along the z-axis by such a configuration (two infinitely thin wire loops), can be calculated via the Biot-Savart law:

$$\boldsymbol{B}(z) = \frac{\mu_0 N I}{2} \cdot \left(\frac{r^2}{\left(r^2 + (z - d/2)^2\right)^{3/2}} \pm \frac{r^2}{\left(r^2 + (z + d/2)^2\right)^{3/2}} \right) \boldsymbol{e}_z, \tag{3.1}$$

with the vacuum permeability μ_0, the distance between the coils d and z being the coordinate along the z-axis, with a reference set at the coil centre. The +/- sign in eq. (3.1) correspond to configurations where the current in both coils circulates in the same/opposite directions, respectively. This yields a situation where the produced magnetic field is nearly homogeneous/a pure gradient, respectively.
For the homogeneous case (fig. 3.2 (a)), it is straightforward to show that the first and second spatial derivation around $z = 0$ are vanishing for the HH-condition

$$d = r \tag{3.2}$$

and the resulting magnetic field at the centre is given by

$$\boldsymbol{B}(0) = \left(\frac{4}{5}\right)^{\frac{3}{2}} \frac{\mu_0 N I}{r} \boldsymbol{e}_z. \tag{3.3}$$

As we want to maximize the flatness of the field produced by the offset coil, we want to be as close as possible to this configuration, because the field has no curvature.

In the case of the gradient coil (AHH-configuration, fig. 3.2 (b)) the second and third spatial derivations of the field (the latter being the curvature of the gradient) are vanishing for

$$d = \sqrt{3} r. \tag{3.4}$$

For this configuration the gradient is roughly 25 % smaller than for $d = r$, but as we aim for maximum uniformity of the gradient this arrangement would be favourable.

Calculating the magnetic field along the z-axis is a simple task due to the symmetry of the problem. For optimizing the geometry of the coils, this is not sufficient and we need to characterize the full 3D-field around the centre of the chamber. Due to the symmetry of the coils, cylindrical coordinates are a natural choice. With the radial coordinate ϕ and axial coordinate z, the magnetic field reads (cf. fig. 3.2 (a)) for the definition of the usual coordinate axis x, y, z:

$$\boldsymbol{B}\left(\boldsymbol{r}\right) = B_\phi \boldsymbol{e}_\phi + B_z \boldsymbol{e}_z, \text{ with } \boldsymbol{e}_\phi = cos(\theta)\boldsymbol{e}_x + sin(\theta)\boldsymbol{e}_y. \tag{3.5}$$

Fortunately, it is possible to get an analytical expression for the field of an infinitely thin circular wire via the complete elliptic integrals of the first and second kind E and K:

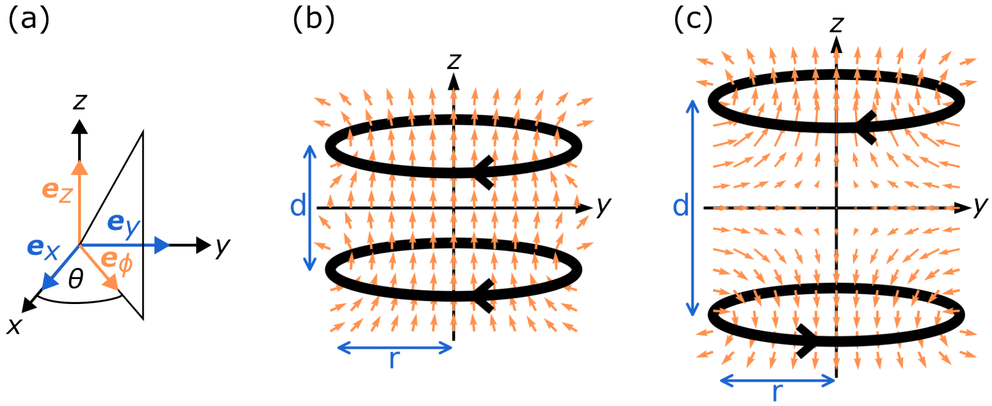

Fig. 3.2. (a) Explanation of coordinate frame: Calculations of the magnetic field are carried out in cylinder coordinates with unit vectors $\boldsymbol{e}_z$ and $\boldsymbol{e}_\phi$, (b)-(c) Schematic representation of two circular magnetic coils symmetric around z-axis with corresponding magnetic field (in orange), the arrows are indicating the current flow direction resulting in an (a) HH-configuration with d = r and (b) AHH-configuration with d = $\sqrt{3}$r

$$
\begin{aligned}
B_\phi &= \frac{\mu_0 I}{2\pi\phi} \frac{z - z_\mathrm{c}}{\left[(r+\phi)^2 + (z-z_\mathrm{c})^2\right]^{1/2}} \left[-K\left(k^2\right) + \frac{r^2 + \phi^2 + (z-z_\mathrm{c})^2}{(r-\phi)^2 + (z-z_\mathrm{c})^2} E\left(k^2\right) \right], \\
B_z &= \frac{\mu_0 I}{2\pi} \frac{1}{\left[(r+\phi)^2 + (z-z_\mathrm{c})^2\right]^{1/2}} \left[K\left(k^2\right) + \frac{r^2 - \phi^2 - (z-z_\mathrm{c})^2}{(r-\phi)^2 + (z-z_\mathrm{c})^2} E\left(k^2\right) \right], \qquad (3.6) \\
k^2 &\equiv \frac{4r\phi}{(r+\phi)^2 + (z-z_\mathrm{c})^2},
\end{aligned}
$$

with z_c the center position of the loop on the z-axis[33, p. 271]. For a coil represented just by one pair of wire loops $z_\mathrm{c} = \pm d/2$ holds true. Based on these formulas, a python class was developed. Each instance of this class represents a specific coil configuration. For the B-field calculation, the field of each wire is calculated by subdividing it into a raster and adding up the respective field contributions. Subsequent adding the fields of each individual wire for both of the coils in the pair leads to full 3D-information of the magnetic field. This approach leads to the possibility of taking into account all kinds of different coil geometries and even specific winding schemes, with the limiting factor that it is still an idealized situation. For example, the wires are not perfect loops around the z-axis, they rather have to perform a spiral-like step in one region of the circumference of the holder (cf. sec. 4.2.1).

3.2 Optimization Strategy for Offset (HH) Coils

As discussed in section 2.4 the requirements for the offset coils (from now on referred to as HH-coils) are higher than for the gradient (AHH-coils). Therefore the focus of the optimization process lies on the HH-coils and after finding the best configuration here the AHH-coils are designed accordingly.

3.2.1 Outer geometry

The field quality, as well as the power consumption (being the most important factor in cooling) of the coil, are in first proximity only dependent on the outer coil geometry, namely radius r, distance d, height H, and width W of the coil (cf. fig. 3.7).

According to equation (3.1), the proportionality equation $B \propto NI$ holds. Let I_1 be the current we would need to create a certain field magnitude for coils of only one winding. The current needed to produce the same field magnitude with N windings and the same outer geometry is given by $I_N = I_1/N$. This can intuitively be understood by the fact that if the coils cross section is filled with N wires with a filling factor of 100 % and a current of I_N, this yields the same current density, and consequently the same magnetic field as with one big rectangular wire filling the same cross-section.
Similar reasoning can be made for the power $P_N = R_N \cdot I_N^2$. The total resistance of the coil is given by

$$R_N = \rho \times \frac{l_N}{A_{\mathrm{wire},N}}, \quad \text{with} \quad l_N = N\, l_1 \text{ and } A_{\mathrm{wire},N} = \frac{A}{N}. \tag{3.7}$$

Here ρ is the resistivity, l_N the total wire length compared to the length of a single winding l_1 and the cross-section of one wire A_{wire} referred to the total coils cross-section $A = H \times W$. If we now put all this together and refer it to the situation of a single wire, we find that the total power of the coil for a fixed target magnetic field is only dependent on the coil's outer geometry:

$$P_N = P_1 = \rho \cdot A \cdot l_1 \cdot I_1^2 \tag{3.8}$$

This is natural given that the current density circulating in the coil to generate a given magnetic field was found to be independent of the wire geometry. Therefore how the cross-section of the coil is filled with wires plays a minor role and it is justified to first optimize the outer geometry.

To discuss the outer coil geometry, we start from the inverted viewport design (fig. 3.1). As distance between the coil and the metal surface of the inverted viewport, we chose 800 µm, which should give us some safety margin to place the coil inside the viewport according to the mechanical workshop of the PI. According to this the minimal distance between the coils $d_{\min}$ and maximum radius $r_{\max}$ are:

$$d_{\min} = 47.4\,\mathrm{mm} \quad \text{and} \quad r_{\max} = 50\,\mathrm{mm}. \tag{3.9}$$

Maximizing A by maintaining a HH-configuration with a square coil would lead to $r_{\mathrm{opt}} = d_{\mathrm{opt}} = 48.7\,\mathrm{mm}$ (referring to coil center), with $H_{\mathrm{opt}} = 1.3\,\mathrm{mm}$ and $W_{\mathrm{opt}} = 2.6\,\mathrm{mm}$. According to formula (3.3) we would need a current of $I_1 = 55\,\mathrm{A}$ to generate a field of 10 G (cf. sec. 2.4), resulting in a current density of $j_{\mathrm{opt}} = 16\,\mathrm{A\,mm^{-2}}$.
At this early design stage, it was very difficult to estimate if we need active cooling at all and what would be a good coil cross-section area which is directly proportional to the power emitted by the coil, according to equ. (3.8). After some reading, the current density turned out to be a good quantity to get a first rough estimate about a reasonable coil geometry. Rough because in the end, it depends a lot on the internal coil structure and also the surrounding of the coil, which is difficult to simulate. The acceptable current

density values for passive air cooling found in literature are in a range of $1.3\,\mathrm{A\,mm^{-2}}$ to $3.5\,\mathrm{A\,mm^{-2}}$ (cf. [34], [35]). That is more than one order of magnitude lower than the value found for the optimal HH configuration.

At this point, we decided to implement active water cooling, but still, we didn't want to have a current density much higher than this range for generating $B = 10\,\mathrm{G}$. Indeed we were concerned about heating so close to the chamber and to sensitive optical paths, in particular as we plan to fit the microscope objective in the viewport reentrance and coil holder. Thus, we wanted to be in a very safe operation mode for the required fields and rather have the potential to go to higher field magnitudes. Consequently, our target current density for generating 10 G should lie close to the passive cooling acceptance, up to a few $\mathrm{A\,mm^{-2}}$.

As a current density of $j_{\mathrm{opt}} = 16\,\mathrm{A\,mm^{-2}}$ was thus not acceptable, it was not possible to have the coils in optimum HH-configuration us and we had to find a compromise between field quality and cooling.

We chose a coil cross-section area and geometry of

$$A_{\mathrm{HH},1} = 16\,\mathrm{mm}^2, \text{ with } H_{\mathrm{HH},1} = W_{\mathrm{HH},1} = 4\,\mathrm{mm}. \tag{3.10}$$

Note that for the cross-section $A_{\mathrm{HH},1}$ the curvature of the magnetic field has a minimum for $W \approx 4.5\,\mathrm{mm}$ and $H \approx 3.6\,\mathrm{mm}$, but the curvature for a symmetric configuration is only 1.2 % higher and as these values will be subject to later fine optimization anyway, they are chosen to be equal for simplicity of the following calculations in this chapter. This leads to a current density of

$$j_{\mathrm{HH},\,1} = 3.4\,\mathrm{A/mm^2} \tag{3.11}$$

at the desired field of 10 G, which is just at the edge of what passive air cooling could potentially be capable of (see discussion above). Of course, this is the situation for one big wire and the current density will increase due to the fact, that we can never achieve a 100 % filling factor (as especially for round wires there will always be some space in between and as the insulation has a certain thickness). Furthermore also the heat conduction in between the wires will affect the situation. But with active water cooling, it should be safely possible to reach the desired field magnitude. A more detailed calculation to confirm this estimate was not possible at this point and had been carried out after fixing the final internal structure of the coil, see sec. 3.2.3).

The coil cross-section area was not solely chosen by considering the cooling properties, still, the main point to keep in mind is the field quality. The magnetic field values are only compared along the z-axis, as the deviation along the x-axis is smaller. To quantify the quality of the field we evaluate, with the method described in section 3.1, the relative difference between the magnetic field value at $z = \pm 1\,\mathrm{mm}$ and $z = 0$ (the centre of the chamber):

$$\delta B_{\pm 1} = \frac{|B(z = \pm 1\,\mathrm{mm}) - B(z = 0\,\mathrm{mm})|}{B(z = 0\,\mathrm{mm})}. \tag{3.12}$$

As presented in table 3.1 the relative field difference is with $\delta B_{\pm 1} = 5.7 \times 10^{-5}$ safely below the desired 1×10^{-4} and leaves some margin for the later optimization process.

$r_{\mathrm{HH},1}$	$d_{\mathrm{HH},1}$	$H_{\mathrm{HH},1} = W_{\mathrm{HH},1}$	B_0	$\delta B_{\pm 1}$
48 mm	51.4 mm	4 mm	9.9 G	5.7×10^{-5}

Table 3.1: Coil outer geometry and properties, field values given for a current of $I_1 = 55\,\mathrm{A}$, B_0 is the field at the center of the chamber and $\delta B_{\pm 1}$ as defined in (3.12)

As the coil itself needs to be placed at a distance of 800 µm, we need a coil that is inherently stable, such that we can remove the supporting structures (needed for winding) to mount them in the viewport. A very convenient choice was here to use self-bonding heat-activated wires (e.g. offered by Elektrisola[1], see also sec. 3.2.4).

3.2.2 Decision on wire geometry (discussion about time response)

After the coil's outer geometry was fixed the next question was how to fill this cross-section with windings. In principle, there are two strategies. First, we could use a high number of windings. The benefits are a lower current to produce the same field and that the in- and outgoing wires play a significantly smaller role in the resulting field, giving a better probably field quality. Second, we could go for a small number of windings, which is easier to wind and often said to have a better time response, as the time response of a coil is strongly influenced by its inductance $L \propto N^2$. If this would actually be the case it would be beneficial for us to use a low number of windings, as the time response is a critical point.

Let's then first discuss this question of the time response versus the number of windings. The time response of the current in a magnetic coil to a step input voltage U_0 is given by:

$$I(t) = \frac{U_0}{R}(1 - e^{-\frac{R}{L}t}), \tag{3.13}$$

with a characteristic time scale of decay set by the ratio $\tau = R/L$ of the resistance and the inductance. For a coil of N windings, the two parameters depend on N. For the resistance, from equations (3.7) follows:

$$R_N = N^2 \frac{\rho\, l_1}{A} \propto N^2. \tag{3.14}$$

For calculation of the inductance an empirical formula derived by professor Perry was used [36]:

$$L_N = 10^{-9} \frac{4\pi N^2 r^2}{0.2317r + 0.44H + 0.39W}\ [\mathrm{H}] \propto N^2. \tag{3.15}$$

From this directly follows that the time constant of equ. (3.13) $\tau_N = \tau_1 = const.$ for a fixed outer geometry of the coil and does in particular not depend on the number of windings.

Another important factor is the needed voltage to generate a given magnetic field and the fast response of its value to a change. To get the same prefactor in equation (3.13), U_0 also has to scale with N^2. But as $B \propto NI$ yields, this relaxes to a scaling of the voltage,

---

[1] Elektrisola Dr Gerd Schildbach GmbH & Co. KG

needed to create the same magnetic field with N. This also matches the intuitive picture, as the power $P = UI$ needed to achieve a certain magnetic field value does not depend on the number of windings.

So the conclusion is that the coils' time response does not depend on the number of windings, as long as one is not limited by voltage. Due to the small size and resulting relatively small resistance of our coils (cf. sec. 3.2.4), the voltage is not limiting in our case. Therefore we decided to use as many windings as feasible to wind in a controlled manner, i.e. without ending up in a random winding.
To decide which wire diameter is still feasible to wind, we did some tests with ∅ 0.5 mm fishing wire (see sec. 4.2.2). As winding with ∅ 0.5 mm-wire was already quite tedious and seemed to be close to the edge of what is possible to wind by hand in a highly controlled way, we decided to use a wire diameter around this value.

3.2.3 Thermal simulation

After deciding on the outer geometry and the approximate wire diameter, we needed to do a thermal simulation, to prove if the coils could actually operate at the desired field strengths. According to our rough estimate in section 3.2.1, this was very likely but still needed to be checked. To perform a more quantitative estimate of the thermal behaviour of the coil, a simplified model of the coil was set up in Solidworks. It was tried to implement the actual round geometry, but Solidworks failed to do a thermal simulation for this. Therefore the coil was approximated as straight bar (see fig. 3.3 (a)). The choice of the coil and wire geometry was oriented on the considerations made in section 3.2.1 and 3.2.2. Also if the values are not exactly matching the final design, this simulation is suited to take qualitative conclusions.

For convective cooling the important parameter is the convective heat transfer coefficient η, for free convection in air this can be in a range of $2.5\,\mathrm{W\,m^{-2}\,K^{-1}}$ to $25\,\mathrm{W\,m^{-2}\,K^{-1}}$ [37]. We chose an intermediate value of $\eta_{air} = 10\,\mathrm{W\,m^{-2}\,K^{-1}}$ for the simulation.

The resistance of our simulation coil, is according to equation (3.7) $R_{\mathrm{sim}} = 1.7\,\Omega$, with the resistivity of annealed copper being $\rho_{\mathrm{Cu},20} = 1.72\,\Omega\,\mathrm{m}$ at 20 °C [38]. Here we do not take into account the temperature dependence of the resistivity. Note that within the temperature range of the simulation, the maximum change in resistivity is estimated to be around 10 %, which is a small change compared to the level of approximation in this simulation. The temperature dependence of the resistivity ρ can be approximated by the linear relation

$$\rho(T) = \rho_{\mathrm{Cu},20}\left[1 + \alpha_{20}\left(T - 293\,\mathrm{K}\right)\right], \tag{3.16}$$

with $\rho_{\mathrm{Cu},20} = 1.72\,\Omega\,\mathrm{m}$ the resistivity of enamelled copper at 20 °C and $\alpha_{20} = 3.9 \times 10^{-3}\,\mathrm{K^{-1}}$ the linear temperature coefficient at this temperature [38].

To produce a field of 10 G with a coil close to the configuration in table 3.1 we need a current of $I_{64} = I_1/64 = 0.9\,\mathrm{A}$, resulting in a power of $P = RI^2 = 1.3\,\mathrm{W}$.
The first simulation done was just with air convection at all four sides at this power level.

It results in a maximum temperature of $T = 43.3\,^\circ\mathrm{C}$ (see fig. 3.3 (b)). The real situation is expected to be better, as the total convective cooled area will be increased with the coil holder. But as discussed we would like to be in a very safe working regime at 10 G with no significant heat up of the coils. For this aim, we need water cooling.

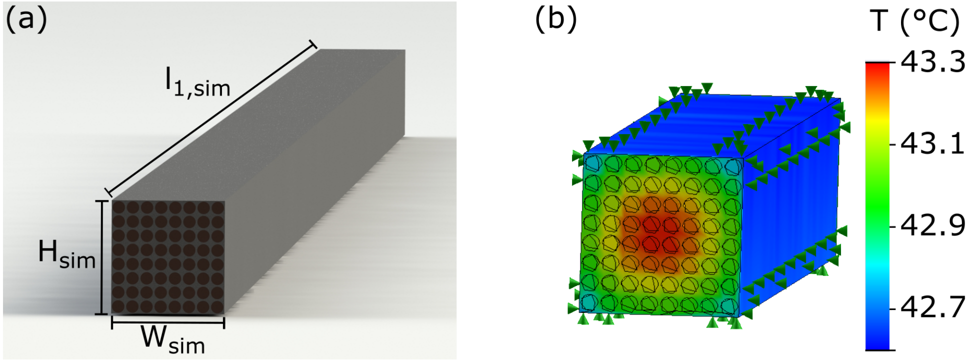

Fig. 3.3. Thermal simulation of the coil: (a) Simplified coil with $l_{1,\mathrm{sim}} = 2\pi r_{\mathrm{HH},1}$, $H_\mathrm{sim} = W_\mathrm{sim} = 8 \times \varnothing_{\mathrm{w,\ sim}}$ ($\varnothing_{\mathrm{w,\ sim}} = 0.568\,\mathrm{mm}$, $\varnothing 0.5\,\mathrm{mm}$ Cu core) and thermal conductivities of copper $k_\mathrm{Cu} = 401\,\mathrm{W\,m^{-1}\,K^{-1}}$ [39] and the insulation $k_\mathrm{ins} = 0.3\,\mathrm{W\,m^{-1}\,K^{-1}}$ [2], (b) thermal simulation for power of $P = 1.3\,\mathrm{W}$, corresponding to the power needed to generate a field of $B = 10\,\mathrm{G}$ (see text), with convective cooling on all four long sides

The next simulations were done with the most simple implementation of a water cooling. The two sides of the coil being in contact with the holder were set to a constant temperature of $T = 16\,^\circ\mathrm{C}$ (temperature of institute water cooling line). This approximation is especially valid for low powers and becomes worse when approaching the limit of heat which can be carried away by the water. To get a feeling for the order of magnitude of this value, we calculate the heat change of the water flowing through the coil holder.

The heat energy Q needed to increase the temperature of an amount of water with a mass m_w and heat capacity $c_\mathrm{p,w} = 4184\,\mathrm{J\,kg^{-1}\,K^{-1}}$ [40] by ΔT is given by $Q = m_\mathrm{w} c_\mathrm{p,w} \Delta T$ [41, p. 294]. By taking the time derivative, we get a steady state equation for the heat carried away by a water mass flow of $\dot{m}_\mathrm{w}$:

$$\dot{Q} = \dot{m}_\mathrm{w} c_\mathrm{p,w} \Delta T. \tag{3.17}$$

The mass flow is determined by the height $h_\mathrm{ch} = 4.7\,\mathrm{mm}$ and width $w_\mathrm{ch} = 3.2\,\mathrm{mm}$ of the water channel in the coil holder (cf. sec. 4.1.1, eq. (4.1)) and v_w the flow velocity of the water:

$$\dot{m}_\mathrm{w} = \rho_\mathrm{w} h_\mathrm{ch} w_\mathrm{ch} v_\mathrm{w}, \tag{3.18}$$

with $\rho_\mathrm{w} = 1000\,\mathrm{kg\,m^{-3}}$ [40] the mass density of water. For this calculation we chose $\Delta T = 2\,^\circ\mathrm{C}$ and $v_\mathrm{w} = 1\,\mathrm{m\,s^{-1}}$, as values which seem reasonable, resulting in a heat change of $\dot{Q} = 130\,\mathrm{W}$, giving an idea of the order of magnitude of the maximum cooling capacity of our water cooling.

---

[2] Data of standard self-bonding wires from Elektrisola, the company from which we ordered our final wire (see sec. 3.2.4)

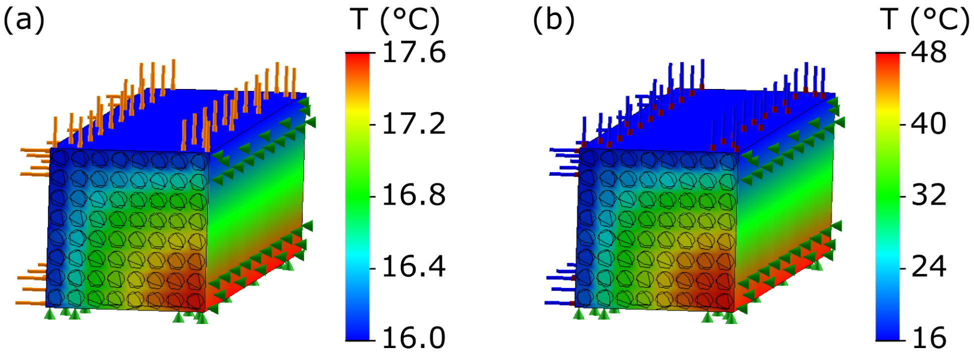

Fig. 3.4. Thermal simulation of the coil with water cooling (fixed temperature of T = 16°) at two sides and convective cooling at the two others and a power of (a) 1.3 W ($B = 10\,\mathrm{G}$) and (b) 30 W ($B \approx 47\,\mathrm{G}$)

As it is two orders of magnitude lower than this estimate, for a power of 1.3 W the hypothesis made in our simulation seems legitimate. With this load, we observe that the coil does not significantly heat up (cf. fig. 3.4 (a)). This result assures that the desired fields can be reached without a problem when using water cooling.

Thanks to the water cooling we can also think to go to larger field values than the designed value of 10 G and this possibility will be beneficial for experiments, as e.g. more FRs can be used. As maximum temperature which might be still acceptable, we agreed on a value roughly around 50 °C. Note that however, this might already be a critical temperature due to possible heating of the chamber and convective air flow influencing the imaging. This temperature is reached at a power of approximately 30 W, corresponding to a magnetic field of $B \approx 47\,\mathrm{G}$ (see fig. 3.4 (b)), the resistance change with temperature is again not taken into account for the conversion from power to field.

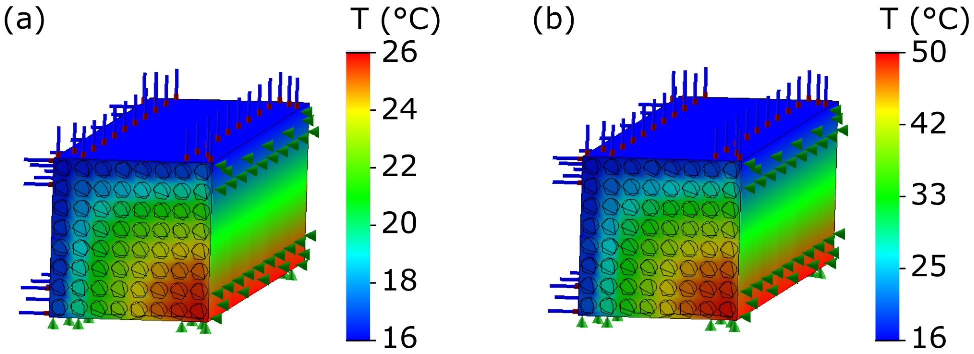

Fig. 3.5. Thermal simulation of the coil with water cooling (fixed temperature of T = 16°) at two sides and convective cooling at the two others, with a thermal conductivity of $k_{ins} = 1\,\mathrm{W\,m^{-1}\,K^{-1}}$ at a power of (a) 30 W ($B \approx 47\,\mathrm{G}$) and (b) 100 W ($B \approx 85\,\mathrm{G}$)

Furthermore, the field range can be further increased by a convenient choice of wires, in figure 3.5 a similar simulation is set up with an increased value for the heat conductivity of the insulation of the wire, showing a significantly better thermal behaviour. The temperature of 50 °C is reached at a magnetic field value of $B = 85\,\mathrm{G}$ (fig. 3.5 (b)). From comparing figure 3.4 and 3.5 we can conclude that, as long as we are still in a regime, in which our water cooling is capable of carrying away the power, the limiting factor of the coil's temperature is the heat conductivity of the wire's insulation.

Due to this we finally decided on a special type of wire from Elektrisola, which has a special heat conductive insulation. It is not clear which thermal conductivity the wire finally has (as it is still in its testing phase), but according to a sales document from Elektrisola, it is said to have up to 50 times higher thermal conductivity, depending on the grade of modification (see app. A.1). Therefore we can not do a quantitative analysis here and also it is very questionable how valid this simulation is for such high powers, but the conclusion we can take from figure 3.5 (b) is that we will probably be able to reach significantly higher fields as required, which will certainly be favourable in the future. This will be tested in section 5.1.

3.2.4 Final Helmholtz-coil configuration

After deciding on the approximate outer coil geometry and wire diameter, the final optimization step was to calculate all possible coil configurations around these roughly fixed constraints and decide on one. The minimum distance of the coils was with $d_{\mathrm{min}} = 47.4\,\mathrm{mm}$ directly taken out of section 3.2.1. The coils height and width were calculated by considering an ideal orthocyclic winding scheme (see sec. 4.2.1 and fig. 3.6). To take into account that with this winding scheme the coils width is 5 % to 10 % larger at the wire crossing region, and that we need space for one outgoing wire also in this region (see sec. 4.1.1), the outer radius was reduced by another 0.5 mm to $r_{\mathrm{max}} = 49.5\,\mathrm{mm}$, leaving a total radial gap of 1.3 mm in the idealized winding scenario.

Three specific wire geometries, offered by Elektrisola, closest to the ∅0.5 mm decided on in section 3.2.2, where taken into account (see table 3.2, Wire 1 - 3). The important values on which the final decision was based are the field quality, measured by the relative field difference around the centre $\delta B_{\pm 1}$ (see equ. (3.12)), and the power needed to produce a field of 10 G, $P_{10\mathrm{G}}$. These values were calculated for all configurations with 6, 8 and 10 layers (radial number of wires) and 7, 8 and 9 windings (axial number of wires). Only odd number of layers were taken into account, as the coil winding starts at the top of the coil and we wanted it to also and at its top to minimize the influence of the in- and out-coming wire (cf. sec. 4.2.3). Note that a configuration with e.g. 8 layers and 8 windings corresponds to a total N of 60, as the number of windings is one smaller each second layer (cf. fig. 3.6).

	Wire 1	Wire 2	Wire 3	Final wire
Core diameter (mm)	0.450	0.475	0.500	0.500
Outer diameter (mm)	0.514	0.543	0.568	0.546

Table 3.2: Standard sizes for self-bonding wires (Wire 1 - 3) and geometry of final custom-made wire, all from Elektrisola

Only coil configurations with a cross-section area above 16 mm^2 were taken into account. Indeed, even if the thermal simulation in section 3.2.3 gives us reason to be optimistic about the thermal behaviour if we use water cooling, but as we are able to match the

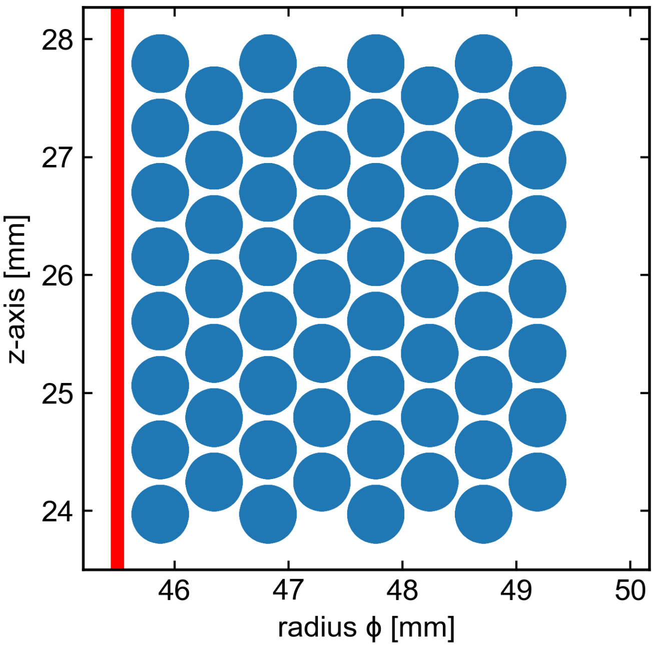

Fig. 3.6. Final winding scheme of HH-coil with 8 layers and 8 windings (one less every second layer), in red the coils winding surface is indicated

requirements on field quality without further reducing the coils cross-section, we kept the constraint fixed in section 3.2.1 to assure safe operation and increase the potential to go to higher fields.

All tested configurations with the corresponding field quality and power values are presented in table 3.3. For all this configurations the span for $\delta B_{\pm 1}$ is 6.7×10^{-5} to 9.8×10^{-5} and for $P_{10\mathrm{G}}$ 0.9 W to 1.5 W. We chose a configuration using Wire 3 with 8 layers and 8 windings, marked bold in table 3.3). It has an intermediate field quality of $\delta B_{\pm 1} = 7.7 \times 10^{-5}$ not so far from the best value achieved, still safely matching our requirement of $\delta B_{\pm 1} < 1 \times 10^{-4}$ (sec. 2.4, and also an intermediate power $P_{10\mathrm{G}} = 1.3\,\mathrm{W}$ compared to the other configurations. In the decision process, the simplicity of the winding procedure was also given a rather high value, therefore the final configuration, having 8 layers was preferred over a configuration with wire 2 and 10 layers, even if the latter has slightly better field quality and the same power.

We finally chose a custom-made heat-activated, self-bonding, enamelled copper wire from Elektrisola, which had an even smaller outer diameter of $\varnothing\,0.546\,\mathrm{mm}$, by maintaining the same core diameter of $\varnothing\,0.5\,\mathrm{mm}$. This further reduced the field quality by reducing $\delta B_{\pm 1}$ to 7.3×10^{-5} (cf. tab. 3.5), by maintaining the value for $P_{10\mathrm{G}}$. Due to the self-bonding property of the wire, we can bake the coil (sec. 4.3) and after cooling down it is inherently stable. This self-binding property is needed to reach the desired coil configuration as already discussed in section 3.2.1. In figure 3.7, it can be clearly seen, that there is no space in the axial direction between the coil and the viewport for a supporting

		$ll = 8$ $ww = 7$	$ll = 8$ $ww = 8$	$ll = 8$ $ww = 9$	$ll = 10$ $ww = 7$	$ll = 10$ $ww = 8$	$ll = 10$ $ww = 9$
Wire 1	$\delta B_{\pm 1}(10^{-5})$	×	×	7.4	6.7	7.6	8.4
	$P_{10\mathrm{G}}(\mathrm{W})$			1.4	1.5	1.3	1.1
Wire 2	$\delta B_{\pm 1}(10^{-5})$	×	7.2	8.0	7.4	8.3	9.1
	$P_{10\mathrm{G}}(\mathrm{W})$		1.4	1.3	1.3	1.1	1.0
Wire 3	$\delta B_{\pm 1}(10^{-5})$	×	**7.7**	8.6	7.9	8.9	9.8
	$P_{10\mathrm{G}}(\mathrm{W})$		**1.3**	1.1	1.2	1.0	0.9

Table 3.3: Final HH-coil configuration decision: Relative field quality $\delta B_{\pm 1}$ and power $P_{10\mathrm{G}}$ needed for 10 G for the three tested wires (cf. tab. 3.2) for different number of layers ll and windings ww, crossed configurations have cross-section area smaller 16 mm^2

structure. Additionally, the wire offered a special highly heat conductive insulation to allow larger fields as discussed in 3.2.3.

The idealized final coils winding scheme can be seen in figure 3.6 and the final coil configuration in figure 3.7. Here also an additional coil (pair), the SF-coil consisting of one winding of the same wire, is shown in yellow. This coil can be used as an radio frequency (RF) antenna despite its symmetry around the z-axis might hinder us to induce the desired transitions, but there was no argument against just implementing it in the most convenient way and testing it. Furthermore, it could be of potential interest for really fast field jumps or small amplitude modulations, as due to its smaller diameter there will be less induced eddy currents. All important geometric coil parameters are summarized in table 3.4 and the corresponding coil properties in table 3.5. Also, the parameters for the AHH-coil, which will be discussed in the next section (3.3), are presented here. A plot of the final calculated magnetic field of the HH-coil can be seen in figure 3.8.

	d (mm)	r (mm)	H (mm)	W (mm)	windings (axial)	layers (radial)	N
HH	51.8	47.5	4.4	3.9	8	8	60
AHH	68.9	47.5	8.7	3.9	16	8	123
SF	47.9	38.7	0.5	0.5	1	1	1

Table 3.4: Geometry of HH-, AHH and SF-coil (cf. fig. 3.7)

3.3 Optimization of Gradient (AHH) Coils

As discussed in section 2.4 the homogeneity of the gradient was not as crucial as the field quality of the HH-coils. Therefore the AHH-coils were designed after the HH-coils and have been strongly adapted to outer constraints, making it impossible to be close to the optimum (in terms of gradient homogeneity) configuration $d = \sqrt{3}r$ (eq. (3.4)). The main restriction here was the desire to keep side optical access (at large angle $\sim 41°$), forcing

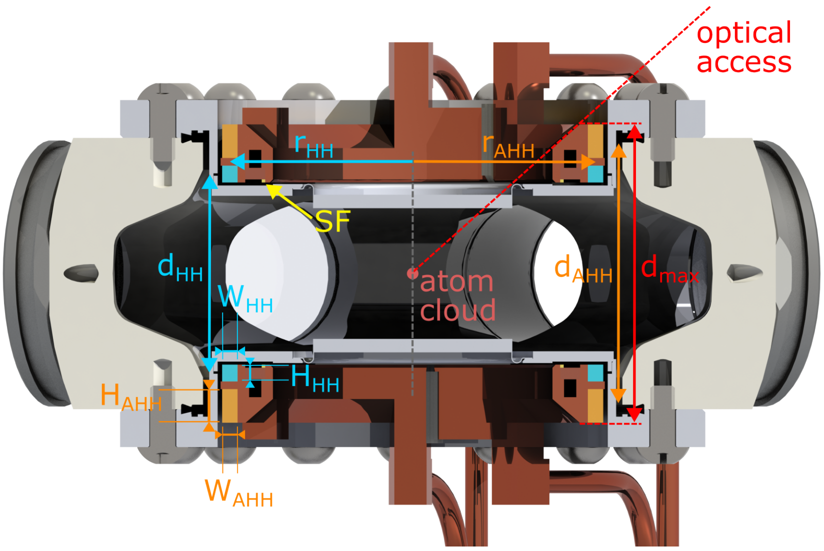

Fig. 3.7. Sectional view of main chamber with reentrant viewports and final configuration of HH- (blue) and AHH- (orange) coil with corresponding parameters (see text), small field (SF)-coil is depicted in yellow

	z- field/gradient @ center	rel. diff. $\pm 1\,\mathrm{mm}$	rel. diff. $\pm 19\,\mathrm{mm}$	R_{pair}	L_{pair}	Power @ 1 A
HH	10.75 G/A	7.3×10^{-5}	8.0×10^{-4}	3.16 Ω	1.61 mH	1.6 W
AHH	5.17 G/(cm A)	4.5×10^{-4}	21 %	6.49 Ω	5.69 mH	3.2 W
SF	0.2 G/A	2.8×10^{-4}	3.8 %	38 mΩ	0.4 µH	21 mW

Table 3.5: Properties of HH-, AHH and SF-coil: relative differences in magnetic field/gradient are given along z-axis, resistance R_{pair} (@ 22 °C)and inductance L_{pair} per pair of coils in series and power for a single coil of configuration

us to significantly reduce the coils distance out of optimum to a maximum distance of $d_{\mathrm{max}} = 77.6\,\mathrm{mm}$ (see fig. 3.7). We chose to use the same wire, as the discussion in section 3.2.2 is also valid for the AHH-coil. Also here the self-binding property of the wire is very useful, as we don't need a supporting plate at the top, making it possible to make use of all available space up to d_{max}. The constraint for the outer radius stays with $r_{\mathrm{max}} = 49.5\,\mathrm{mm}$ the same than for the HH-coil (cf. sec. 3.2.4). It was easiest to just wind the coil on the same inner radius than the HH-coil. Note that, on the one hand, reducing the inner radius wouldn't have made sense, as this would even lead to further decreased gradient homogeneity. On the other hand, further increasing it would lead to a decreased coils cross-section, with consequent worse thermal behaviour.

Under reserve that the requirements to the gradient will be met (discussed below), these considerations directly lead to a final AHH-coil design. The width and consequently the number of layers, as well as the radius, is identical to the of the HH-coil. According to the thermal discussion (see discussion below) it was clear, that we needed to make use of the full available space to maximize the coil's cross-section, by using all available space.

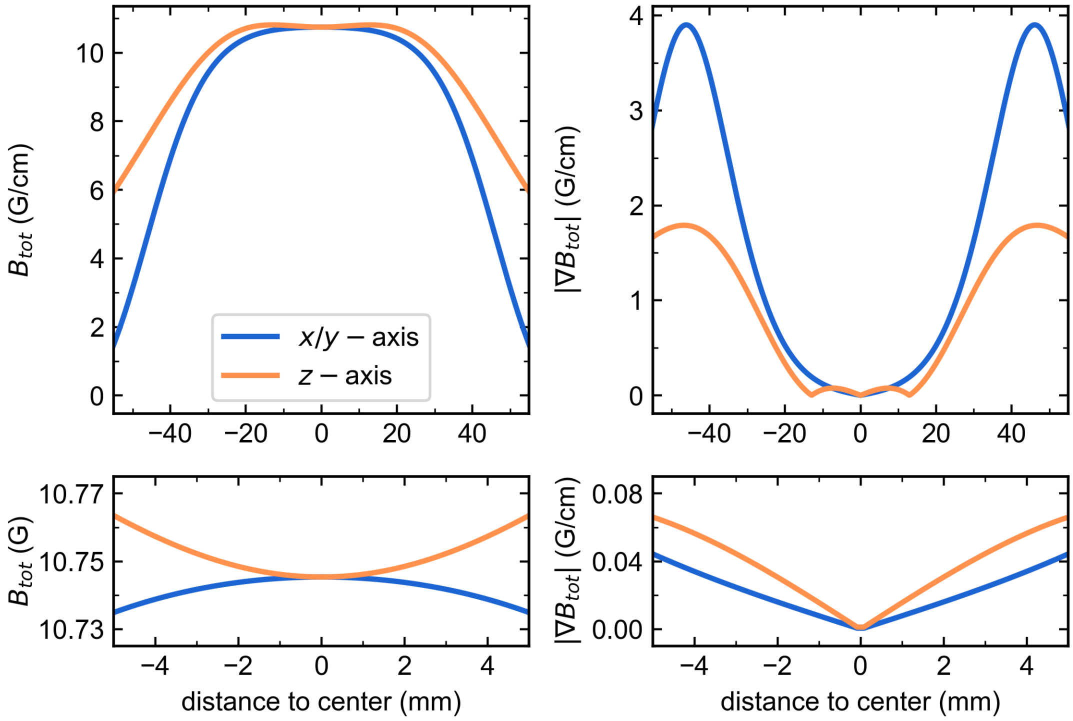

Fig. 3.8. Calculated total magnetic field B_{tot} in left column and gradient $|\nabla B_{\text{tot}}|$ in right column of HH-coil, in orange along the z-axis and in blue along an arbitrary axis in the xy-plane, for a current of $I = 1\,\text{A}$ (see table 3.5 for field characteristics)

This led to a winding number of 16 (15 each second layer) and therefore to a total N of 124. Actually, in practice, for one coil we had a problem with fitting it into the inverted viewport and therefore removed one winding from all coil holders, resulting in a final $N_{\text{AHH}} = 123$. All final values are presented in table 3.4 and 3.5.

What needs to be checked is, if it is possible to achieve the desired gradient values at a decent temperature. To achieve the minimum requirement, being a gradient of $dB/dz = 6\,\text{G/cm}$ (sec. 2.4), we need a current of $I = 1.2\,\text{A}$ corresponding to a power of $P = 4.4\,\text{W}$ for one coil (cf. table 3.5). Even if the thermal simulation carried out in section 3.2.3 was not done for the AHH-coil geometry, we can still conclude from it. As the simulated cross-section is approximately half of one of the AHH-coil, the thermal behaviour will certainly be better. In figure 3.4 it was simulated with water cooling for a power of 1.3 W (a) and 30 W (b), showing no significant heating in the first case and still probably acceptable heating in the second. As the questioned power of 4.4 W is much closer to the situation in (a), we can safely conclude that we can reach this gradient, especially as due to the enhanced heat conductivity of the wire the situation might be more similar to the one simulated in figure 3.5 and that the power needed to be dissipated in the end strongly depends on the duty cycle, which, in particular for the gradient case, will be definitely much lower than the here-assumed scenario, in which the coils are always turned on. Therefore it is highly likely, that we can achieve much higher gradient values, which would be favourable according to the discussion in section 2.4.

A final field and gradient plot can be seen in figure 3.9. For the gradient field, an interesting point to comment on the quality of the field is the gradient homogeneity in a region ±19 mm around the centre, as this is the optimum size of our 3D-MOT cooling region (limited by the clear aperture of our viewport). Simulations of the MOT loading carried out by Jianshun Gao indicate, that a relative difference of 21 % (see tab. 3.5) have no significant influence on the MOT loading rate [32].

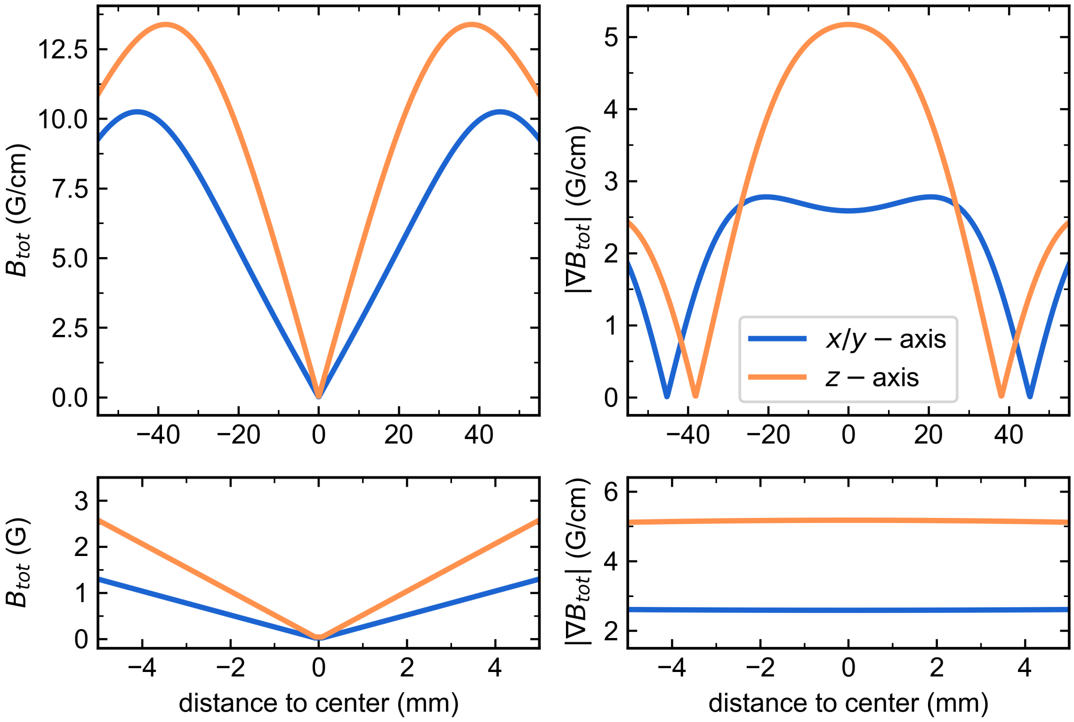

Fig. 3.9. Calculated total magnetic field B_{tot} in left column and gradient $|\nabla B_{\mathrm{tot}}|$ in right column of AHH-coil, in orange along the z-axis and in blue along an arbitrary axis in the xy-plane, for a current of $I = 1\,\mathrm{A}$ (see table 3.5 for field characteristics)

3.4 Power supply

Another limitation to the field quality, besides the configuration of the coils itself, comes from the noise in the current that circulates through the coils. This is generated by the power supply, which we did not want to be the limiting factor in precision and therefore wanted relative current stability safely below 1×10^{-4}, aiming for 1×10^{-5}. According to experience from other groups, the timescale limitation to switching magnetic fields is limited by eddy currents in the metal chamber in the order of 1 ms. We wanted the power supply itself to reach the desired current value in the coil much faster than that, to be sure to not be limited by the power supply. Also, this gives rise to the potential option to actively feedback the magnetic field at some point and therefore get a time response of the magnetic field not limited by the mentioned time scale of eddy currents.

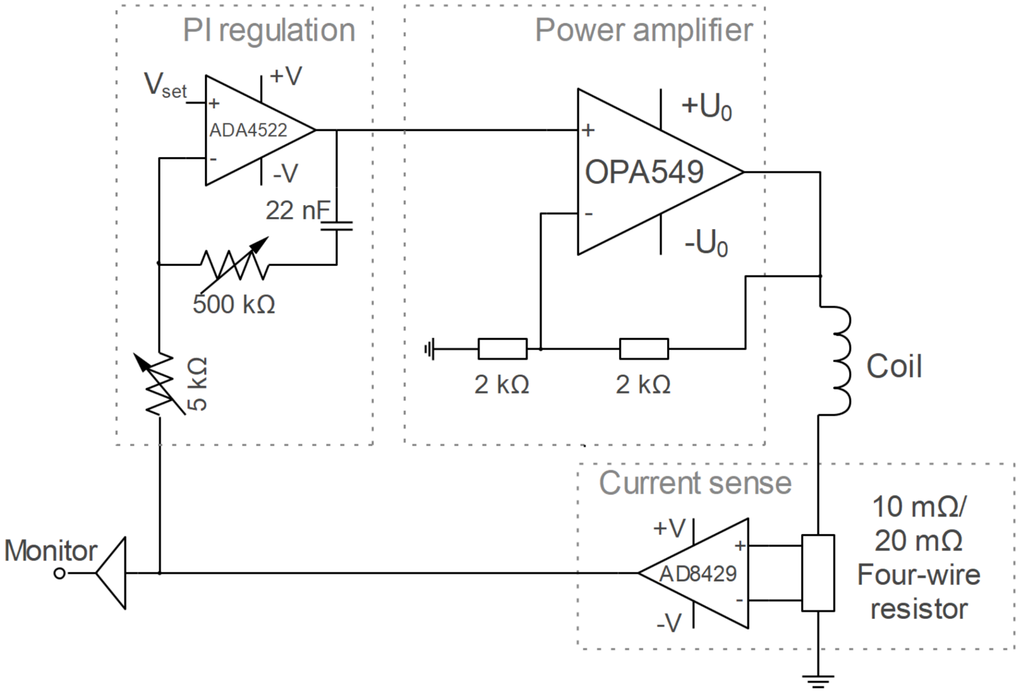

Fig. 3.10. Schematic electronic drawing of home-built power supply

It was not easy to find a commercially available power supply matching these requirements. The only supplies found matching them were produced by the company High-Finesse and are very pricey. As we found a very promising operational amplifier (op amp)-based solution [42], we decided to use a home-built power supply based on this. Design and building of a first prototype was done in the scope of the bachelor thesis of Lennart Hoenen [17]. A simplified version of the power supply can be seen in figure 3.10. The core part of the supply is the high-voltage, high-current op amp, which can deliver a continuous output current of 8 A (10 A peak) and an output voltage up to ±25 V to ±28 V (depending on the load) for the maximum $U_0 = 30\,\mathrm{V}$ in bipolar operation mode [43]. In the pictured configuration input of 1 V corresponds to an output of 2 V delivered to the coil, generating a current depending on its resistance. This current is measured via the voltage drop over a small 10 mΩ or 20 mΩ (depending on the version of the supply) four-wire shunt resistor, which is amplified by another op amp by a factor between 100 to 600.
The amplified voltage is then finally fed back into a PI control loop, which regulates the input voltage to the Power amplifier such that the set voltage V_{set} corresponds to the desired current through the coil. Note that the combination of measurement resistor and gain finally sets the mapping of the input voltage V_{set} to the set current.

With this power supply, we achieved a stable ±5 A (currently limited by the power rating of our measurement resistor), with a relative RMS noise below 2.5×10^{-5}, which was the measurement limit of the oscilloscope [17]. A full turn on/off of the magnetic field of the HH-coil to/from the required 10 G was achieved in ~50 µs (cf. sec. 5.2). Therefore all of our requirements were fulfilled and our electronic workshop will build a rack-mounted version of this supply, having five separate output channels, with slightly different current ranges, to power all four pairs of magnetic coils around the main chamber.

4 | Coil Manufacturing

As the design of the magnetic coils was fixed in the last chapter, the next step was the design of the coil holder and the subsequent manufacturing process. In this chapter, a detailed description of this manufacturing process, which includes the holder manufacturing, as well as winding and baking the coil, is provided.

4.1 Coil Holder

4.1.1 Holder design

The design process of the holder took place in parallel with that of the coils, as it was always an interplay between what coil configuration we wanted to achieve, and what is technically feasible. As holder material copper was chosen, as it is perfectly suited to mediate the action of water cooling due to its high thermal conductivity. Also, it is very favourable to have a coil holder material with the same thermal properties as the wire (see sec. 4.4). One of the very first considerations was if it is possible to manufacture a coil without a top or bottom plate, by attaching them during the winding process, baking the coil, thereby fixing its structure, and afterwards removing these plates. This was successfully evaluated before the following design process (see sec. 4.2.2).

Given the coils geometry and the geometrical constraints fixed by the viewport, the evaluation of most outer geometries of the coil holder was straightforward. Referring to figure 4.1, the outer radius r_{out} is given via the earlier discussed constraint of having a distance of 800 µm to the viewports surface (cf. sec. 3.2.1). The radius r_{in}, on which the coils are wound, directly follows from the coils geometry (cf. tab. 3.4). Same applies for the winding heights h_{HH} and h_{AHH}, which were set exactly to the height of the coils, as this worked well in preceding winding tests (cf. sec. 4.2.2). During the final winding process it turned out in fact, that here an additional height of ∼150 µm would have been favourable, but it was possible to compensate for this issue (see sec. 4.2.3).
The height H_{h} directly follows from the coils heights and the positions, the total height H_1 from the holders positioning (also 800 µm above the viewport) and the geometry of the polyether ether ketone (PEEK)-mounts. The width W_{h} is limited by the edge e_1 of the inverted viewport, with which we did not want to overlap (to keep the previously fixed distance to the viewport), therefore also the edge from the holder at this position was chamfered. The top-bevelled geometry was adapted to the optical access line.

The size of the water channel was then consequently chosen, with a minimum copper material thickness of ∼2 mm everywhere, which seemed to be a safe value in terms of

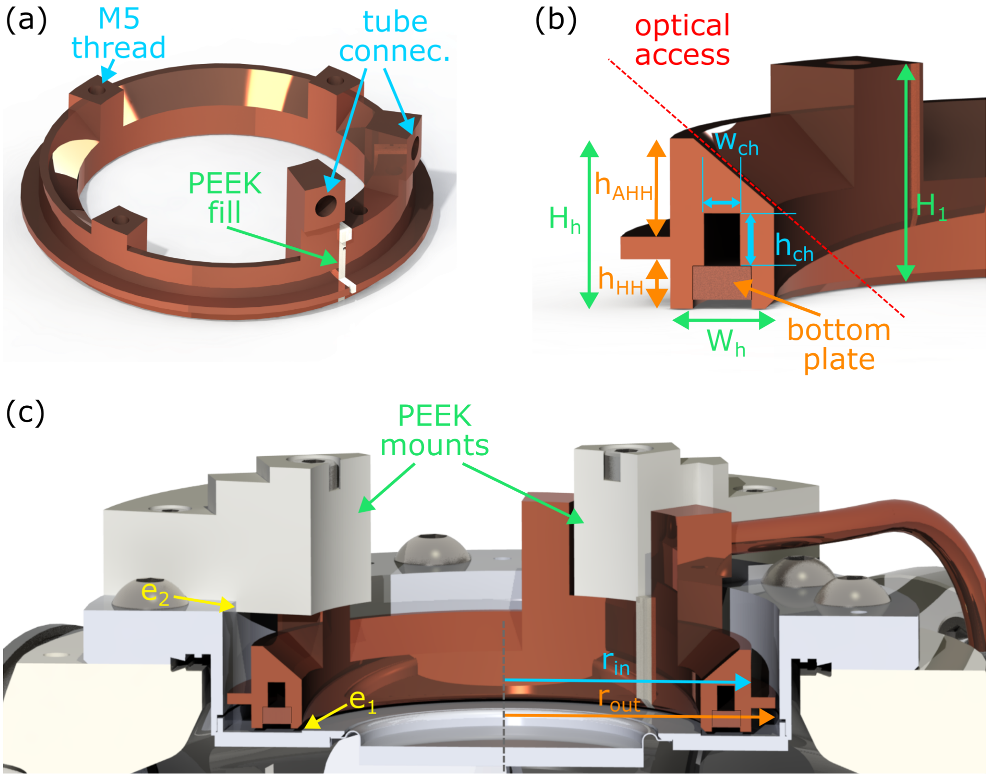

Fig. 4.1. Coil holder design: (a) top view, (b) cross-section close-up, (c) cross-section of holder mounted in inverted viewport

stability and also leakage, to be:

$$h_{\mathrm{ch}} = 4.7\,\mathrm{mm} \quad \text{and} \quad w_{\mathrm{ch}} = 3.2\,\mathrm{mm}. \tag{4.1}$$

This water channel is closed, via soldering or welding (see sec. 4.1.2), with a separate copper bottom plate, leaving space for the SF coils (cf. fig. 3.7). The channel surrounds the holder by a total angle of ∼320°, going over into two vertical round channels here and ending up in two radially outgoing round holes, the tube connections in figure 4.1 (a). Into this connections tubes are soldered after the winding process (see fig. 4.3). We decided to solder tubes into the holder rather than having some kind of water connection directly at the holder because we wanted to do these connections at a safe distance from the inverted viewport to minimize leakage probability close to it, as leakage at this point could for example irreversibly damage the viewports coating. The tubes are bent such that we can do all the water connections far away from the experiment below the main breadboard (cf. fig. 4.11). As water connections, we decided on using the Gyrolok tube fitting system from Hoke (similar to the Swagelok system), which is known for its quality and reliability. With this, we connect the 6 mm copper tube to a 8 mm hose. A full technical drawing of the coil holder with all its measures can be found in appendix A.2.

Another major point in the design are grooves in the winding surface of the holder to achieve an orthocyclic winding scheme (cf. sec. 4.2.1). The grooves force the wire into the scheme seen in figure 4.4 (b). They start at the income point of the wire leading clockwise (from the top), fully parallel to the holders' flange around the holder over a total angle of

315°, at this point, it is no longer parallel but performs a step of exactly one wire width over the remaining 45° to end up below the starting point of the upper groove. From there the same process starts again until the whole surface is covered (see fig. 4.3).

The holder has a slit to prevent for circular eddy currents (fig. 4.1 (a)). This slit is filled by a small PEEK part, which also fulfils the role of guiding the incoming (and also the outgoing for SF coil) wires to their right position (fig. 4.2). It has the other advantage that the incoming wires are not bent around a sharp metal edge, which would highly likely damage its insulation, causing a short with the holder, but over an additionally rounded plastic edge. PEEK is used because of its high thermal resilience, essential for baking the coil, its high mechanical strength and its low inflammability (important for safety reasons in the experiment) [44].

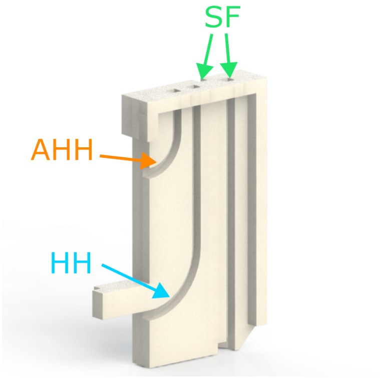

Fig. 4.2. PEEK holder slit filling with wire channels

To mount the holder into the inverted viewport four M5-threads are cut into four additionally exposed square structures (see fig. 4.1 (a)). The mechanical connection to the main chamber is realized by four PEEK mounts (see fig. 4.1 (c)). The resulting electric insulation between the holder and the chamber might be again beneficial to reduce eddy currents. The PEEK-mount secures the alignment of the coil holder due to its edge e_2, having the same radius as the inner radius of the inverted viewport. These parts are highly customized to additionally function as a mount for the two pairs of rectangular coils (see fig. 4.11).

4.1.2 Holder manufacturing

The rather complicated process of manufacturing the coil holder was done by the mechanical workshop of the PI[1]. In total, they manufactured four holders, such that we have some in spare to account for possible failure. The rough structure of the main part of the holder was cut out of a round copper bar via a computerized numerical control (CNC)-machine. Afterwards, the bottom plate was attached to the holder. For the first three holders, it was hard soldered. The last one was welded, which later turned out to be an easier process according to an employee of the workshop. Because the temperature to which the holder is exposed during this process slightly changes its measures, it was needed to manufacture the exact geometries, especially the ones being in contact with the coil and therefore needed to be highly precise, afterwards. As a final step, the grooves were manufactured with the same CNC-machine. For this process, it was crucial that the holder does not have a top and bottom plate, as it was needed to access the winding surfaces from this direction with a rotating cutting tool. The final coil holder before the winding process can be seen in figure 4.3.

After the winding and baking process, which will be described in detail in the next sections (4.2.3, 4.3), the last step was to (soft) solder the tubes into the holder. They were

---

[1] Physikalisches Institut Heidelberg

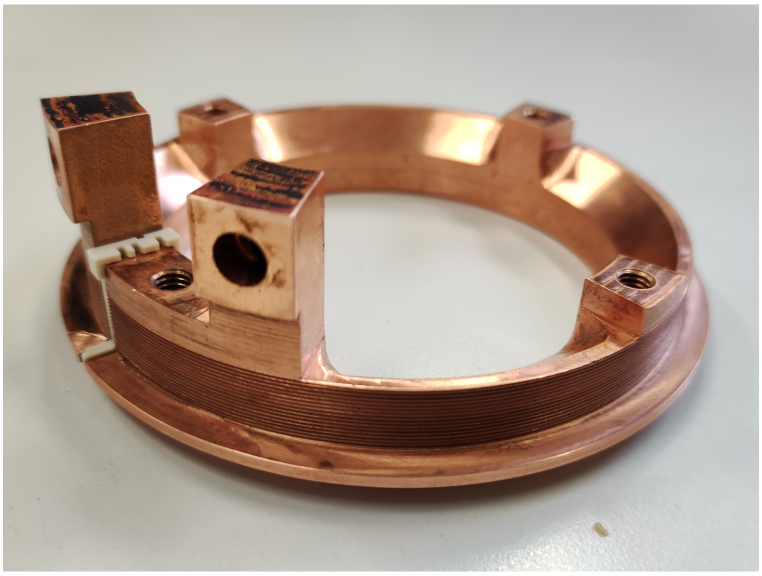

Fig. 4.3. Final coil holder

bent before this process into the right shape, to avoid putting too much stress onto the soldering connection and only do slight corrections at the experiment site after installation.

4.2 Coil Winding

4.2.1 Orthocyclic winding scheme

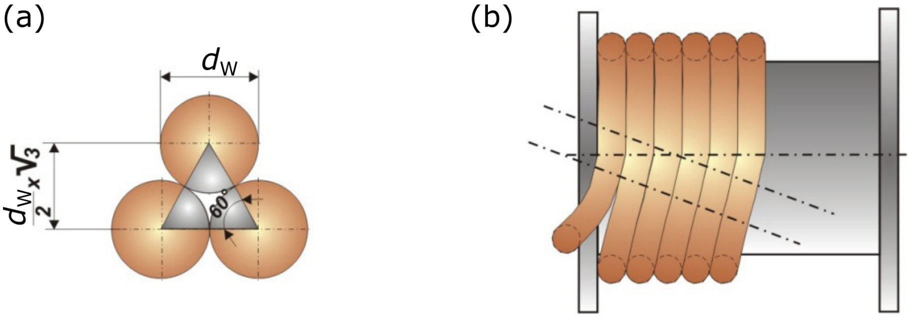

Fig. 4.4. Schematic of orthocyclic winding scheme: (a) Optimum filling ratio, (b) Visualization of the first layer (figure taken from [45, p. 147])

The most controlled winding technique is the orthocyclic winding scheme. Here the conductors are wound mostly parallel to the coil flange. After one winding the wire needs to make a step (in the axial direction) of one wire diameter size to the next winding (cf. fig. 4.4 (b)). This step needs to be performed within a range of 30° to 60°, otherwise, the wire will lose its self-guiding behaviour and a random winding is produced. The next layer (in the radial direction) is then laid into the valleys of the layer beneath but needs to cross the wires where the inner layer does the step. This region is called the crossover zone. At this point, the coil has a 5 % to 10 % higher width according to empirical findings. [45,

pp. 146–152]
It can easily be calculated that with this winding scheme one can theoretically get a filling factor of 90.7 % outside the crossing region (cf. fig. 4.4 (a)).

Furthermore one needs to think about the number of windings (axial) per layer (radial). As seen in fig. 4.5 one option is to start with covering the full coil width in the first layer and then alternately have one winding less per layer.

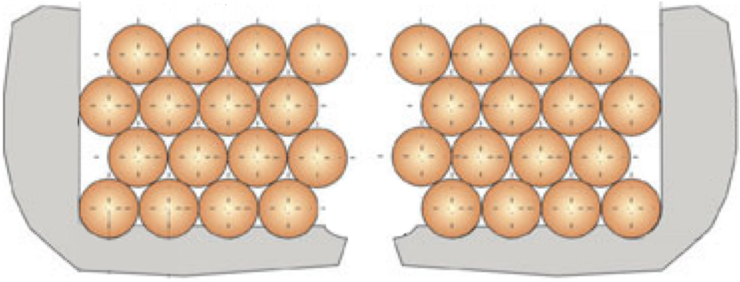

Fig. 4.5. Schematic representation of alternating layering in orthocyclic winding scheme (figure taken from [45, p. 149])

4.2.2 Winding tests

One of the most important questions in the decision about the wire geometry was, what is feasible to wind in a highly controlled way (sec. 3.2.2). Therefore we performed some winding tests before deciding. The first tests were done with a ~ ∅0.5 mm fishing wire on an aluminium cylinder with a 4 mm groove (8 windings). It was difficult to get a controlled winding scheme and therefore we manufactured some grooves (like in fig. 4.5) with a width of 0.5 mm into the holder, entirely controlling the first layer of the coil including the crossing region. We chose to do the step over an angle of 45°, being exactly in the middle of the above-mentioned safe range (sec. 4.2.1). This enabled us to do a very controlled winding, first with fishing wire and later with ∅0.5 mm test wire with self-bonding property. The final result is presented in figure 4.6.

To manufacture the grooves it was necessary to divide the holder into two parts, the one

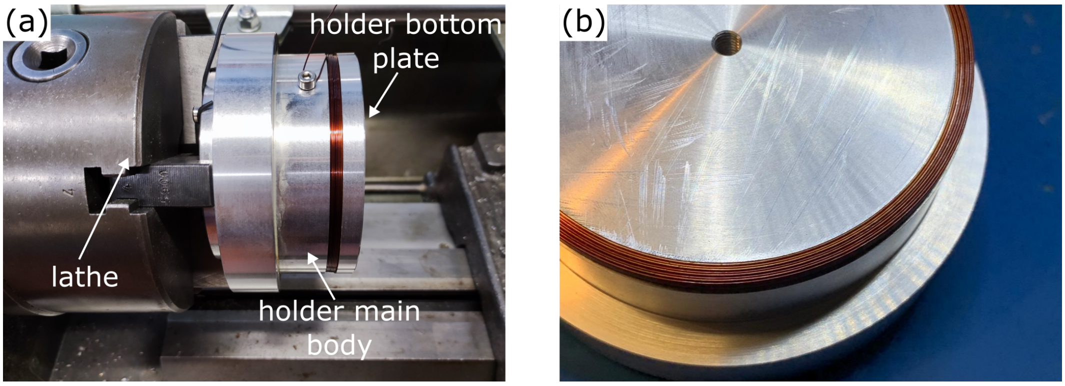

Fig. 4.6. Test coil on aluminium holder: (a) in lathe after winding, (b) close-up of the coil after baking and removing the bottom plate

seen in figure 4.6 (b), in which the grooves were cut and one bottom plate screwed on it for winding (a).

After the winding process, the coil was baked and afterwards, the bottom plate was removed, which was not possible without a bit of force, so we decided to place a layer of Kapton foil between the holder and the support plate for the final coil (see sec. 4.2.3).

4.2.3 Coil winding

For the winding process, the coil holder was prepared as seen in figure 4.7 (a), with two supporting plates made out of copper. First, the single winding of the SF-coil was laid into its groove (see fig. 4.8) and threaded through the corresponding slots in the PEEK slit filling part. Afterwards, the two supporting plates for winding are mounted from the top and bottom. In between, there were several layers of Kapton foil with a thickness of 75 µm each. One separating the coil and the respective supporting plate and two additional layers at each coil to increase the total winding width (corresponding to h_{HH} and h_{AHH}, fig. 4.1 (a)) by 150 µm. This was needed as it was not possible to perfectly fit 8 (HH) or 16 (AHH) windings into the first layer. The last winding was very slightly pressed radially outwards (less than half a wire width, but visible with eye), which ultimately led to an uncontrolled winding. The two additional Kapton foils with an outer diameter of r_{in} (fig. 4.1 (a)) fully solved this issue.

The winding process started with the AHH-coil. The wire was threaded through the corresponding slit in the PEEK part and fixed on the top plate by clamping it with a screw, after protecting the wire with a shrinking tube. For the winding, the coil holder was clamped into a lathe and the wire bobbin was placed below on a pin in a box (see fig. 4.7 (c)). The wire was then guided, wearing leather gloves, while another person manually turned the lathe, which had a counter to keep track of the number of windings. The wire was always held not exactly orthogonal to the winding direction, but under a slight angle, e.g. when a layer was wound from left to right (cf. fig. 4.7 (c)), the wire was always held a little bit left from its position at the coil. At some points, the positioning of some windings was corrected either by hand or by using a small Teflon block (to not scratch the wire). As the maximum tension on the wire was given by 1370 cN (see app. A.1), it was always wound with a moderate to low tension by feeling. After finishing the winding process the outgoing wire then was again protected via a shrinking tube, wound around an, after the winding process mounted, bracket and fixed by another screw in the top plate (cf fig. 4.7 (b)). This support was needed just for the baking process, as afterwards the coil is inherently stable. The procedure for the HH-coil was the same.

During the whole winding process, it was very regularly checked if there was an electrical contact between the coil holder and the wire, using a multimeter. Being very cautious about all sharp tools and edges, which might touch the wire, e.g. during winding at the beginning or end of each layer, turned out to be crucial, as it is very easy to damage the wire's insulation and subsequently create a short between the wire and the holder.

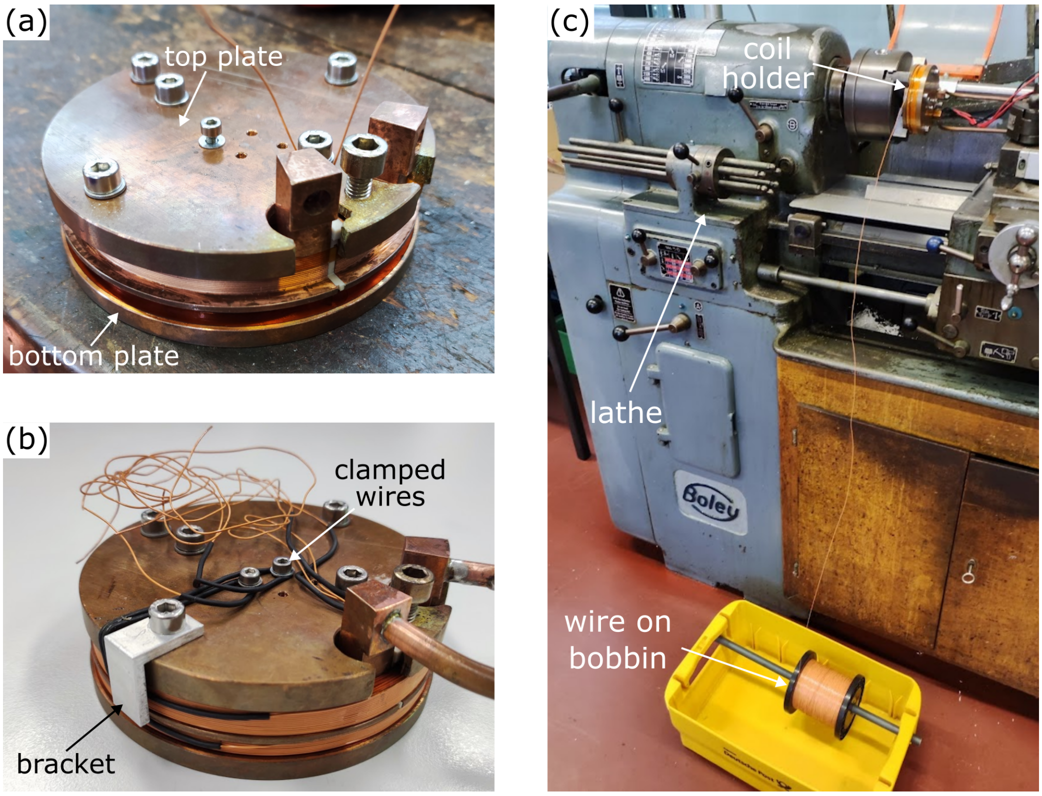

Fig. 4.7. Coil holder winding process: (a)-(b) Final coil holder with supporting plates (a) and fully wound (b), (c) winding setup on the lathe (note: Picture (b) and (c) were taken later for illustration and not directly after the winding process. The tubes seen in (b) and (c) and the electrical connections in (c) were not present at this point)

4.3 Coil Baking

After winding the coils, the holder was prepared as seen in figure 4.7 (b) (Note that the water-cooling tubes were not soldered in at this point, but after the baking process). Three thermocouples were attached to it with Kapton tape, one directly to each coil and one to the top plate. According to the datasheet of the self-bonding polyamide layer (Solabond FSP18 bonding layer, see app. A.1), the optimum baking temperature is 150 °C to 170 °C. This means once the whole coil reached a temperature of 150 °C, it stays in its shape after cooling down. We noticed during the winding tests (sec. 4.2.2), that it takes very long until the coil has its temperature if it is just put into the oven. Therefore a very big (compared to the holder) aluminium plate was put into the oven and brought to a temperature of 165 °C and the holder then was placed on this plate. The temperature of the holder was constantly monitored during the baking process via the three attached thermocouples. We waited until the temperature of the top plate reached 155 °C, to be sure, that the whole structure was at least heated up to 150 °C. The temperature readings of the thermocouples attached to the coils showed a temperature of around 158 °C to 161 °C. This process took around 10 min to 15 min.
After getting the holder out of the oven, we checked again if there was a short between one of the coils and the holder (see sec. 4.4).

4.4 Manufacturing Issues

4.4.1 Electrical-short after baking

For the first coil holder (No. 1) we wound, the two supporting plates (cf. 4.1 (b)) were made out of aluminium. Directly after baking the coil we measured a short between the upper (AHH) coil and the holder, which was not measurable before baking and disappeared after the temperature of the holder had fallen below ∼100 °C. We suspect, that this issue appeared due to the different thermal expansions of aluminium and copper. The relative linear thermal expansions for copper and aluminium are [46]

$$\alpha_{\mathrm{t,Cu}} = 17 \times 10^{-6}\,\mathrm{K}^{-1} \quad \text{and} \quad \alpha_{\mathrm{t,Al}} = 23 \times 10^{-6}\,\mathrm{K}^{-1},$$

meaning that aluminium expands more than copper. As the upper supporting plate is directly screwed into the holder (see fig. 4.7) and the lower plate is just clamped with screws against the upper plate, it seems plausible that the top aluminium plate presses the holder (which has a slit and is therefore not stable) radially outwards, which possibly leads to a cutting of the grooves through the insulation of the wire, generating an electrical contact. When the holder cools down it shrinks to its original size and the short is gone. This explanation is additionally supported by a very similar problem we faced for our rectangular coils [17]. They were wound on an aluminium frame with grooves and for all of them, we noticed a short between the coil and the holder, which was gone below a certain temperature. Here the problem was solved by just removing the whole frame except for some pieces for mounting.

For the round coils, we solved this problem by manufacturing a new set of supporting plates made of copper, which worked very well for the second and third coil we wound. For the fourth and last coil, we again measured a short after baking, which did not disappear after cooling down. Fortunately, it was possible to unwind the coil even after the baking procedure and we rewound it being extra careful and using less tension during winding. We cannot safely attribute the problem to this, but my personal guess is that the coil was wound with too much tension on the wire before. Note that using less tension makes it more difficult to obtain a perfect self-guided winding and one needs to manually correct for this more often. Either we just had more luck this time or this precaution solved the problem, but finally, we did not measure a short after baking anymore.

4.4.2 Error in groove manufacturing

For the last two holders, there was an issue in the manufacturing process of the grooves. Due to an unknown error, the outer diameter of the coil holder was slightly smaller in the lower half of the HH-coil, resulting in non-existent grooves in this region, as seen in figure 4.8.

Finally, it turned out, that it was still possible to get a well-controlled winding, but one needed to interfere a lot more during the winding process, e.g. manually correct the wire positions with a small Teflon block. The final winding ordering was slightly worse than for the holders with all grooves but still acceptable. Still, I think it was crucial to have the first windings controlled by the grooves as this enabled the possibility to just press the following ones against these.

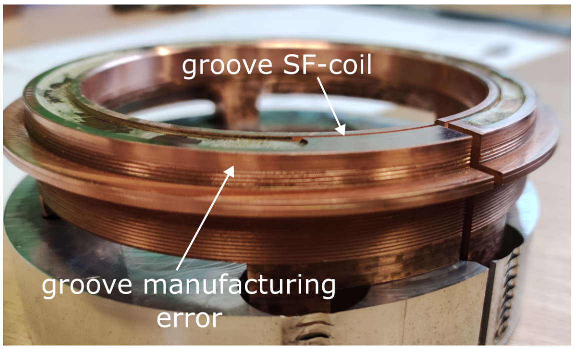

Fig. 4.8. Groove manufacturing error

4.4.3 Leakage in Bottom Plate of Holders

Unfortunately, we noticed that we have a leak in the bottom plate of holder No. 3 and 4 (see next section 4.5 for an overview of manufactured holders). For holder No. 3, which was soldered the leak appears at one connection point between the bottom plate (cf. fig. 4.1) and the holder itself (see fig. 4.9 (b)). The groove for the SF-coil was manufactured after soldering and apparently the gap between the holder and bottom plate was not filled with solder and as the material on top was removed for the groove the leak appeared.
Holder No. 4, which was welded not soldered, has two leaks, one at exactly the same position (see fig. 4.9 (e)), which seems to be a weak point, and one somewhere directly in the welded material (see fig. 4.9 (d). It can hardly be seen in the figure, but when connected to water lines, water leaking out at this point can clearly be noticed.

We had an extensive discussion about how to go on with this issue. Our focus was on first having one working pair of coil holders. Holder No. 1 and 2 have no leak, but as discussed above (sec. 4.4.1), for Holder 1 we measured a short after baking and the winding is a bit uncontrolled as we improved the winding process after the first holder (see sec. 4.2.3). Therefore, we decided that we will rewind this coil. Furthermore, we were concerned that a leak develops over time at exactly the same position at holders No. 3 and 4, which seems to be a weak spot. Thus, we will further reinforce the bottom plate of holder No. 1 and 2 probably with an epoxy filling, the exact material is still point of ongoing discussions.
For holder No. 3 and 4, we had an intensive discussion about different fixing methods. We decided against glueing, as due to experience from other groups leaks fixed like this have a high probability to leak again after a timescale of several years. As such a leak has the potential of seriously damaging our objective lens and inverted viewport, accessing the holder at a later point furthermore involves a huge effort of disassembling the setup, and we do not want to take this risk. Therefore, we would like to fix this leak through another soldering process. Which process this will be is also still object of ongoing discussions. The main point we are concerned about is damaging the coil during this process, which is very likely. So it is not clear yet, if we directly unwind the coil, do the soldering and wind it again or if we just try to do the soldering and see if we damage the coil and rewind it if needed.

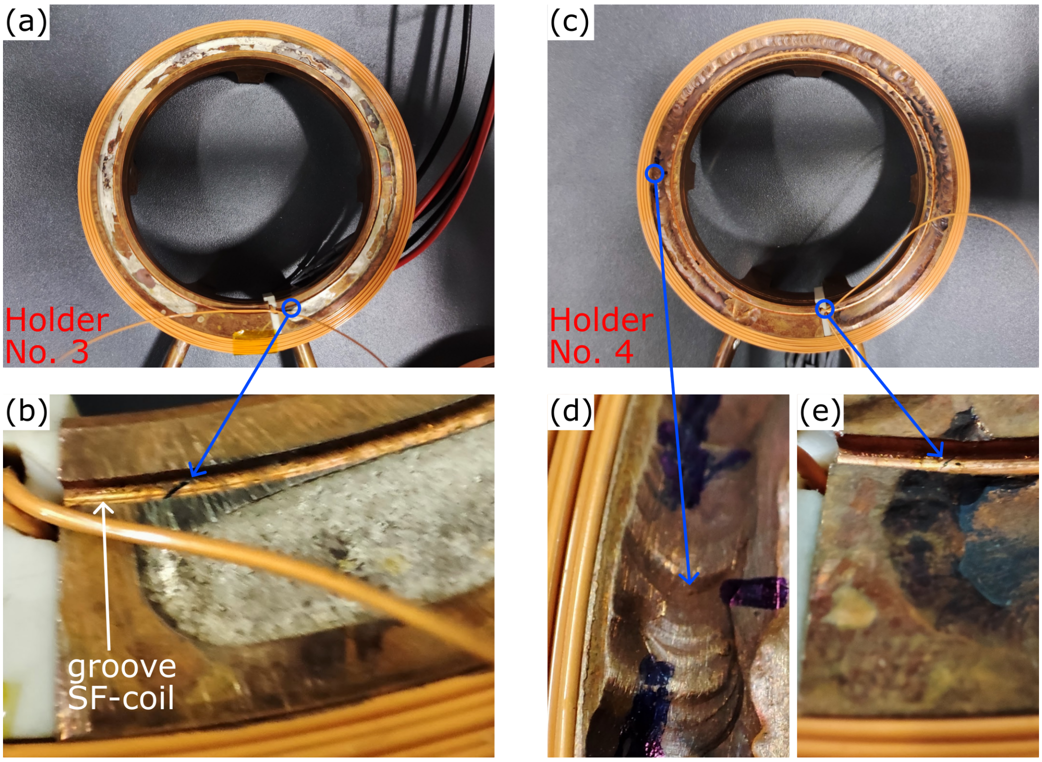

Fig. 4.9. Leak in coil holders No. 3 and 4: (a) Overview of holder No. 3 and close up of leak at bottom plate-holder connection (b), (c) overview of holder No. 4 and close up of leak in welding in (d) (small hole visible under close inspection) and at the bottom plate-holder connection in (e)

4.5 Summary and Final Coil Setup

Below we summarize the properties of each of the four holders manufactured. **Holder No. 1**

The holder is watertight, but the winding is a bit uncontrolled and we measured a short directly after baking for the AHH-coil (see sec. 4.4.1). The uncontrolled winding causes a slightly worse cooling behaviour. With turned on water cooling with a current of 5 A (HH) and 4 A (AHH) the coils have a temperature of $\approx$10 °C higher than for the coils of Holder No. 2 (cf. 5.1).

We will rewind both coils of the holder and reinforce the bottom plate, as we fear that it might have the same weak spot in terms of leakage as holder No. 3 and 4.

Holder No. 2

The holder is watertight and manufactured as planned. As for Holder No. 1, we plan to reinforce the bottom plate.

Holder No. 3 & 4

The winding is well structured, but there is water leakage at the bottom plate (see fig. 4.9). We are still in the process of discussing how to proceed with these holders, but probably we will fix these leaks by soldering and maybe rewind the coils (see sec. 4.4.3).

Final coil setup

The final wound coil is presented in figure 4.10 and the full final setup of the coils around a 3D-printed model of our main chamber and inverted viewports can be seen in figure 4.11.

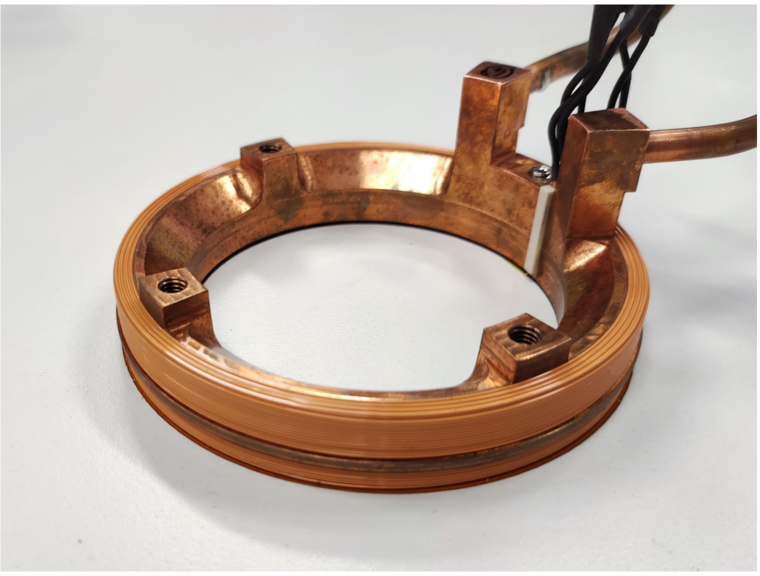

Fig. 4.10. Final wound coil

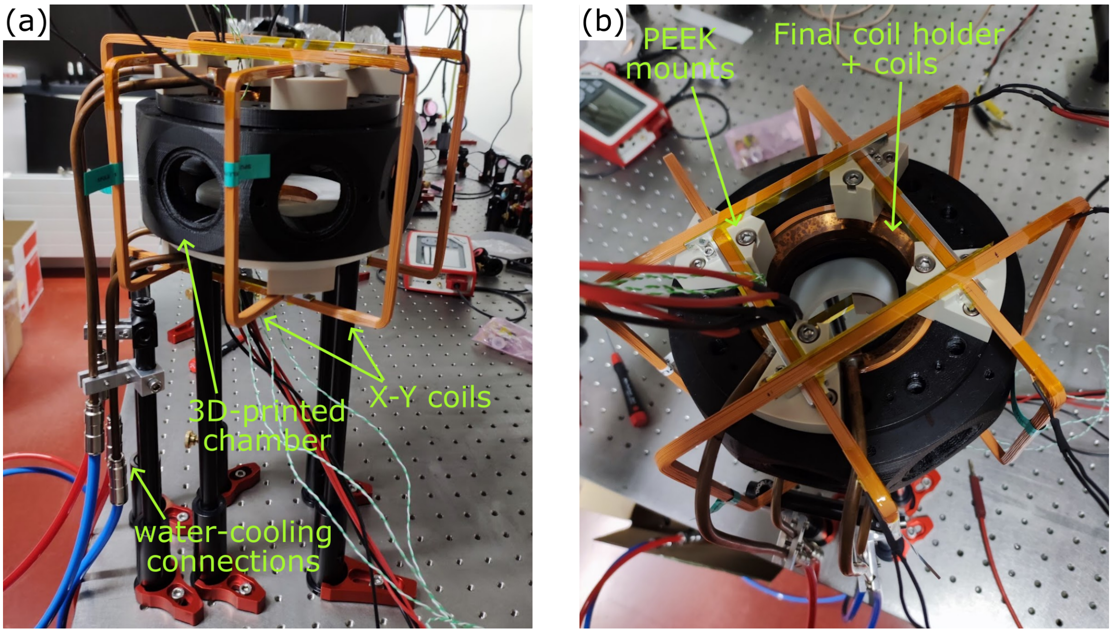

Fig. 4.11. Full coil setup around 3d printed or main chamber

5 Characterization of Magnetic Coils

In this chapter, we present the various performance test that we performed on the coils after their manufacturing. That includes temperature stress test, time and frequency current response, and magnetic field measurements. For all following tests, the coils were mounted together with the compensation cage in the 3D-printed setup of our main chamber, as shown in figure 4.11. This was the most realistic scenario we could simulate without having the possibility to use the final main chamber and viewports, as they were in use and the coils needed to be tested before finally mounting them into the setup.

5.1 Heating Characteristics

A very important measurement is the heating characteristic of the coils, as they dictate the conditions of safe operations of the coils without overheating. The first tests were done with a continuous current running through either the HH- or the AHH-coil of one of the four manufactured holders, each with and without water cooling. The temperatures were measured via a thermocouple attached to the outside of the coil (radially in the gap between the inverted viewport and coils) close to the electrical connections via Kapton tape. The data is depicted in figure 5.1. The temperature curves were taken up to a limit of 60 °C (with exception of one data point for the HH-coil), as we agreed on this as a safe value to not damage the coils or the printed plastic chamber and anyway as discussed in section 3.2.3 we would not like to go above 50 °C in the final experimental setup. The curves seem to have a parabola shape, which makes sense as the power is proportional to I^2. The temperature of the holder without current is slightly higher than room temperature, which might indicate that we didn't wait long enough before the measurement to take this data point.

In table 5.1 the maximum values of figure 5.1 with a temperature below 60 °C are summarized. The calculation of the power relies on calculated temperature-dependent resistance values, derived by plugging in (3.16) into (3.14) for the final coil values (cf. tab. 3.4). We relied on the calculated resistance values, as we are interested in the coil's resistance without supply lines. The slightly higher measured value (see section 5.2) is probably due to the supply lines and indicates that the calculated value is a good choice. The power values for the AHH-coil are slightly higher than that for the HH-coil, which makes sense as the AHH-coil is bigger and has, therefore, a larger exposed area to the water cooling and is furthermore directly exposed on one side, different to the HH-coil, which is the closest to the bottom plate of the inverted viewport (cf. fig. 3.7).

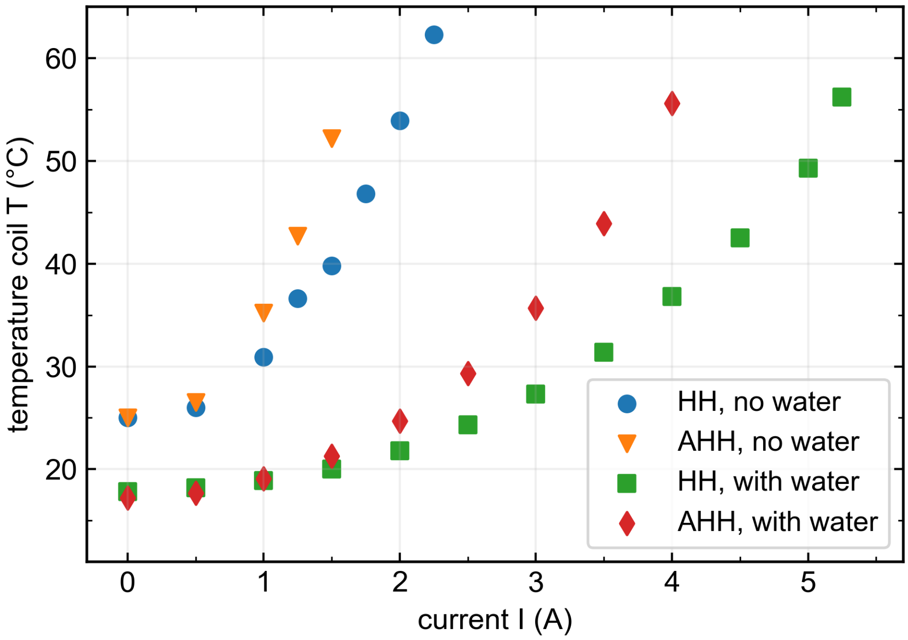

Fig. 5.1. Heating characteristics of HH- and AHH-coil for continuous current, with and without water cooling, the room temperature is 22.0(5) °C and the cooling water temperature 17.0(5) °C

The situation without water-cooling is slightly better than simulated, a temperature of ≈ 43 °C for the HH-coil is reached for ≈ 1.6 A (see fig. 5.1, corresponding to a power of 3.9 W, different from the simulated value of 1.3 W (cf. sec. 3.2.3, fig. 3.3). This might be explained by our choice of a too low chosen value for the convective heat transfer coefficient in the simulation in chapter 3.
With water cooling the power where 50 °C is reached is around 50 W for the HH-coil. Therefore, the coil performs better than in the simulation with water cooling and for a standard thermal conductivity of the wire's insulation (cf. sec. 3.2.3, fig. 3.4 (b)), where 48 °C are reached at 30 W, but it performs worse than the situation in fig. 3.5 (b) with an arbitrarily increased thermal conductivity. As already discussed in section 3.2.3 the discrepancy was expected and overall the order of magnitude of the simulation is justified. Furthermore, it indicates that the increased thermal conductivity of the wire in fact improves the thermal behaviour of the coil, but as we have no comparison measurement using a different wire in the same configuration, we can not clearly conclude that.

Additionally, images with an infrared (IR) camera were taken to check if there are no hotter spots at the holder than measured in figure 5.1. An image with and without water cooling is presented in figure 5.2. In both cases, there is no point at the coil with a temperature exceeding the measured temperature with the thermocouple. Furthermore, it can be noticed, that the holder has a constant temperature of around 17 °C to 19 °C for all measurements with water cooling and does thus not heat up (see fig. 5.2).

	unit	HH		AHH	
		no water	water	no water	water
Temperature T	°C	53.9	56.2	52.2	55.6
Current I	A	2	5.25	1.5	4
Power P	W	7.1	49.4	8.2	58.7
Field / Gradient		21.6 G	56.7 G	7.8 G/cm	20.8 G/cm

Table 5.1: Summary of maximum values for currents with a corresponding temperature below 60 °C, the corresponding power per coil and the maximum field/gradient, which can be achieved.

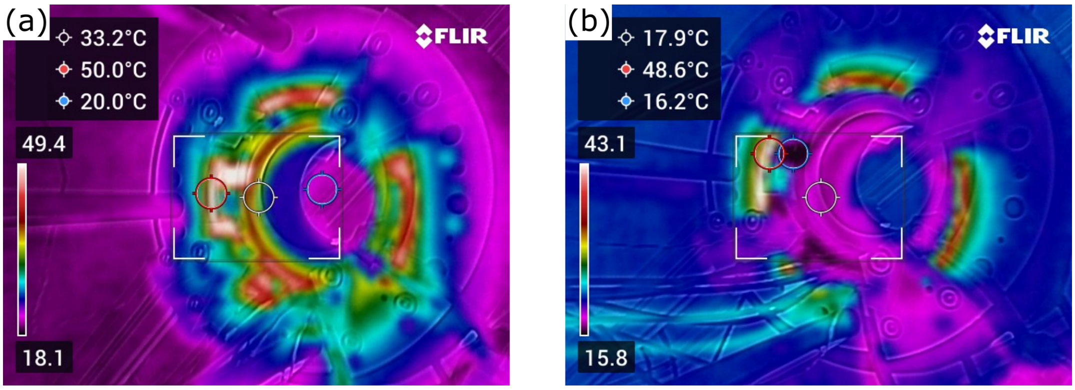

Fig. 5.2. IR-images of AHH-coil with- and without water-cooling: (a) No water cooling with current of 1.5 A, temperature at outer coil surface measured with thermocouple is 52.8 °C, (b) Water cooling with current of 4 A, temperature at outer coil surface measured with thermocouple is 55.6 °C

Combined use of both coils

To estimate how the coils behave, when they are used at the same time, two measurements respectively with and without water-cooling were performed and compared to the characteristics shown in figure 5.1.

Without water cooling the total power of the two coils directly adds up and the current which can be sent through the coils while keeping the temperature below 60 °C is significantly lowered. A current of 1 A was sent through both of the coils, leading to a total power of 5.2 W, the coils reached a temperature of 44.2 °C and 44.3 °C. For the individual operation a similar temperature of 46.8 °C was reached by the HH-coil at 1.25 A (5.3 W) and a temperature of 42.7 °C was reached by the AHH-coil at 1.25 A (5.5 W).

For the case with water cooling, both coils behave nearly the same as in individual use. Currents of 4 A and 3 A were sent through the HH- and AHH-coils respectively (to have a similar power in both coils). This led to a temperature of 38.1 °C (36.8 °C in individual use) in the HH-coil and 36.1 °C (35.7 °C in individual use) in the AHH-coil.

Simulating duty cycle

As the coils will most of the time not run continuously in the experiment, but with a certain duty cycle, an additional measurement was performed to check if the important parameter one needs to consider for the heating is actually the mean deposited power, as one would expect. For this the coils were switched on and off at intervals of 500 ms.
Without water cooling, we tested with the HH-coil. It reaches a temperature of 39.8 °C at a continuous current of 1.5 A. The same mean power with the duty cycle described above is reached at a continuously switched current with an amplitude of 2.12 A. With this procedure, the coil reached the exact same temperature of 39.8 °C. The test with water cooling was performed the AHH-coil (to reach a higher temperature at rather low currents). The AHH-coil reached a temperature of 35.7 °C at 3 A, corresponding to a current amplitude of 4.24 A with described duty cycle. The reached temperature here was 34.8 °C.
Therefore, we can conclude that indeed the mean power can be considered to dictate the coil's heating. Of course, this has its limitation, at some point for really high currents, even for a very short time, the coil will heat very quickly and one needs to carefully monitor the temperature if one plans to implement such a cycle.

5.2 Time Response of Coils

5.2.1 Switching times with PI-control

As discussed in section 2.4 it is of great importance to the experiment, to be able to fully switch on/off the fields/gradients fast. Here we test the time response characteristics of the coils in the test setup of fig. 4.11 (that is to say is their final configuration yet without the metallic environment of the final chamber) and through the behaviour of the current flowing through one pair of coils.
These measurements were done with our home-built power supply described in section 3.4. A step input voltage corresponding to a final current of 1 A is given as set-value for the power supply and the resulting current in the coils is measured via the amplified voltage drop over the measurement resistor used also for the feedback loop of the supply. In figure 5.3 the current response of the HH- and AHH-coils in series can be seen. As test current we chose 1 A, as this for both pairs of coils roughly matches the required field/gradient values (see sec. 3.2.4). The final current value for the HH-coils is reached somewhere between 100 µs to 150 µs, for the AHH-coils at approximately 250 µs. The turn-off times are nearly symmetric to the turn-on times, as expected, as the limiting factor in the switching time with PI-control is the maximum voltage that can be delivered by the power supply of $\sim \pm 30\,\mathrm{V}$. Our power supply is bipolar and has a nearly symmetric maximum and minimum voltage. The AHH-coils turn off time is roughly 50 µs faster than the turn-on. This can be explained by the following effect: When the AHH-coils run at 1 A the power supply needs to deliver roughly 6.5 W, when now during switch off the PI regulates the supply's voltage to its minimum of $\sim -28\,\mathrm{V}$, the difference to the current voltage is larger than for turn on and the switching time is faster. The HH-coils have significantly smaller resistance this effect is not visible.

We therefore achieve the requirement of switching significantly below 1 ms, as discussed in section 2.4. Finally, the time scale of the magnetic field will thereby not be limited by

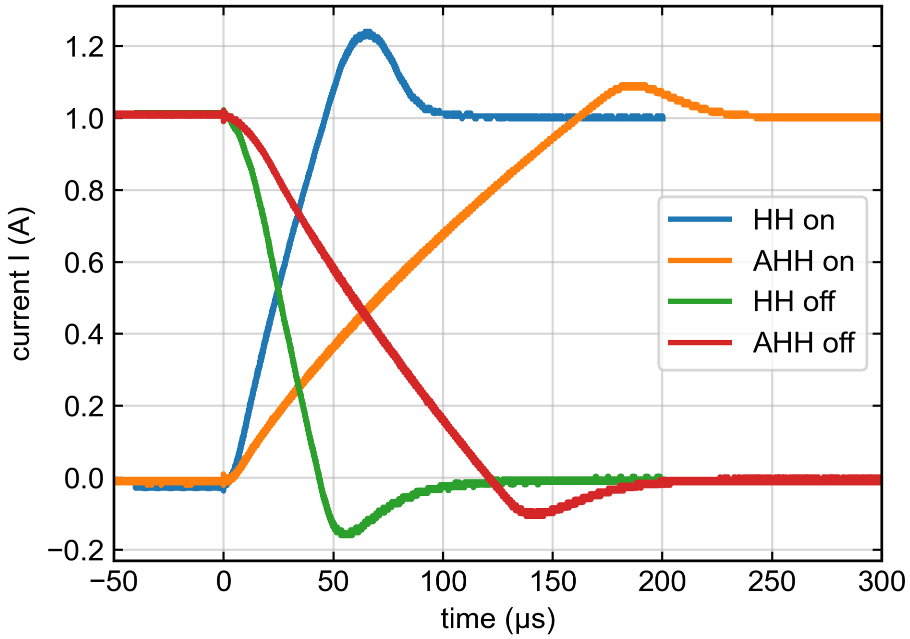

Fig. 5.3. Full turn on/off of HH- and AHH-coil in series with PI-control to/from 1 A, corresponding to a magnetic field/ field gradient of 10.8 G/ 5.2 G cm^{-1} respectively. At t=0 a step input corresponding to a set current of 1 A is fed to the power supply

the coils themself, but probably by eddy currents in the steel chamber. Therefore, we are also not concerned about the significant overshoot of the current in the coils seen in figure 5.3, as this will at most improve the time scale of the magnetic field.

5.2.2 Switching times without PI-control

To characterize the coils themselves, it is also very interesting to evaluate their current time response $I(t)$ as answer to a step input voltage U_0. As already discussed in section 3.2.2 the time response of a coil is given by:

$$I(t) = I_0 \left(1 - e^{-\tau\, t}\right), \tag{5.1}$$

with $I_0 = U_0/R$ and $\tau = R/L$ in dependence on the resistance R and inductance L of the coils configuration. We wired the HH- and AHH-coils again in series and set U_0 (the output voltage of our home-built power supply), such that the final current $I_0 = 1\,\mathrm{A}$. The result of these time measurements is shown in figure 5.4. As expected the turn-on and off curves are symmetric. The turn-on behaviour of both coil configurations was fitted with (5.1).

Additionally, the resistance of the final coil configurations was measured and via the fitted value of τ the inductance of the coil pairs was calculated. The results are summarized in table 5.2. The resistance was measured by applying a test-current of 1 A via an R&S Hmp4040 power supply (having a highly accurate readback of current and voltage) and measuring the voltage. It was connected in four-wire voltage measurement mode to compensate for the supply lines directly connected to the power supply. Therefore, R_{exp} is

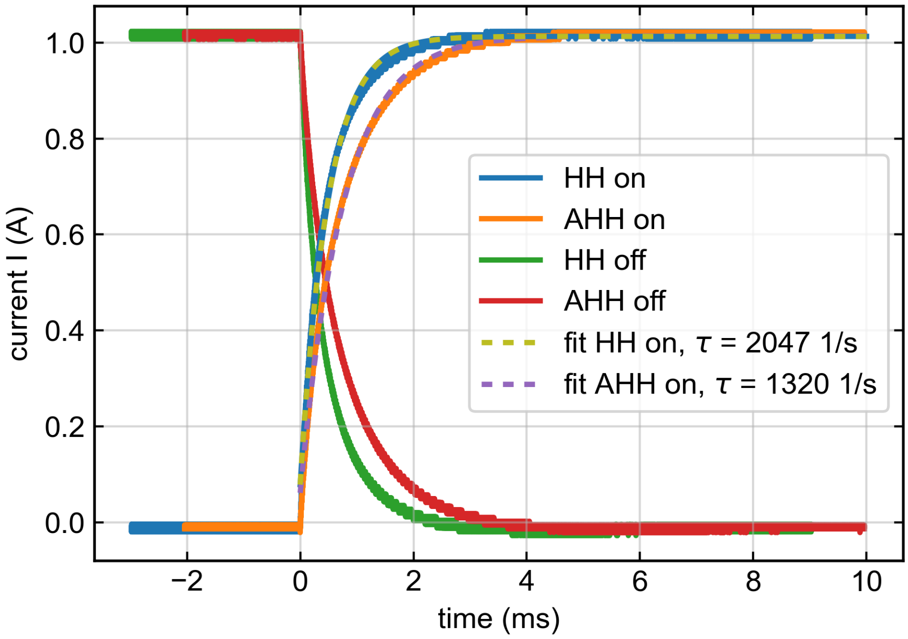

Fig. 5.4. Full turn on/off of HH- and AHH-coils in series without PI-control: Turn on curves show current response of coil-configurations to a step input voltage at $t = 0$, chosen such that $I_0 = 1\,\mathrm{A}$. Turn-off curves show current response when this voltage is switched to 0 at $t = 0$. Turn-on curves are fitted via (5.1), the fitting error of τ is negligibly small.

the resistance of both coils in series with their soldered connection wires and one interconnection ($\approx 5\,\mathrm{m}$ in total). Both coils had a temperature in the range $T = 22 \pm 1\,°\mathrm{C}$, which slightly varied during the measurements. Therefore an additional error of 0.5 % (expected change in resistance for a temperature change of 1 °C according to (3.16)) was added to the measured voltage additionally to the readback accuracy of the power supply. Due to the additional wiring which adds up to the intrinsic resistance of the coils, it is not surprising that the experimental value of the resistance is slightly higher than the calculated one.
The experimental value of the inductance of the HH-coil pair is in good agreement with the previously calculated one (cf. tab. 3.5). The of the AHH-coil is lower than the calculated inductance value, which means that the coil switching time is faster, as one would expect from the calculated inductance and resistance. This makes sense, as the coils are wired in a quadrupole configuration and therefore the induced current from one coil in the other is effectively decreasing switching time in the latter and vice versa.

	R_{exp} (Ω)	R_{cal} (Ω)	τ_{exp} (s^{-1})	L_{exp} (mH)	L_{cal} (mH)
HH	3.320(19)	3.16	2047	1.622(9)	1.61
AHH	6.64(4)	6.49	1320	5.030(3)	5.69

Table 5.2: Comparison of experimental and calculated coil parameters: Resistance R_{exp} of coil setup in series, τ_{exp} extracted from fit in fig. 5.4 (error is negligible) and L_{exp} calculated via $L_{\mathrm{exp}} = R_{\mathrm{exp}}/\tau_{\mathrm{exp}}$. The calculated values are taken from table 3.5

5.2.3 Frequency response without PI-control

Another important coil characteristic is its frequency response. When considering a sine-wave-like AC signal of frequency f is applied to a coil, one has to consider its complex $\tilde{Z}$ impedance, which is given by:

$$\tilde{Z} = R + i\omega L \tag{5.2}$$

with the circular frequency $\omega = 2\pi f$. The current $\tilde{I}(t)$ flowing through this impedance upon applying a voltage $\tilde{U}(t)$ and the corresponding amplitudes can then be calculated via Ohm's law

$$\tilde{I}(t) = \frac{\tilde{U}(t)}{Z(t)} \quad \Rightarrow \quad |\tilde{I}(t)| = \frac{|\tilde{U}(t)|}{\sqrt{R^2 + \omega^2 L^2}} = \frac{|\tilde{U}(t)|}{\sqrt{\tau^2 + \omega^2}}. \tag{5.3}$$

For the frequency response, a sine-wave-like voltage signal with a peak-peak voltage chosen such that the peak-peak current in the coils corresponds to 300 mA for low frequencies is applied to the coils and the current amplitude is measured with the measurement resistor included in our home-built power supply. The results of the measurements are shown in figure 5.5. Equation (5.3) is fitted to the data and the time constant τ is extracted. The fit describes the data pretty good for frequencies up to $\approx 1\,\mathrm{kHz}$, for larger frequencies the coils show a lower amplitude damping than expected. This is reflected in the large error on the time constant. The time constant extracted via fitting the time response (cf. fig. 5.4) seems to be the more reliable value and still lies in a 2σ interval of the τ extracted from the frequency response.
Furthermore, the 3dB cut-off frequencies for both coil-configurations are extracted from the fit (see fig. 5.5). Note that the frequency response in the experiment will be finally limited by the power supply and not the intrinsic frequency response of the coils described here as already seen from the time response measurements of 5.2.1 and 5.2.2.

5.3 Magnetic Field Measurements

To fully characterize the magnetic field, especially to confirm the claimed field quality, one needs a high-precision magnetic field sensor. We ordered one, but unfortunately, it didn't arrive on time to use it for the measurements in this thesis. Thanks to the HQA[1] group, who kindly lend us their sensor, we could still do some characterization. The main limiting factor was the minimum step size of the sensor of $\approx$1.6 G. To minimize this error source, for each data point an average of five measurements were taken a. As a systematic error of each measurement, the step size was chosen and quadratically summed with the statistical deviations of the set of five data points. Before measuring the field in the final setup, a calibration of the sensor was performed following a procedure that was originally designed by Christian Gölzhäuser to characterise the 2D-mot magnetic field configuration [47]. One axis of the sensor (y-axis of the sensor) was calibrated by placing the sensor in the centre of one HH-coil and the magnetic field in along the symmetry ($z-$axis) was measured for a current range of $-5\,\mathrm{A}$ to $5\,\mathrm{A}$ in $0.5\,\mathrm{A}$ steps. A linear fit was performed and the measurement was compared to the expected calculated value. The resulting magnetic field B_m for a sensor output b_sen reads:

$$B_\mathrm{m} = (b_\mathrm{sen}(\mathrm{G}) - 11.2(4)\,\mathrm{G})\frac{7.93\,\mathrm{G/A}}{16.08(15)\,\mathrm{G/A}}. \tag{5.4}$$

---

[1] Heidelberg Quantum Architecture

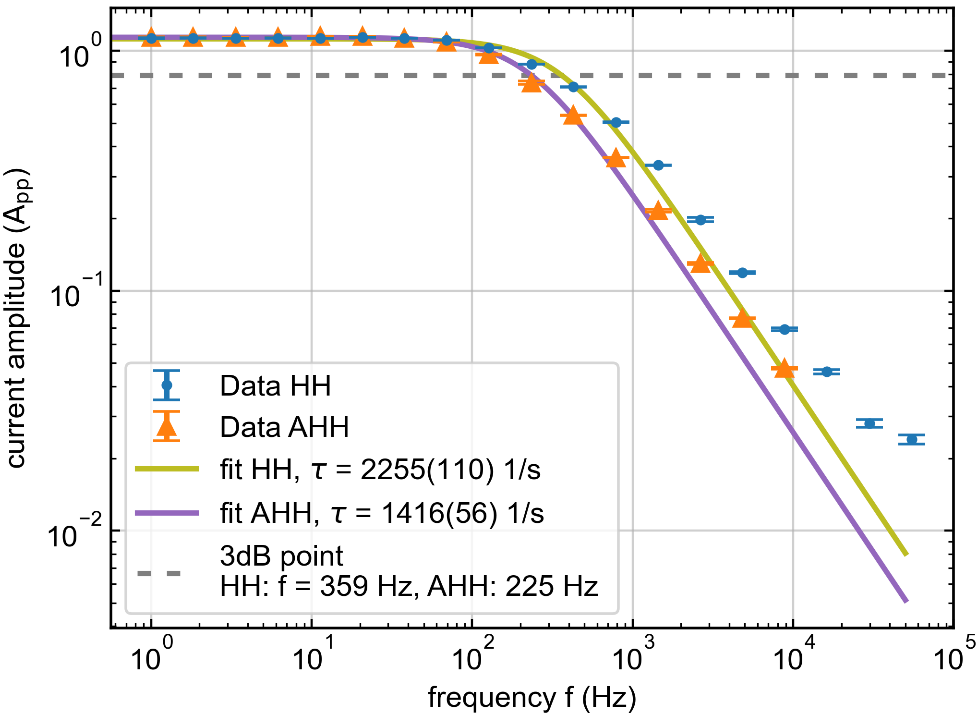

Fig. 5.5. Frequency response measurement of HH- and AHH-coils in series without PI-control: A sine-wave like voltage signal with a peak-peak voltage chosen such that the peak-peak current in the coils correspond to 300 mA for low frequencies is applied to the coils and the current amplitude is measured with the measurement resistor included in our home-built power supply (see sec. 3.4). The data are fitted with (5.3) and the 3dB cut-off frequency is noted.

This result relies on the calculated field current conversion factor for the single HH-coil is $7.93\,\mathrm{G\,A^{-1}}$. Of course, it would be better to calibrate the sensor with an independent measure, but this was not possible, as we had no other source for a reliable magnetic field strength at hand.

For the HH-coils the z-component of the magnetic field was measured at the centre of the chamber for different currents (see fig. 5.6) to verify the calculated magnetic field to current-conversion factor. As seen in table 5.3 the measured and calculated value are in good agreement with each other.

	unit	Field/gradient to current conversion factor	
		experiment	calculated
HH	G/A	10.68(19)	10.75
AHH	G/(cm A)	5.03(17)	5.17

Table 5.3: Measured and calculated magnetic field/gradient conversion factors for HH/AHH-coils, extracted from fits in fig. 5.6 and 5.7

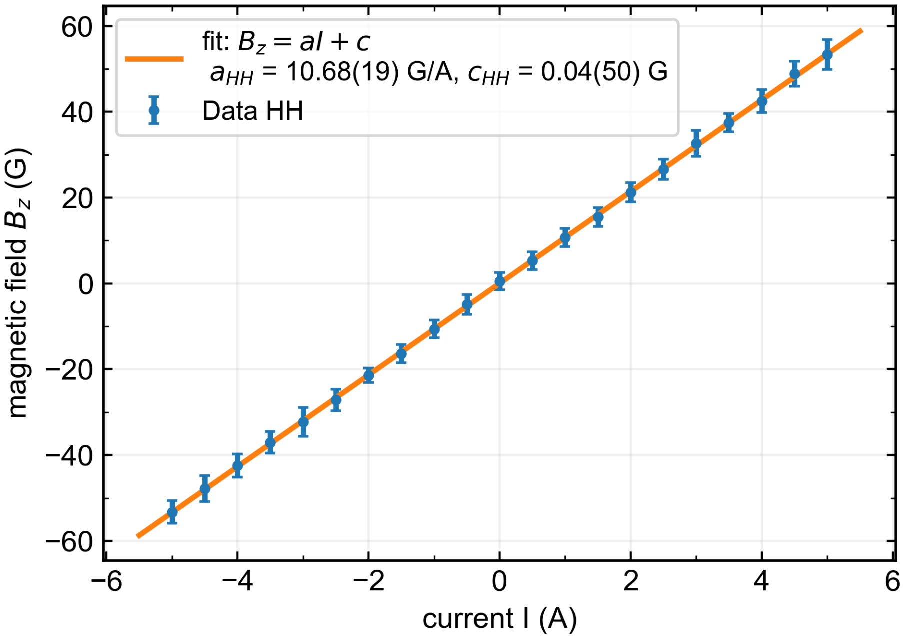

Fig. 5.6. Magnetic field measurement HH-coils: Magnetic field sensor is placed in center of 3D-printed main chamber and the $z-$component of the magnetic field is measured vs. the current

In figure 5.7 a similar measurement is presented to measure the gradient of the AHH-coil. It was only done for one current of $I = 4\,\mathrm{A}$, but for different positions along the $z-$axis. Also here the measured current-to-field gradient conversion factor is in good agreement with the calculated one.

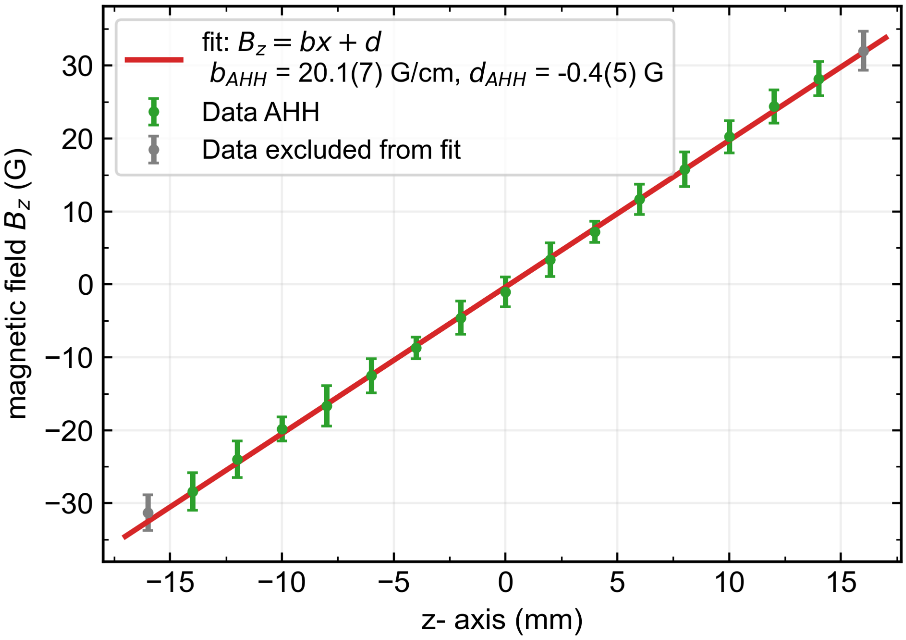

Fig. 5.7. Magnetic field gradient measurement AHH-coils: Magnetic field sensor is moved with a linear stage along the $z-$axis of the main chamber and the $z-$component of the magnetic field is measured for a current of $I = 4\,\mathrm{A}$, calculated values taken from table 3.5

6 | 3D-MOT Implementation

The optical design of our 3D-MOT input arms will be presented in this chapter. Furthermore, a set of partially optimized parameters is provided.

6.1 Optical Setup Design

For the 3D-MOT we planned for the most common configuration as described in section 2.3.1 consisting of six counter-propagating circularly polarized beams crossing in the centre of the main chamber. Two pairs enter the main chamber in the horizontal plane via the CF40 viewports and one pair is crossing the main chamber along the z-axis through the reentrant viewports as depicted in figure 2.5.

To get an estimate about the optimum parameters, being detuning, beam width and power of the laser beams, as well as the magnetic field gradient strength, a Monte Carlo simulation of the MOT loading process was carried out by Jianshun Gao [32]. As described in 2.4.1 the atoms leave the oven as a hot vapour jet, are captured in the 2D-MOT, from there transported via a push-beam through the differential pumping stage into the main chamber and finally captured in the red 3D-MOT. A representative sample of possible atom trajectories from the oven to the 3D-MOT has been simulated. A set of optimized 3D-MOT parameters obtained via the simulation is presented in table 6.1. As all parameters of 2D- and 3D-MOT, the push beam, as well as from the oven are strongly coupled and the simulation relies on several assumptions and does not account for the complexity of the system, it is not possible to find the final optimum parameters in the simulation. We should rather consider the parameters presented here as the best guess on which we oriented during the design process and serve as a starting point for the final experimental optimization. The most important parameter for the optical design is of course the beam width. Note that in the simulation the beam is cut at a diameter of ∅35 mm, as this is the clear aperture of our viewports.

To achieve the six circularly polarized beams in the experiment, the easiest way is to use three individual circularly polarized input beams, which pass the chamber, afterwards a $\lambda/4$-waveplate, are retro-reflected, such that they pass again the waveplate, which then finally swaps the polarization with respect to the incoming beam before they enter the chamber from the other site.
We decided to assemble the input beam optics as an input arm using a cage system, as this is a very flexible solution due to the possibility to easily change the constituting optical elements, but also move the whole input arm and further makes alignment easier by reducing the degrees of freedom. We decided to not include mirrors at the end of

the input arm to align the beam, as the respective 2-inch mirror mounts from Thorlabs included magnetic components, which we didn't want to have next to our main chamber. We agreed to try a fully rigid input arm and see if it is possible to align with this.

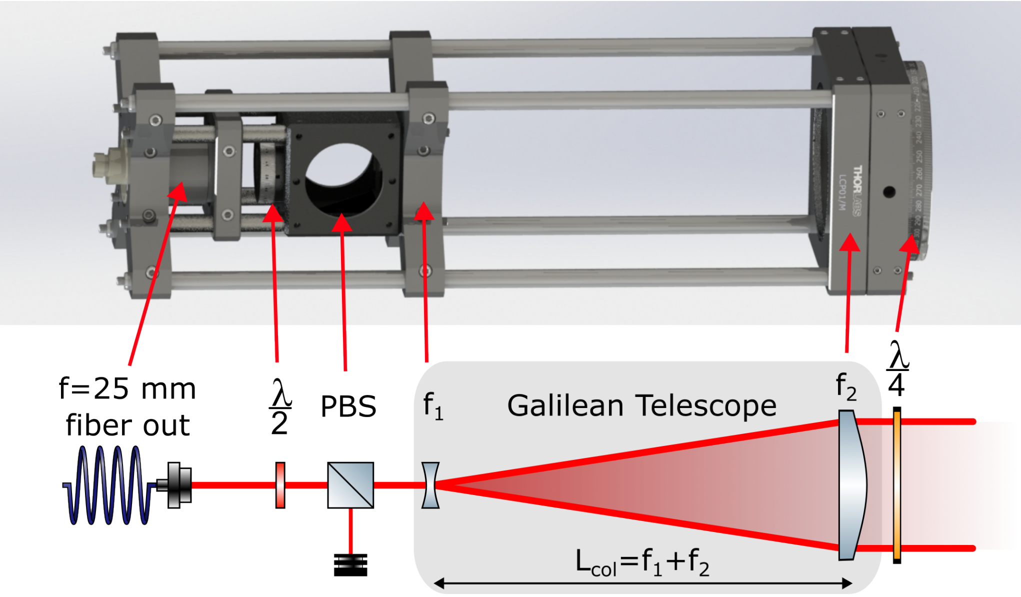

Fig. 6.1. Input arm design: The beam is outcoupled from a fibre via a fibre collimator with focal length of $f = 25\,\mathrm{mm}$, passes a $\lambda/2$-waveplate + polarizing beamsplitter (PBS) to clean the linear polarization before entering a Galilean telescope to increase it to the desired beam size and finally passes a $\lambda/4$-waveplate to achieve circular polarization.

The conceptual design as well as a 3D-model of the input arm can be seen in figure 6.1. We use a single-mode fibre from OZ Optics[1]. The effective numerical aperture, which is defined at the $1/e^2$-intensity level of the beam, is provided by the manufacturer as $NA_{\mathrm{eff}} = 0.089(10)$ at a wavelength of $633\,\mathrm{nm}$, close enough to the from us used $626\,\mathrm{nm}$ to use it as an approximation of the beam size. The beam width w (defined as half the beam diameter at the $1/e^2$-level) of a beam collimated via a lens of focal length f after a fibre output, can be easily found from the definition of the numerical aperture $NA = n\,sin(\theta)$, with n the refractive index and θ the far-field divergence angle of the beam, as

$$w = f\,NA_{\mathrm{eff}} \tag{6.1}$$

via geometric constructions and under the small angle approximation. The distance between the fibre end and the lens is in the collimated case equal to f. One needs to use the effective NA, as we are interested in the $1/e^2$-beam size. We decided on a fibre outcoupler with an intermediate focal length of $f = 25\,\mathrm{mm}$ from Schäfter + Kirchhoff[2], such that we need a telescope with intermediate magnification factor. According to (6.1) the beam radius after the outcoupler w_{fib} is

$$w_{\mathrm{fib}} = 2.23(25)\,\mathrm{mm}. \tag{6.2}$$

---

[1] fibre model: OZ Optics Ltd. PMJ-3A3A-633-4/125-3-5-1

[2] outcoupler model: Schäfter + Kirchhoff GmbH, 60FC-T-4-M25-01

Therefore the magnification factor M to achieve the beam width of the simulation $w_{\text{sim}} = 14.7\,\text{mm}$ (cf. tab. 6.1) is around:

$$M_{\text{sim}} = \frac{w_{\text{sim}}}{w_{\text{fib}}} = 6.6. \tag{6.3}$$

The magnification of a Galilean telescope as depicted in figure 6.1 can be easily obtained via geometric construction as

$$M = \frac{f_2}{f_1}. \tag{6.4}$$

We didn't fix the focal lengths of these two lenses during the design process but ordered several different lenses to obtain values around (6.3) to test the resulting beam quality.

In principle, one would like to have a collimated beam after the telescope, but in reality intensity losses at the viewports, waveplate and the mirror would result in a decreased intensity of the reflected beam passing the atom cloud in the centre of the main chamber the second time. The center intensity I_{c} of a gaussian beam, traveling along the $z-$axis, is given by [48, p. 79]:

$$I_{\text{c}}(z) = \frac{2P}{\pi w^2(z)}, \tag{6.5}$$

with P the total power of the beam. Let's assume the beam passes the atoms at z_1 the first time, then passes the viewport, the $\lambda/4$-waveplate, is reflected by the mirror, travels again through the waveplate and the viewport and passes the atoms' position the second time at z_2. The total transmission/reflection losses are reflected in the coefficient T, such that $P(z_2) = T\,P(z_1)$. We would like to achieve the same centre intensity at these two points: $I_{\text{c}}(z_1) \overset{!}{=} I_{\text{c}}(z_2)$. From (6.5) directly follows for the corresponding beam widths:

$$\frac{w(z_2)}{w(z_1)} = \sqrt{T}. \tag{6.6}$$

So we would like to have a slightly converging beam, which can be achieved by slightly increasing the length of the telescope L (see fig. 6.1) from its collimated position $L_{\text{col}} = f_1 + f_2$. The coefficient T can be easily estimated by measuring the total power of a small laser beam before and after the respective optical components.

6.2 Experimental Realization

The following discussion will focus on setting up the MOT-beams in the horizontal direction to present the concept, in the end, I will also comment on the vertical MOT-beam. The two points of interest in the horizontal direction, at which the beam crosses the atoms the first (z_1) and second (z_2) time, with respect to the last optical element of the input arm are:

$$z_1 = 30\,\text{cm and } z_2 = 90\,\text{cm}. \tag{6.7}$$

Note that z doesn't refer to the in previous chapters defined axis of the main chamber, but is the beam propagation axis. The overall measured transmission of the optics between

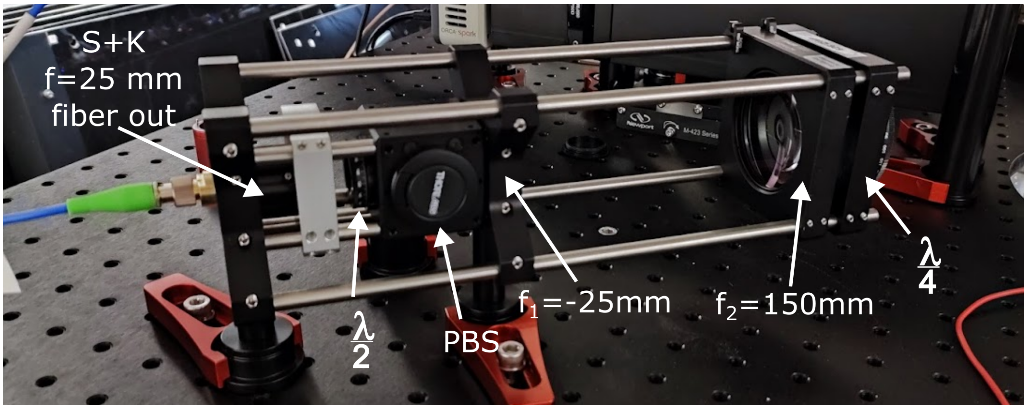

Fig. 6.2. Input arm in experiment

these two points in the horizontal plane is $T_{\text{hor}} = 0.970(4)$, as introduced in (6.6) and the corresponding wanted relation of the widths at these positions directly follows as

$$\frac{w(z_2)}{w(z_1)} = \sqrt{T_{\text{hor}}} = 0.984(2). \tag{6.8}$$

The whole input arm was mounted according to the design seen in figure 6.1 and is shown in figure 6.2. The first lens setup, with corresponding magnification according to (6.4) for the telescope, we tested was

$$\text{Configuration 1}: \; f_1 = -15\,\text{mm}, \; f_2 = 100\,\text{mm} \;\Rightarrow\; M_{\text{c1}} = 6.67\,. \tag{6.9}$$

We decided for this as a first test, as it is very compact and the magnification is matching very well the value we aim for ($M_{sim} = 6.6$, see (6.3)). To evaluate the telescope we measured the beam waist at z_1 and z_2 after the telescope. To fit the beam waist, the intensity profile along the horizontal axis transverse to the propagation axis is measured by moving a power meter, with a small pinhole aperture on its measuring head, via a linear translation stage horizontally through the beam and noting the power values at each position.

In figure 6.3 (a) measurements, as well as Gaussian fits of the beam at the two positions are shown. In this configuration we see a slightly divergent beam, having a larger Gaussian beam width at the second measurement point ($w(z_2) > w(z_1)$), but the beam is already cut to a width of about 10.5 mm. By further increasing the length of the telescope, which is needed to get a convergent beam, the cutting more and more decreases the beam size at z_2. Therefore, unfortunately, it was not possible to get a convergent or even collimated beam with this lens setup, as the beam showed a strong cutting at position z_2, which rapidly increased (diameter of cut decreased) by increasing the length of the telescope.

Therefore, we tried a different lens configuration. The one closest to the desired magnification value we had at hand was

$$\text{Configuration 2}: f_1 = -25\,\text{mm}, \; f_2 = 150\,\text{mm} \;\Rightarrow\; M_{\text{c2}} = 6\,. \tag{6.10}$$

As seen in figure 6.3 (b) it was possible to get the desired ratio of beam widths for this configuration (cf. (6.8)). The beam width is with $w \approx 12\,\text{mm}$ also in the range of what

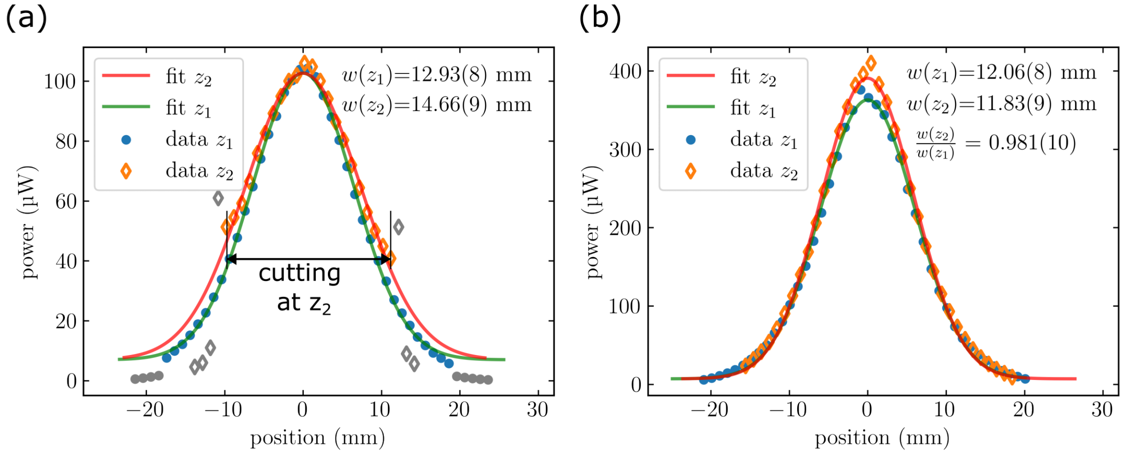

Fig. 6.3. Beam width measurements for (a) configuration 1 and (b) the final configuration 2 of the horizontal MOT beams at the two measurement points $z_1 = 30\,\text{cm}$ and $z_2 = 90\,\text{cm}$ behind the input arm. A strong cutting of the beam in configuration 1 at z_2 to a beam width of ~10.5 mm can be observed. grey points have not been used for the fitting.

we would expect ($w_{\text{cal}} = M_{\text{c2}}\, w_{\text{fib}} = 13.4(15)\,\text{mm}$, cf. (6.2)).
The second horizontal beam was aligned similarly.

The vertical MOT-beam was set up slightly different. First, we needed to adjust the input arm to get a vertical beam output, this was done by introducing a 2-inch elliptical mirror after the telescope with the $\lambda/4$-waveplate mounted on top. Second, as we had no more $f = -25\,\text{mm}$ lens available, we went on with the closest possible configuration:

$$f_1 = -18\,\text{mm},\ f_2 = 100\,\text{mm} \ \Rightarrow\ M_{\text{v}} = 5.6\,. \tag{6.11}$$

In the vertical direction, we didn't have the final setup of our main chamber for this first realization of the MOT. Due to huge delivery delay of our reentrant viewports, we realized the first MOT with standard, uncoated CF-100 viewports (cf. fig. 6.4), resulting in a much higher loss ($T_{\text{vert}} = 16\,\%$). Therefore, the beam should be significantly more convergent. In the experiment we had some difficulties in realising such a convergent beam and went on with a nearly collimated beam with a size of $w_{\text{ver}} = 11.28(1400)\,\text{mm}$ (cf. 6.1) for this temporarily setup. For the vertical direction, this is less critical, as the heavy Dy atoms experience a large downwards force anyway by gravity, which is also pointed out by the possibility of realizing a five-beam MOT without the top beam at all [49]. Furthermore, we have a rather bad beam quality, because the $-18\,\text{mm}$ lens is slightly offset from the centre, as it has an outer diameter of 12 mm and was fitted into a 1/2-inch mount. As already said, the current setup of the vertical input arm is only temporarily, it needs to be adjusted anyway when we finally mount the reentrant viewport and in this process, a different lens setup will be used.

6.3 First MOT Realization

We managed to realize a 3D-MOT in our temporarily setup shown in figure 6.4. The use of the standard CF100 viewports made it necessary to develop a second pair of HH- and

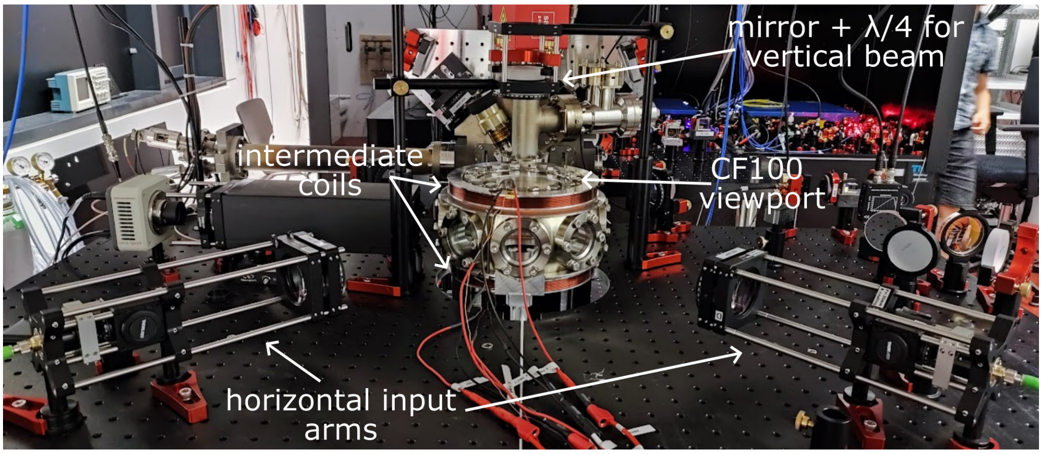

Fig. 6.4. Intermediate setup of main chamber with MOT-input arms

AHH-coils to use in this setup. The geometry of these coils is presented in [17]. The calculated current to field/gradient conversion factors are:

$$\mathbf{HH}_{\text{int}}: \ 6.74\,\text{G/A}, \quad \text{AHH}_{\mathbf{int}}: \ 1.38\,\text{G/(cm A)} \ \ (\text{along } z\text{−axis}). \tag{6.12}$$

The process of optimizing the MOT-parameters is still ongoing, the so far optimum (in terms of number of atoms loaded into the MOT) set of parameters is presented in table 6.1. It is possible to realize a MOT over a wide range of parameters, so it might be, that we will finally find an optimum with quite different values. Also the MOT loading process so far takes 30 s, which needs to be decreased. Note that so far the 2D-MOT is not optimized and we work without a push-beam from the 2D- to the 3D-MOT, which should definitely bring improvement in terms of MOT loading rate and final number of atoms.

	Unit	Simulation	Experiment		
			horiz. 1	horiz. 2	vertical
Detuning Δ	Γ_{626}	-45	$-48(4)$		
	$2\pi\times$ MHz	-6	$-6.5(5)$		
Magnetic gradient	G/cm	1.1	1.8		
Beam width w	mm	14.7	12.06(8)	12.04(8)	11.28(14)
Power per beam P	mW	100	80(2)	85(2)	90(2)
Sat. parameter $s \equiv I_c/I_{\text{sat}}$		410	486(14)	518(14)	623(26)

Table 6.1: Set of parameters for 3D-MOT obtained via Monte Carlo simulation [32] and first set of partially optimized parameters in the experiment. The beam width is defined as half the beam diameter at the $1/e^2$-intensity level and measured at the first measurement point z_1 (see (6.7)), the detuning in terms of the 626 nm-transitions decay rate Γ_{626} and the saturation parameter as the ratio of the beams center intensity I_c (see (6.5)) and the saturation intensity of the transition I_{sat} (see tab. 2.1). The magnetic gradient is calculated on the basis of the measured current via (6.12).

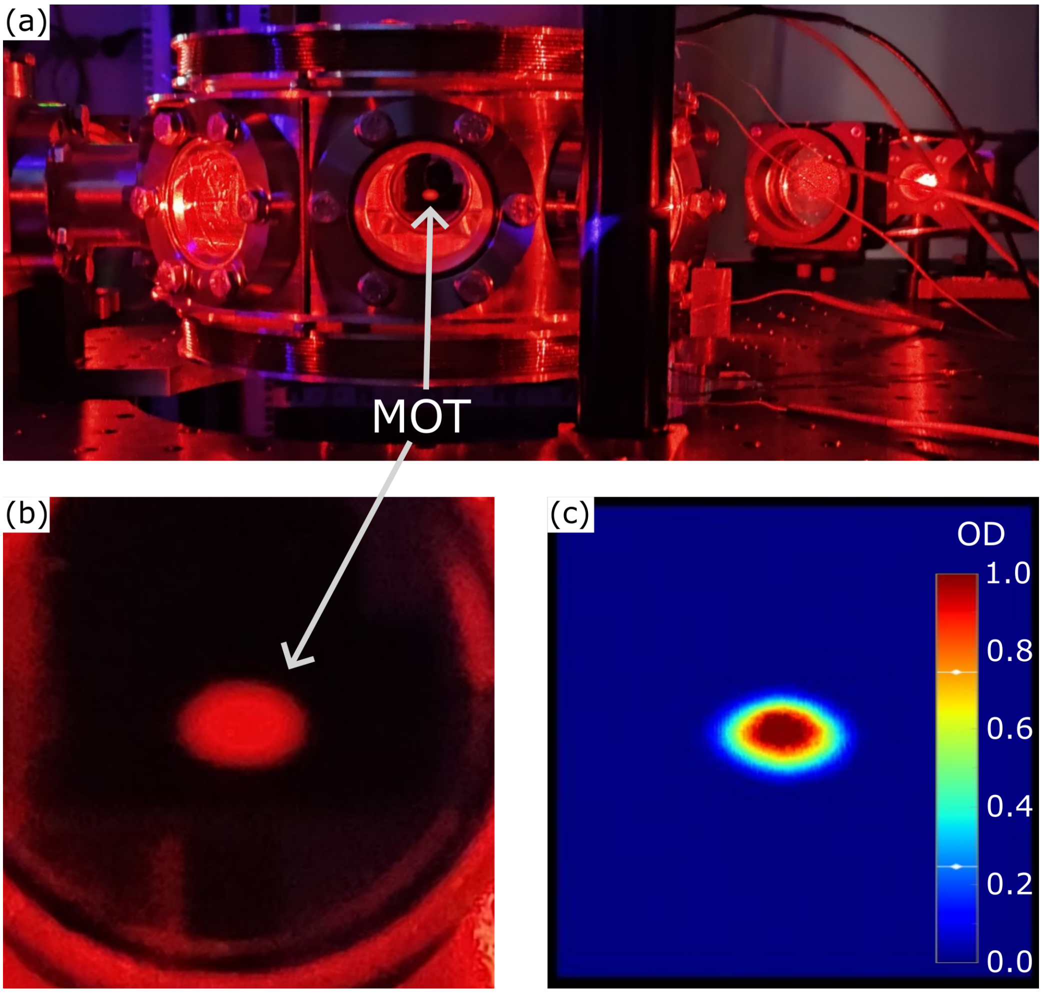

Fig. 6.5. Realization of MOT: (a), (b) images of first realization of MOT, (c) absorption imaging optical density plot of MOT with parameters presented in table 6.1, Note that the MOT-parameters are different for (a)/(b) and (c)

In figure 6.5 (a) and (b) images of our first realization of the MOT with not optimized parameters are shown, in (c) an absorption image of the MOT with the parameters presented in table 6.1 is presented. As we didn't calibrate our imaging so far, it is not possible to give an accurate number of atoms in our MOT. But we estimate it to be in the order of 1×10^7 to 2×10^7 atoms.

7 | Conclusion and Outlook

The main focus of this thesis was on the development and manufacturing of the magnetic field setup for our novel experimental apparatus producing ultracold gases of Dy atoms. We need magnetic fields that are highly stable, uniform and variable in strength and orientation to tune the contact and dipolar interactions of the atoms, as well as a quadrupole magnetic field for magneto-optical trapping and Stern-Gerlach separation. Based on the requirements dictated by this application a detailed description of the design process of the coils and holder is provided. These needed to be highly adapted to the geometric constraints of our experiment.

One major point in the design process was the decision on using a high number of windings with small wire cross-section, which decreases the contribution of every single wire to the resulting field and therefore improves the field quality by reducing the effect of in-and outgoing wires as well as winding inhomogeneities. It was shown that for small magnetic coils with limited power a fast time response with full switch on/off times in the range of 100 µs to 250 µs is possible, which will probably in any case be faster than the time-scale limit of the magnetic field due to eddy currents in the steel chamber.
The minimum requirements for the magnetic field and magnetic gradient strength can be achieved even without water cooling. The maximum homogeneous field strength we can achieve with the HH-coils is 22 G without and 57 G with active water cooling and the maximum gradients achieved with the AHH-coils are $8\,\mathrm{G\,cm^{-1}}$ without and $21\,\mathrm{G\,cm^{-1}}$ with water cooling when limiting the coil's temperature to 60 °C. These values are for continuous operation and it is possible to go to even higher fields/gradients for short times.
According to calculations we achieve the desired relative field stability for the HH-coils of $\delta_{\pm 1} < 10^{-4}$ in a region of ±1 mm around the centre. As we had no precise enough magnetic field sensor it was not possible to experimentally prove this.

During the coil characterization, we noticed a serious manufacturing issue. Two of the four manufactured holders are leaking out of their bottom plate due to an issue in the soldering process. One of the water-tight holders has a slightly uncontrolled winding structure and a short after the baking process (see 4.4). We will rewind this one and reinforce the bottom plate, probably with epoxy to minimize the risk of future leaking. This will provide us with a set of fully working coils, later we plan to repair the other two pairs by a new soldering process to have two spare coil holders.

Our current version of the power supply is limited to maximum currents of ±5 A, which corresponds quite well to the limitations of the magnetic coil setup due to heating for continuous operation. To use the full potential of the setup and produce even higher magnetic

fields and gradients for short times, slight adaptions to the current version of the supply or another power supply would be needed. Especially for Stern-Gerlach separation of a thermal cloud in the MOT this would be beneficial.
Another open point is the generation of RF-signals. It is still not fully clear and rather unlikely, that we can produce the desired RF-fields with the designed SF-coil. Testing this and if needed designing a proper RF-coil will be part of a future project.

Furthermore, we presented in this thesis the optical design of our 3D-MOT, as well as the first implementation in the experiment with the current status of the optimization process. A stable MOT with an approximated atom number of 1×10^7 w to 2×10^7 was achieved.
So far, the parameters of the 2D-MOT are not optimized and we work without a push-beam and the optimization process of the 3D-MOT is still ongoing. Furthermore, the next step is to mount the final inverted viewport and the coil setup in this thesis. From there on we will work towards optical trapping of the atoms, which is already prepared, to achieve quantum degeneracy.

A | Appendices

This chapter includes supplementary material such as technical data sheets and a technical drawing of the coil holder.

A.1 Elektrisola wire characteristics

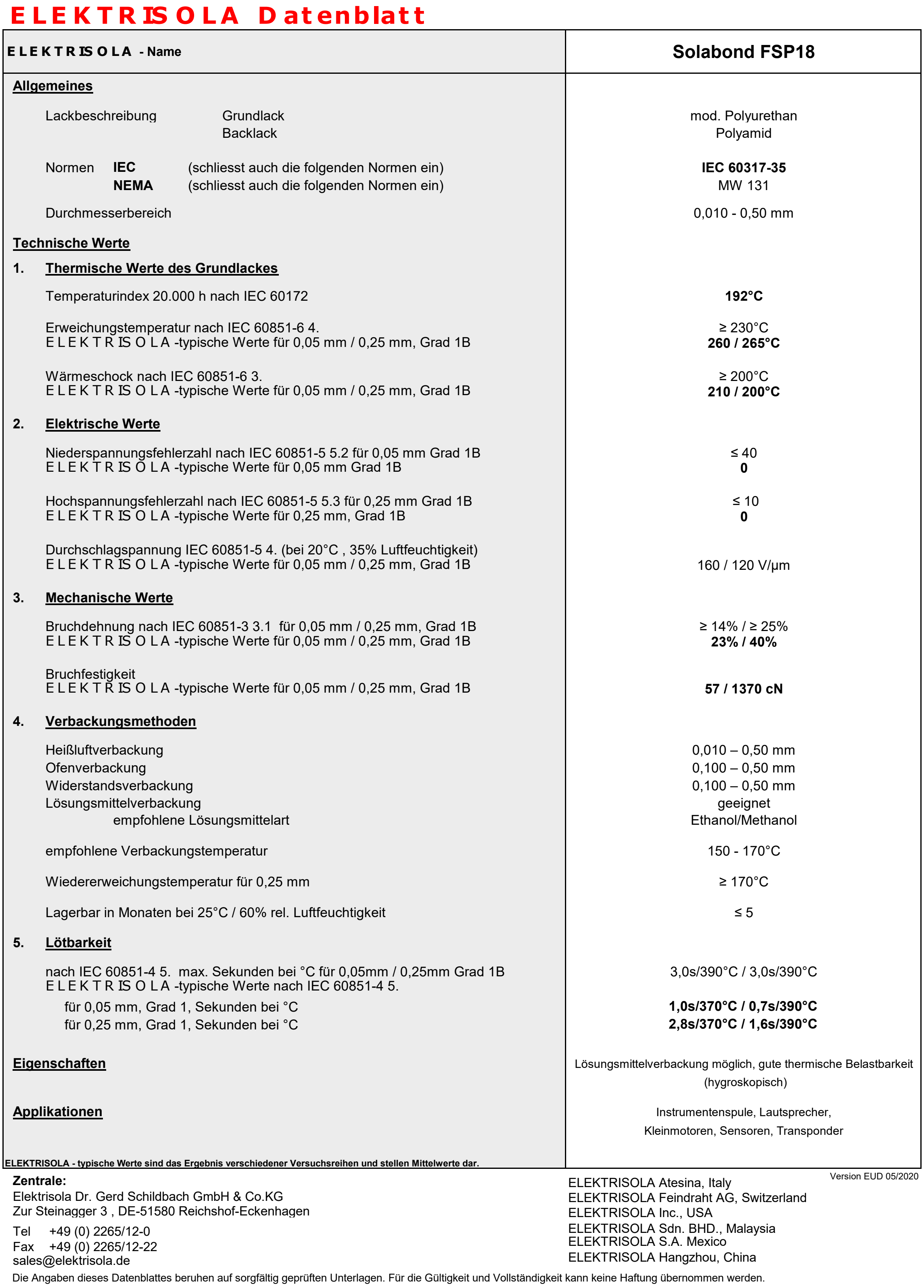

ELEKTRISOLA Datenblatt

ELEKTRISOLA - Name	**Solabond FSP18**
Allgemeines	
Lackbeschreibung: Grundlack Backlack	mod. Polyurethan Polyamid
Normen **IEC** (schliesst auch die folgenden Normen ein) **NEMA** (schliesst auch die folgenden Normen ein)	**IEC 60317-35** MW 131
Durchmesserbereich	0,010 - 0,50 mm
Technische Werte	
1. Thermische Werte des Grundlackes	
Temperaturindex 20.000 h nach IEC 60172	**192°C**
Erweichungstemperatur nach IEC 60851-6 4. ELEKTRISOLA -typische Werte für 0,05 mm / 0,25 mm, Grad 1B	≥ 230°C **260 / 265°C**
Wärmeschock nach IEC 60851-6 3. ELEKTRISOLA -typische Werte für 0,05 mm / 0,25 mm, Grad 1B	≥ 200°C **210 / 200°C**
2. Elektrische Werte	
Niederspannungsfehlerzahl nach IEC 60851-5 5.2 für 0,05 mm Grad 1B ELEKTRISOLA -typische Werte für 0,05 mm Grad 1B	≤ 40 **0**
Hochspannungsfehlerzahl nach IEC 60851-5 5.3 für 0,25 mm Grad 1B ELEKTRISOLA -typische Werte für 0,25 mm, Grad 1B	≤ 10 **0**
Durchschlagspannung IEC 60851-5 4. (bei 20°C , 35% Luftfeuchtigkeit) ELEKTRISOLA -typische Werte für 0,05 mm / 0,25 mm, Grad 1B	160 / 120 V/µm
3. Mechanische Werte	
Bruchdehnung nach IEC 60851-3 3.1 für 0,05 mm / 0,25 mm, Grad 1B ELEKTRISOLA -typische Werte für 0,05 mm / 0,25 mm, Grad 1B	≥ 14% / ≥ 25% **23% / 40%**
Bruchfestigkeit ELEKTRISOLA -typische Werte für 0,05 mm / 0,25 mm, Grad 1B	**57 / 1370 cN**
4. Verbackungsmethoden	
Heißluftverbackung	0,010 – 0,50 mm
Ofenverbackung	0,100 – 0,50 mm
Widerstandsverbackung	0,100 – 0,50 mm
Lösungsmittelverbackung	geeignet
empfohlene Lösungsmittelart	Ethanol/Methanol
empfohlene Verbackungstemperatur	150 - 170°C
Wiedererweichungstemperatur für 0,25 mm	≥ 170°C
Lagerbar in Monaten bei 25°C / 60% rel. Luftfeuchtigkeit	≤ 5
5. Lötbarkeit	
nach IEC 60851-4 5. max. Sekunden bei °C für 0,05mm / 0,25mm Grad 1B ELEKTRISOLA -typische Werte nach IEC 60851-4 5.	3,0s/390°C / 3,0s/390°C
für 0,05 mm, Grad 1, Sekunden bei °C	**1,0s/370°C / 0,7s/390°C**
für 0,25 mm, Grad 1, Sekunden bei °C	**2,8s/370°C / 1,6s/390°C**
Eigenschaften	Lösungsmittelverbackung möglich, gute thermische Belastbarkeit (hygroskopisch)
Applikationen	Instrumentenspule, Lautsprecher, Kleinmotoren, Sensoren, Transponder

ELEKTRISOLA - typische Werte sind das Ergebnis verschiedener Versuchsreihen und stellen Mittelwerte dar.

Version EUD 05/2020

Zentrale:
Elektrisola Dr. Gerd Schildbach GmbH & Co.KG
Zur Steinagger 3 , DE-51580 Reichshof-Eckenhagen
Tel +49 (0) 2265/12-0
Fax +49 (0) 2265/12-22
sales@elektrisola.de

ELEKTRISOLA Atesina, Italy
ELEKTRISOLA Feindraht AG, Switzerland
ELEKTRISOLA Inc., USA
ELEKTRISOLA Sdn. BHD., Malaysia
ELEKTRISOLA S.A. Mexico
ELEKTRISOLA Hangzhou, China

Die Angaben dieses Datenblattes beruhen auf sorgfältig geprüften Unterlagen. Für die Gültigkeit und Vollständigkeit kann keine Haftung übernommen werden.

ELEKTRISOLA

Group

High Thermal Conductive Wire for EV

Objective

- higher efficiency of electric coils in EV applications by improved thermal conductivity

Solution (Patent by Elektrisola)

- development of enamel with improved thermal conductivity with
  - high dielectric strength
  - high temperature class insulation

Thermal conductivity of different wires

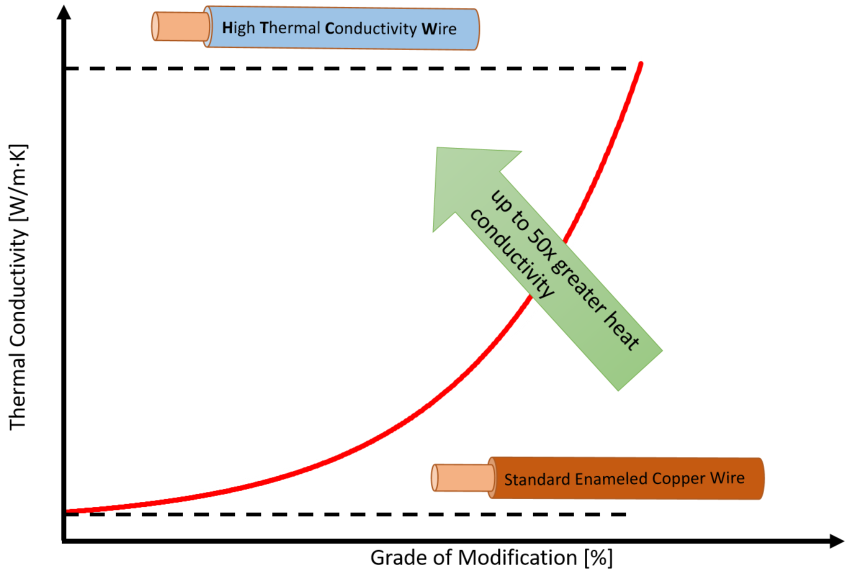

ELEKTRISOLA Dr. Gerd Schildbach GmbH & Co.KG
D-51580 Reichshof-Eckenhagen, Germany

Contact:
sales@elektrisola.de

ELEKTRISOLA

Group

Advantages:

- **Technical**

  Higher efficiency by

  - ☐ lower core temperature due to better heat conductivity
  - ☐ significant reduction of thermal copper losses
  - ☐ improved thermal conductivity between copper conductor and potting or impregnation resins

- **Commercial**

  - ☐ efficiency gain
  - ☐ less complex cooling needed
  - ☐ smaller coil possible = lower cost

Example of coil temperature:

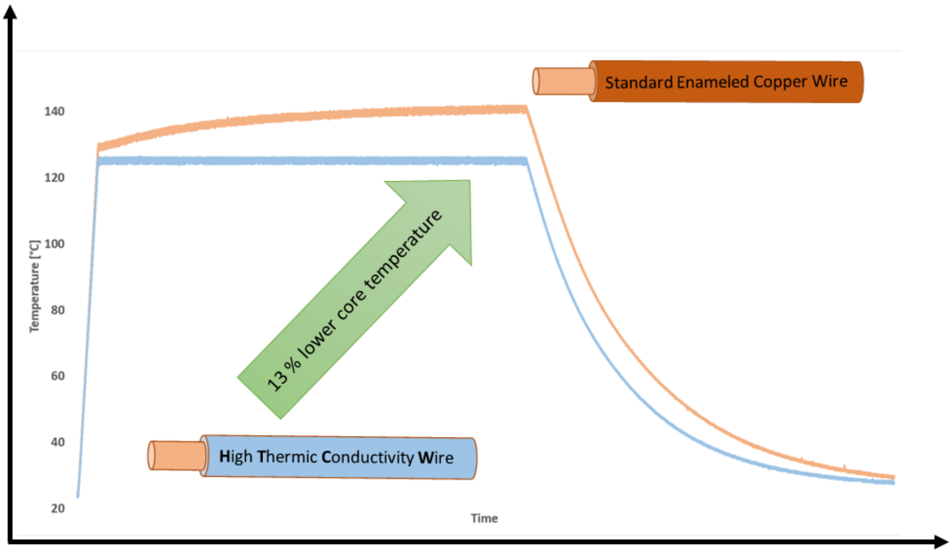

ELEKTRISOLA Dr. Gerd Schildbach GmbH & Co.KG
D-51580 Reichshof-Eckenhagen, Germany

Contact:
sales@elektrisola.de

A.2 Technical Drawing Holder

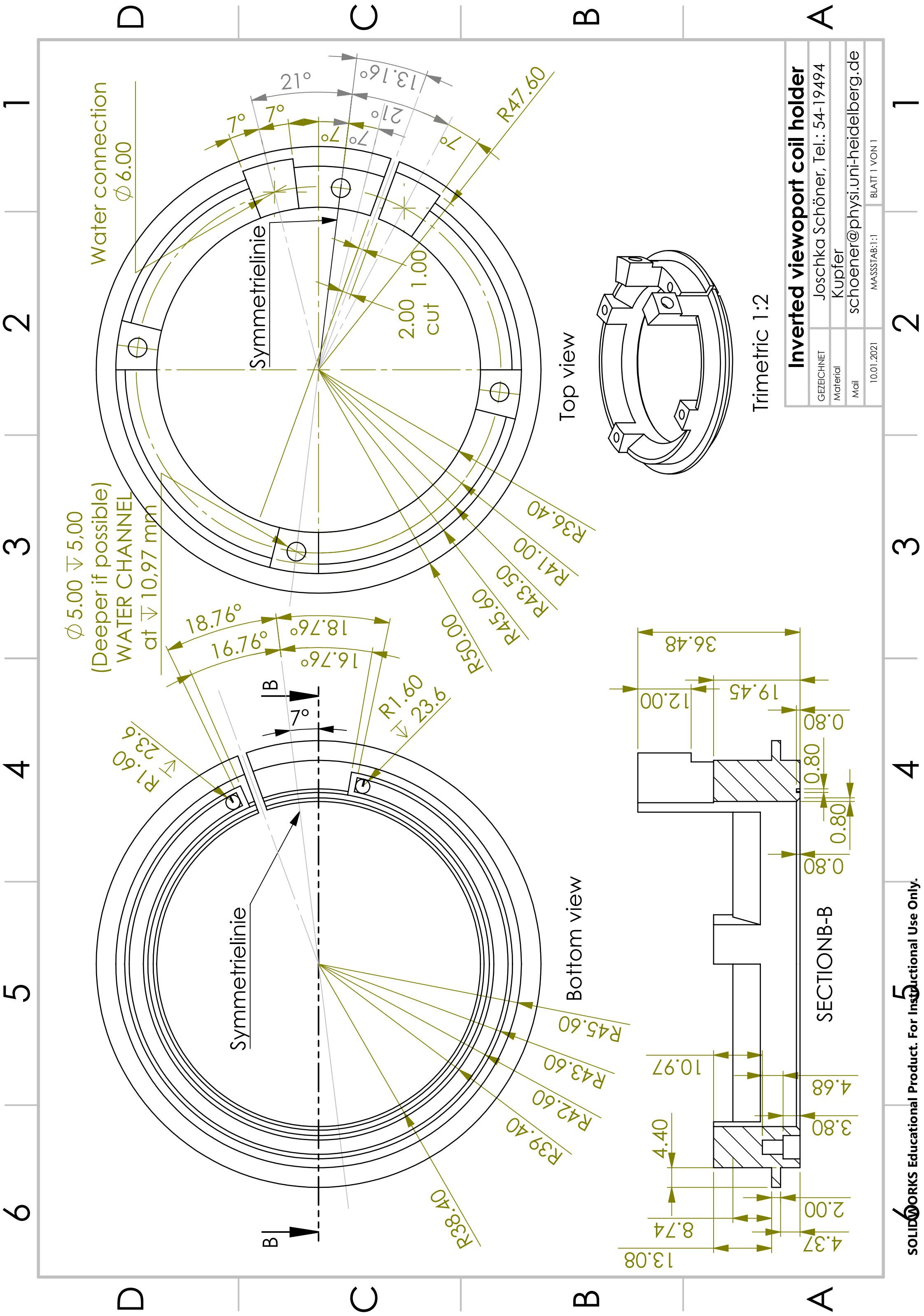

B Bibliography

[1] Mike H Anderson, Jason R Ensher, Michael R Matthews, Carl E Wieman, and Eric A Cornell. Observation of bose-einstein condensation in a dilute atomic vapor. *science*, 269(5221):198–201, 1995.

[2] Kendall B Davis, M-O Mewes, Michael R Andrews, Nicolaas J van Druten, Dallin S Durfee, DM Kurn, and Wolfgang Ketterle. Bose-einstein condensation in a gas of sodium atoms. *Physical review letters*, 75(22):3969, 1995.

[3] Axel Griesmaier, Jörg Werner, Sven Hensler, Jürgen Stuhler, and Tilman Pfau. Bose-einstein condensation of chromium. *Physical Review Letters*, 94(16):160401, 2005.

[4] Lauriane Chomaz, Igor Ferrier-Barbut, Francesca Ferlaino, Bruno Laburthe-Tolra, Benjamin L Lev, and Tilman Pfau. Dipolar physics: A review of experiments with magnetic quantum gases. *arXiv preprint arXiv:2201.02672*, 2022.

[5] Mingwu Lu, Seo Ho Youn, and Benjamin L Lev. Spectroscopy of a narrow-line laser-cooling transition in atomic dysprosium. *Physical Review A*, 83(1):012510, 2011.

[6] T Maier, H Kadau, M Schmitt, M Wenzel, I Ferrier-Barbut, T Pfau, Albert Frisch, Simon Baier, Kiyotaka Aikawa, Lauriane Chomaz, et al. Emergence of chaotic scattering in ultracold er and dy. *Physical Review X*, 5(4):041029, 2015.

[7] Holger Kadau, Matthias Schmitt, Matthias Wenzel, Clarissa Wink, Thomas Maier, Igor Ferrier-Barbut, and Tilman Pfau. Observing the rosensweig instability of a quantum ferrofluid. *Nature*, 530(7589):194–197, 2016.

[8] L Chomaz, S Baier, D Petter, MJ Mark, F Wächtler, Luis Santos, and F Ferlaino. Quantum-fluctuation-driven crossover from a dilute bose-einstein condensate to a macrodroplet in a dipolar quantum fluid. *Physical Review X*, 6(4):041039, 2016.

[9] Igor Ferrier-Barbut, Holger Kadau, Matthias Schmitt, Matthias Wenzel, and Tilman Pfau. Observation of quantum droplets in a strongly dipolar bose gas. *Physical review letters*, 116(21):215301, 2016.

[10] Matthew A Norcia, Claudia Politi, Lauritz Klaus, Elena Poli, Maximilian Sohmen, Manfred J Mark, Russell N Bisset, Luis Santos, and Francesca Ferlaino. Two-dimensional supersolidity in a dipolar quantum gas. *Nature*, 596(7872):357–361, 2021.

[11] L. Tanzi, E. Lucioni, F. Famà, J. Catani, A. Fioretti, C. Gabbanini, R. N. Bisset, L. Santos, and G. Modugno. Observation of a dipolar quantum gas with metastable supersolid properties. *Phys. Rev. Lett.*, 122:130405, Apr 2019.

[12] L Chomaz, D Petter, P Ilzhöfer, G Natale, A Trautmann, C Politi, G Durastante, RMW Van Bijnen, A Patscheider, M Sohmen, et al. Long-lived and transient supersolid behaviors in dipolar quantum gases. *Physical Review X*, 9(2):021012, 2019.

[13] Fabian Böttcher, Jan-Niklas Schmidt, Matthias Wenzel, Jens Hertkorn, Mingyang Guo, Tim Langen, and Tilman Pfau. Transient supersolid properties in an array of dipolar quantum droplets. *Phys. Rev. X*, 9:011051, Mar 2019.

[14] Cheng Chin, Rudolf Grimm, Paul Julienne, and Eite Tiesinga. Feshbach resonances in ultracold gases. *Reviews of Modern Physics*, 82(2):1225, 2010.

[15] Eric L Raab, Mara Prentiss, Alex Cable, Steven Chu, and David E Pritchard. Trapping of neutral sodium atoms with radiation pressure. *Physical review letters*, 59(23):2631, 1987.

[16] Walther Gerlach and Otto Stern. Der experimentelle nachweis der richtungsquantelung im magnetfeld. *Zeitschrift für Physik*, 9(1):349–352, 1922.

[17] Lennart Hoenen. *Fast, High Precision Low Noise Bipolar Power Supply for Magnetic Field Coils in Ultra-Cold Dysprosium Experiment.* Bachelor's thesis, Heidelberg University, 2022.

[18] David R Lide. *CRC handbook of chemistry and physics*, volume 85. CRC press, 2004.

[19] Christopher J Foot. *Atomic physics*, volume 7. OUP Oxford, 2004.

[20] William Clyde Martin, Zalubas R., and Hagan L. *Atomic energy levels: The rare earth elements*, page 261. United States. National Bureau of Standards and Burris, B.L. and Morehouse, R.J., 1978.

[21] Philipp Ilzhöfer. *Creation of Dipolar Quantum Mixtures of Erbium and Dysprosium.* PhD thesis, University of Innsbruck, 2020.

[22] Thierry Lahaye, C Menotti, L Santos, M Lewenstein, and T Pfau. The physics of dipolar bosonic quantum gases. *Reports on Progress in Physics*, 72(12):126401, 2009.

[23] Christopher J Pethick and Henrik Smith. *Bose–Einstein condensation in dilute gases.* Cambridge university press, 2008.

[24] Hiroki Saito and Masahito Ueda. Mean-field analysis of collapsing and exploding bose-einstein condensates. *Physical Review A*, 65(3):033624, 2002.

[25] Tsin D Lee, Kerson Huang, and Chen N Yang. Eigenvalues and eigenfunctions of a bose system of hard spheres and its low-temperature properties. *Physical Review*, 106(6):1135, 1957.

[26] Matteo Barbiero. *Novel techniques for a strontium optical lattice clock.* PhD thesis, PhD thesis, Polytechnic University of Turin, 2019.

[27] Wolfgang Demtröder. *Atoms, molecules and photons*, volume 3. Springer, 2010.

[28] Kristian Baumann, Nathaniel Q Burdick, Mingwu Lu, and Benjamin L Lev. Observation of low-field fano-feshbach resonances in ultracold gases of dysprosium. *Physical Review A*, 89(2):020701, 2014.

[29] C. H. Schunck, M. W. Zwierlein, C. A. Stan, S. M. F. Raupach, W. Ketterle, A. Simoni, E. Tiesinga, C. J. Williams, and P. S. Julienne. Feshbach resonances in fermionic lithium-6. *Physical Review A*, 71(4), 2005.

[30] Davide Dreon, Leonid A Sidorenkov, Chayma Bouazza, Wilfried Maineult, Jean Dalibard, and Sylvain Nascimbene. Optical cooling and trapping of highly magnetic atoms: the benefits of a spontaneous spin polarization. *Journal of Physics B: Atomic, Molecular and Optical Physics*, 50(6):065005, 2017.

[31] Valentina Salazar. *The Accordion Lattice: Trapping of Bosonic Dysprosium Ultracold Gases in Two Dimensions (working title).* Master's thesis, Heidelberg University, 2022 (will be published).

[32] Jianshun Gao. *A First Two-Dimensional Magneto-Optical Trap for Dysprosium.* Phd admission thesis, Heidelberg University, 2022 (will be published).

[33] William R. Smythe. *Static and Dynamic Electricity, Second Edition.* International Series in pure and applied Physics. McGraw-Hill Book Company, Inc., 1950.

[34] SG Sandomirskii. Calculation of acceptable stationary current density in magnetizing coil at natural cooling with surrounding air. *Russian Electrical Engineering*, 81(5):270–273, 2010.

[35] Thomas Zickler. Normal-conductinng accelerator magnets, lecture 3: Analytical design. `https://indico.cern.ch/event/779575/contributions/3244562/attachments/1796007/2930569/JUAS_lecture_2019_Lecture_3_Transparencies.pdf`. Joint Universities Accelerator School, JUAS 2019.

[36] Professor John Perry D.Sc. F.R.S. Xxvi. a formula for calculating approximately the self-induction of a coil. *The London, Edinburgh, and Dublin Philosophical Magazine and Journal of Science*, 30(184):223–227, 1890.

[37] Chapter 14 - mechanical engineering. In Philip Kosky, Robert Balmer, William Keat, and George Wise, editors, *Exploring Engineering (Fifth Edition)*, pages 317–340. Academic Press, fifth edition edition, 2021.

[38] Wikipedia. Electrical resistivity and conductivity — Wikipedia, the free encyclopedia. `http://en.wikipedia.org/w/index.php?title=Electrical%20resistivity%20and%20conductivity&oldid=1099758295`, 2022. [Online; accessed 22-July-2022].

[39] Wikipedia. List of thermal conductivities — Wikipedia, the free encyclopedia. `http://en.wikipedia.org/w/index.php?title=List%20of%20thermal%20conductivities&oldid=1097122183`, 2022. [Online; accessed 22-July-2022].

[40] Wikipedia. Wasser — Wikipedia, the free encyclopedia. `http://de.wikipedia.org/w/index.php?title=Wasser&oldid=224906118`, 2022. [Online; accessed 31-July-2022].

[41] W. Demtröder. *Experimentalphysik 1: Mechanik und Wärme.* Springer-Lehrbuch. Springer Berlin Heidelberg, 2015.

[42] Yu-Meng Yang, Hong-Tai Xie, Wen-Chao Ji, Yue-Fei Wang, Wei-Yong Zhang, Shuai Chen, and Xiao Jiang. Ultra-low noise and high bandwidth bipolar current driver for precise magnetic field control. *Review of Scientific Instruments*, 90(1):014701, 2019.

[43] Texas Instruments. High-voltage, high-current operational amplifier. `https://www.ti.com/lit/gpn/opa549`, 2022.

[44] Wikipedia. Polyether ether ketone — Wikipedia, the free encyclopedia. `http://en.wikipedia.org/w/index.php?title=Polyether%20ether%20ketone&oldid=1103607101`, 2022. [Online; accessed 15-August-2022].

[45] Jürgen Hagedorn, Florian Sell-Le Blanc, and Jürgen Fleischer. Handbook of coil winding. *Springer Berlin Heidelberg*, 2018.

[46] Wikipedia. Thermal expansion — Wikipedia, the free encyclopedia. `http://en.wikipedia.org/w/index.php?title=Thermal%20expansion&oldid=1095877520`, 2022. [Online; accessed 04-August-2022].

[47] Christian Gölzhäuser. *Building a new Dy quantum gas experiment.* Bachelor's thesis, Heidelberg University, 2021.

[48] Bahaa EA Saleh and Malvin Carl Teich. *Fundamentals of photonics.* john Wiley & sons, 2007.

[49] P Ilzhöfer, G Durastante, A Patscheider, A Trautmann, MJ Mark, and F Ferlaino. Two-species five-beam magneto-optical trap for erbium and dysprosium. *Physical Review A*, 97(2):023633, 2018.

Erklärung:

Ich versichere, dass ich diese Arbeit selbstständig verfasst habe und keine anderen als die angegebenen Quellen und Hilfsmittel benutzt habe.

Blåvand, den 12. September 2022

Joschka Schöner